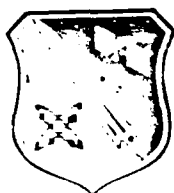


DOD COPY

(9)



AL-TR-89-076

AD:

Final Report
for the period
August 1986 to
June 1989

Model Studies of CBES Decomposition

February 1990

Authors:
T.A. Seder
D.J. Bernard
R.H. Cohn
Rockwell International
Science Center
1049 Camino Dos Rios
Thousand Oaks CA 91360

AD-A219 744

F04611-86-C-0072
SC5467.FR

APR 21 1990
C
E
D

Approved for Public Release

Distribution is unlimited. The AL Technical Services Office has reviewed this report, and it is releasable to the National Technical Information Service, where it will be available to the general public, including foreign nationals.

Prepared for the:

Astronautics Laboratory (AFSC)
Air Force Space Technology Center
Space Systems Division
Air Force Systems Command
Edwards AFB CA 93523-5000

NOTICE

When U.S. Government drawings, specifications, or other data are used for any purpose other than a definitely related Government procurement operation, the fact that the Government may have formulated, furnished, or in any way supplied the said drawings, specifications, or other data, is not to be regarded by implication or otherwise, or in any way licensing the holder or any other person or corporation, or conveying any rights or permission to manufacture, use, or sell any patented invention that may be related thereto.

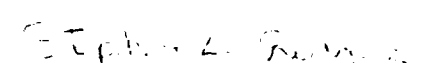
FOREWORD

This final report was submitted by Rockwell International Science Center, Seal Beach CA on completion of contract F04611-86-C-0072 to the Astronautics Laboratory (AFSC), Edwards Air Force Base, CA. AL Project Manager was Capt Steven Thompson.

This report has been reviewed and is approved for release and distribution in accordance with the distribution statement on the cover and on the DD Form 1473.

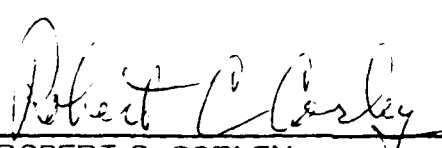


STEVEN D. THOMPSON, CAPT, USAF
Project Manager



STEPHEN L. RODGERS
Chief, Applied Research In Energy
Storage Office

FOR THE DIRECTOR



ROBERT C. CORLEY
Director, Astronautical Sciences Division

UNCLASSIFIED

SECURITY CLASSIFICATION OF THIS PAGE

FORM APPROVED
OMB No. 0704-0188

REPORT DOCUMENTATION PAGE			
1a. REPORT SECURITY CLASSIFICATION UNCLASSIFIED		1b. RESTRICTIVE MARKINGS	
2a. SECURITY CLASSIFICATION AUTHORITY		3. DISTRIBUTION/AVAILABILITY OF REPORT Approved for public release; distribution unlimited	
2b. CLASSIFICATION/DOWNGRADING SCHEDULE			
4. PERFORMING ORGANIZATION REPORT NUMBER(S) SC5467.FR		5. MONITORING ORGANIZATION REPORT NUMBER(S) AL-TR-89-076	
6a. NAME OF PERFORMING ORGANIZATION ROCKWELL INTERNATIONAL Science Center	6b. OFFICE SYMBOL <i>(If Applicable)</i>	7a. NAME OF MONITORING ORGANIZATION Astronautics Laboratory (AFSC)	
6c. ADDRESS (City, State, and ZIP Code) 1049 Camino Dos Rios Thousand Oaks, CA 91360		7b. ADDRESS (City, State and ZIP Code) AL/LSX Edwards AFB CA 93523-5000	
8a. NAME OF FUNDING SPONSORING ORGANIZATION	8b. OFFICE SYMBOL <i>(If Applicable)</i>	9. PROCUREMENT INSTRUMENT IDENTIFICATION NUMBER CONTRACT NO. F04611-86-C-0072	
8c. ADDRESS (City, State and ZIP Code)		10. SOURCE OF FUNDING NOS.	
		PROGRAM ELEMENT NO. 62302F	PROJECT NO. 5730
		TASK NO. 00	WORK UNIT ACCESSION NO. WM
11. TITLE (Include Security Classification) MODEL STUDIES OF CBES DECOMPOSITION			
12. PERSONAL AUTHOR(S) Seder, T.A., Benard, D.J. and Cohn, R.H.			
13a. TYPE OF REPORT Final Report	13b. TIME COVERED FROM <u>86/08/05</u> TO <u>89/06/30</u>		14. DATE OF REPORT (Year, Month, Day) 90/02
15. PAGE COUNT 106			
16. SUPPLEMENTARY NOTATION <i>(CBES)</i>			
17. COSATI CODES	18. SUBJECT TERMS (Continue on reverse if necessary and identify by block number) Fluorine azide, nitrogen fluoride, chemically bound excited states, diatomic molecules detonation, decomposition and dissociation reactions, electronic and vibrational excitation, metastable states, energy storage, transfer and pooling, emission spectra, kinetics, potential energy curves, high impulse propellants		
FIELD 7	GROUP 04	SUB-GROUP	
21	09		
19. ABSTRACT (Continue on reverse if necessary and identify by block number) The explosive decomposition of cryogenic films of fluorine azide, FN₃, has been studied using a variety of experimental techniques. Although the amounts of NF(a) and NF(b) produced upon film combustion was found to be below the detection limits of our emission spectrometer, indirect evidence of the presence of these species has been recorded. The presence of CN(B-X) emission and the absence of CN(A-X) emission implied B state population via resonant energy transfer from a combustion species, having at least 3.2 eV of excitation. Also, using schlieren photography and an optical scattering probe it was deduced that the minimum burn velocity of the material is 1.6 mm/μs. From these observations a simple model involving shock induced unimolecular decomposition of FN₃ was developed to describe the detonation of the films. Consistent with the model, the burn velocity could be moderated via addition			
20. DISTRIBUTION/AVAILABILITY OF ABSTRACT UNCLASSIFIED/UNLIMITED <input type="checkbox"/> SAME AS RPT. <input checked="" type="checkbox"/> DTIC USERS <input type="checkbox"/>		21. ABSTRACT SECURITY CLASSIFICATION UNCLASSIFIED	
22a. NAME OF RESPONSIBLE INDIVIDUAL Capt. Steven Thompson		22b. TELEPHONE NUMBER <i>(Include Area Code)</i> (805) 275-5651	22c. OFFICE SYMBOL AL/LSX

UNCLASSIFIED

SECURITY CLASSIFICATION OF THIS PAGE

19. ABSTRACT (Cont'd)

of high heat capacity materials. Also, the burn velocity was found to be dramatically altered by low level impurities which appear as a result of the thermal decomposition of FN_3 . Since the pure azide has an exceedingly high specific impulse, relative to monopropellants, and the burn rate of this material is broadly tunable via additives, the results of the above studies indicate that FN_3 can be developed for use as a high performance monopropellant.

A-1

TABLE OF CONTENTS

	<u>Page</u>
1.0 INTRODUCTION	1
2.0 EXPERIMENTAL TECHNIQUES	5
2.1 Synthesis of Fluorine Azide	5
2.2 Formation and Characterization of FN ₃ Films	23
2.3 Ignition and Combustion Diagnostics	27
3.0 EMISSION MEASUREMENTS	40
3.1 Emission Spectra	40
3.2 Analysis of Emitters	42
3.3 Decomposition Mechanism	51
4.0 BURN VELOCITY DETERMINATION	53
4.1 Time-Resolved Scattering	53
4.2 Schlieren Photography	61
4.3 Detonation of Condensed Phase FN ₃	63
5.0 STABILIZATION STUDIES	69
5.1 Infrared and Mass Spectrometric Analysis	69
5.2 Moderation of Burn Velocity	82
5.3 Mechanism of Stability Enhancement	88
6.0 SUMMARY AND RECOMMENDATIONS	90
7.0 REFERENCES	92

LIST OF FIGURES

<u>Figure</u>		<u>Page</u>
1	Potential energy curves of fluorine azide	4
2	Schematic diagram of fluorine azide generator	7
3	Detailed view of HN_3 generator	8
4	Vapor pressure curves of FN_3 and HF	10
5	Temporal behavior of HN_3 generator with constant heater power and 0.5 mol NaN_3 with 2.0 mol stearic acid	11
6	Temporal behavior of HN_3 generator with constant heater power and 0.1 mol NaN_3 with 2.0 mol stearic acid	11
7	Schematic diagram of infrared absorption diagnostic	12
8	Feedback circuit for temperature stabilization of PbSe detector	14
9	Comparison of infrared and ultraviolet absorption diagnostic with constant heater power	14
10	Schematic diagram of programmed power supply used to stabilize HN_3 generation rate	15
11	Temporal behavior of HN_3 generator using programmed power supply	16
12	Response of infrared absorption diagnostic to generation of FN_3	16
13	Schematic diagram of FN_3 transfer and storage system	18
14	Magnitude of the FN_3 mass signal in the 8°C holding tank gases at various times	19
15	Gas phase infrared spectrum of holding tank stored FN_3	20
16	Expanded view of the 1000 cm^{-1} region of the gas phase FN_3 spectrum	24
17	Infrared spectrum of gas phase HN_3	25
18	Schematic diagram of azide film combustion chamber	26
19	uv-vis absorption spectrum of cryogenic FN_3 film	26

LIST OF FIGURES (Continued)

<u>Figure</u>		<u>Page</u>
20	Infrared spectrum of cryogenic FN ₃ film on KBr substrate	28
21	Cartoon depicting evolution of burning azide film.....	28
22	Diagram of apparatus used to analyze plume emission	31
23	Block diagram of optical detection system	31
24	Schematic diagram of synchronization circuit	32
25	Instrument response function of OMA and monochromator	33
26	Schematic diagram of apparatus used for delayed-pulse probe of film thickness	34
27	Diagram of cw laser scattering apparatus for measurement of burn velocity along the substrate	36
28	Apparatus used for measurement of ignition delay time.....	37
29	Diagram of thermal lensing apparatus for plume velocity measurement	38
30	Diagram of pulsed laser schlieren photography system	39
31	Near-uv and vis emission spectra from combustion of film formed with cold trap-bypassed FN ₃ on CaF ₂ substrate	41
32	Near uv and vis emission spectra from combustion of film formed with cold trap-purified FN ₃ on CaF ₂ substrate	42
33	Near uv and vis emission spectra from combustion of film formed with cold trap-purified FN ₃ on SiO ₂ substrate	43
34	Potential energy curves of NF	45
35	Vibrational energy and quantum number of NF(b) vs wavelength of the $\Delta v = 0$ transition to NF(X)	46
36	Gated emission spectra of NF ₃ film cumbustions with a 100 ns delay and aperture times of 10 μ s (a) and 50 μ s (b)	48
37	Derivation of approximate time profiles from gated emission spectra	49

LIST OF FIGURES (Continued)

<u>Figure</u>		<u>Page</u>
38	Temporal profile of the emission feature at 430 nm and 470 nm	50
39	Storage oscilloscope traces corresponding to laser intensity with no film (1), with azide film before ignition (2) and 10 ns after film ignition (3)	54
40	Data from laser scattering measurement of burn velocity for a thin film (a) and a thicker film (b)	56
41	Plot of delay time to scattering probe site vs FN ₃ film thickness	57
42	Example data from measurement of ignition delay via laser scattering	59
43	Plot of ignition delay against ignition laser energy	59
44	Plot of ignition delay against ignition laser energy on same scale as Fig. 41	60
45	Example data from plume velocity measurement via thermal lensing	61
46	Schlieren photograph of expanding plume at 1.8 μ s following ignition	62
47	Schlieren photographs of plume at various times	63
48	Plot of schlieren measured film burn distance against time	64
49	Plot of schlieren measured plume height against time	64
50	Cartoon of plumes formed from film deflagration (a) and detonation (b)	67
51	Simple model for detonation of FN ₃ films	68
52	FTIR spectra of azide film on an NaCl substrate before (a) and after (b) ignition	71
53	FTIR spectrum of surface remnants which result from removing films from a KBr substrate by gentle heating	72
54	FTIR spectrum of surface remnants on-an NaCl substrate taken at room temperature in air	73

LIST OF FIGURES (Continued)

<u>Figure</u>		<u>Page</u>
55	FTIR spectrum showing disappearance of surface remnant upon deposition of an azide film	74
56	Comparison of FTIR spectra of films formed from trap-purified (a) and trap-bypassed FN ₃	75
57	Comparison of FTIR spectra of films formed from pure FN ₃ (a) and HN ₃ tainted FN ₃ (b)	76
58	FTIR spectrum of solid HN ₃	77
59	Expansion of the 2100 cm ⁻¹ region of the spectra displayed in Fig. 57	78
60	Mass spectrum of holding tank gases tank immediately filling with output of FN ₃ generator	79
61	Ratios of the mass signals of impurities to FN ₃ for gases in the holding tank at various times: CO ₂ /FN ₃ (a); N ₂ F ₂ , NF ₃ , and N ₂ F ₄ /FN ₃ (b)	80
62	FTIR spectra of films formed after first passing FN ₃ through coil of tubing maintained at room temperature (a), 70°C (b) and 150°C (c)	81
63	Comparison of FTIR spectra of films formed with FN ₃ held in tank for 0 min. (a), 23 min. (b) and 38 min. (c)	82
64	Expansion of the 1000 cm ⁻¹ region of Fig. 63	83
65	Expansion of the 2200 cm ⁻¹ region of Fig. 63	84
66	Delay in arrival of combustion front to probe site plotted against percentage of CO ₂ added to film	86
67	Delay in arrival of combustion front to probe site plotted against time gases were held in 9°C holding tank	86
68	Percentage of CO ₂ relative to CO ₂ + FN ₃ in 9°C holding tank plotted against holding time	87
69	Difference FTIR spectra taken from 9°C holding tank gases at 0 and 30 minutes	87
70	Diagram of regular sheet structure of solid FN ₃ calculated by Brener	89

LIST OF TABLES

<u>Table</u>		<u>Page</u>
1	Assignments of Infrared Absorption Bands Observed in Holding Tank Gas	21
2	Infrared Absorptions of cis and trans N ₂ F ₂	22
3	Assignments of Infrared Absorptions of Observed in FN ₃ Films	29

1.0 INTRODUCTION

The development of new classes of high energy density materials for the use in advanced propellant systems presents an array of challenges which must be addressed prior to device application. Following the development of novel methods of energy storage, for instance, via charge separation, ring strain, or in energetic metastable chemical bonds, an understanding of the chemical physics of the decomposition of the energetic material must be developed. In addition to being necessary for safety in handling and storage, an understanding of the decomposition processes is required to tailor combustion rates and to prevent uncontrollable detonations. Consequently, the goal of the Astonautics Laboratory funded research reported here was to attain enough of an understanding of the combustion mechanism of a potential advanced propellant, fluorine azide, to intelligently choose additives which could act as 'stabilizers' against unwanted decomposition.

Fluorine azide, FN_3 , was chosen for study because it is prototypical of an important class of high energy density materials referred to as chemically bound excited state (CBES) species. The interesting and important characteristic of CBES materials is that an excited state fragment is produced via thermal dissociation. FN_3 , for instance, can be thermally decomposed to generate $\text{NF}(\text{a})$ and $\text{N}_2(\text{X})$. Since the material is essentially an excited state species whose lifetime is enhanced through interaction with a ground state molecule, it is an effective store of electronic excitation energy. In addition to its usefulness as an advanced propellant, this energy store can be potentially used to fuel a chemical laser. (Indeed, using funds provided by the Weapons Laboratory, we currently are developing a fluorine azide fueled BiF(A-X) laser.)

During the course of this work, we have benefitted from the results of azide studies conducted via the Rockwell International Independent Research and Development program, as well as that of other researchers. Until recently, very little information on the properties of FN_3 have been reported. This is, no doubt, due to the fragile, toxic and explosive nature of fluorine azide. Haller,¹ who first synthesized and characterized the physical properties of the molecule in the early 1940's, noted the highly sensitive nature of the material. The material was found to be light and shock sensitive, as well as extremely energetic. Two drops would pulverize all glass within 15 cm, propelling fragments through a 24 gauge steel barrier positioned 5 cm from the ignition site. More

recent quantitative measurements of the energy content of this molecule have been performed by Patel and co-workers.² They estimated the heat of formation of the molecule to be an exceedingly high +120-135 kcal/mol. Further characterizations of the spectral and physical properties of fluorine azide have been conducted by Gholivand and co-workers.³ Their experimentally observed values for the vibrational frequencies of FN₃ are in accord with the theoretical values provided by Michels.⁴ Finally, theoretical work, most notably, calculation of the condensed phase structure and density of the material, has been performed by Brener.⁵

From the results of these studies a thorough understanding of the chemical physics of fluorine azide is emerging. In particular, the explosive nature of the FN₃ molecule is a result of an exceedingly weak FN-NN bond, in addition to a high energy content. The activation energy for cleavage of this bond has been calculated by Michels⁴ to be approximately 0.6 eV, a result which has been verified by Benard and co-workers.⁶ The calculated and experimentally verified potential energy surface is shown in Fig. 1. The potential energy change resulting from the stretching of the FN-NN bond is represented in the figure by the solid line. Depending on the geometry of the FN₃ transition state, bond breakage leads to excited singlet state NF fragments via either the NF(a) or NF(b) dissociation channels. Significantly, the triplet surface (dotted line in Fig. 1) intersects the singlet surface on the products side on the transition state. Consequently, the dissociating azide passes through the region of surface crossing only once: hence, the probability of crossing onto the ground state triplet NF(X) surface is low. If, on the other hand, the singlet-triplet surface crossing occurred on the reagent (FN₃) side of the transition state, a thermally excited (vibrating) azide molecule would sample the surface crossing region multiple times prior to reaching the transition state. Thus, the likelihood of surface crossing is enhanced and the yield of excited state NF fragments is diminished.

The low dissociation energy of the FN₃ barrier is attributed to the electronegativity of the fluorine atom: The bonding in XN₃ species is such that as the electronegativity of the X atom increases, the electron density withdrawn by the halogen causes a lengthening and weakening of the XN-NN bond. Consequently, covalent azides are more sensitive explosives than are ionic azides.

Despite our understanding of the physical properties and the details of the molecular potential energy surface, prior to the work reported here, nothing was known of the decomposition of condensed phase FN_3 . Consequently, much of the work in this report was guided by the results of previous gas phase studies. The gas phase thermo- and photo-chemical dissociation of fluorine azide has been fully examined,^{2,6} and excited state NF species are found to be nascent dissociation products regardless of whether dissociation occurs via an excited state FN_3 surface or via the ground state potential energy surface. Since FN_3 can be viewed as a metastable complex of the NF(a) molecule and N_2 , the combustion chemistry of the material is likely to parallel the chemistry of the NF(a) and the NF(X) species. NF(a) is not an exceedingly reactive species, though it readily undergoes $\text{NF(a)} + \text{NF(X)}$ collisional quenching with a variety of collision partners.⁷ Very little NF(X) chemistry has been experimentally elucidated, although arguments have been made regarding the superior reactivity of this species.⁸

The work presented here is the first such complete quantitative study of the combustion of condensed phase fluorine azide. To assess the important parameters in the decomposition of this type of high energy density material, we have developed a methodology for producing, characterizing and reliably igniting cryogenic fluorine azide films. Additionally, the results of several experiments designed to elucidate the decomposition mechanism for solid FN_3 are reported. Potential methods for stabilizing these explosive films which have been identified via these experiments are also presented. Finally, the results of experiments which assess the effectiveness of two stabilizing additives are detailed.

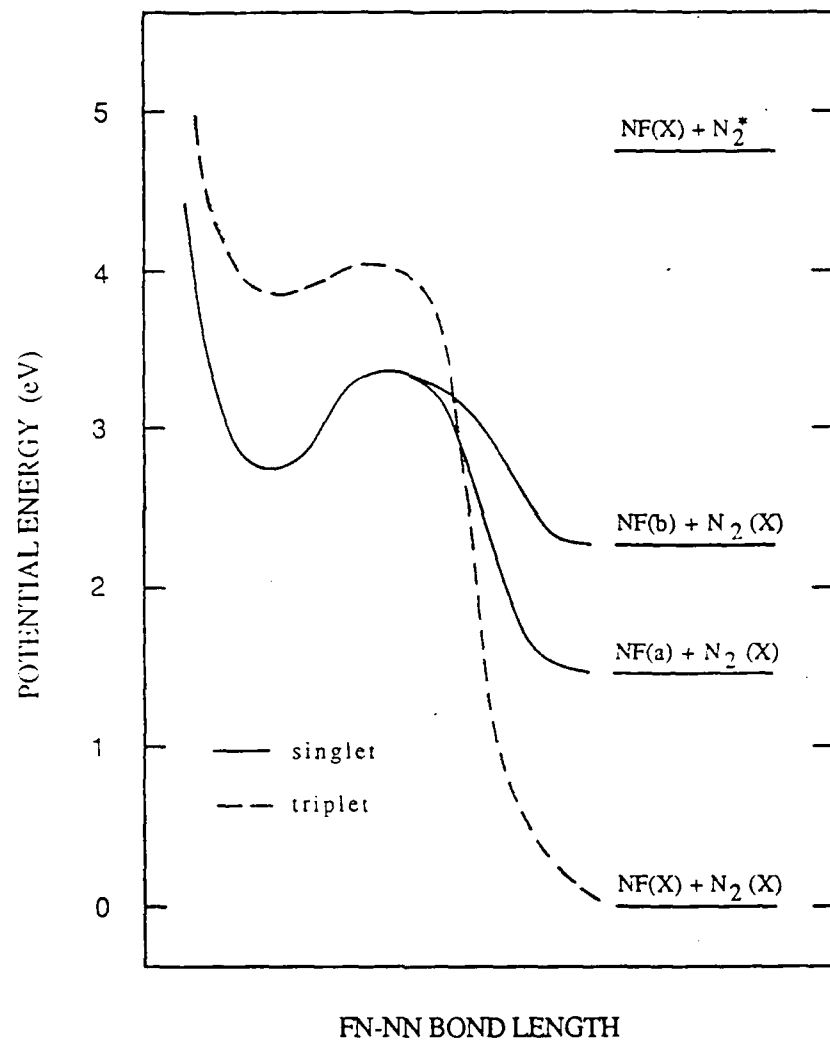


Fig. 1 Potential energy curves of fluorine azide.

2.0 EXPERIMENTAL DETAILS

In the following subsections the techniques used to safely synthesize and characterize a continuous pure flow of FN₃ are detailed. Also, the methods used to form, characterize, ignite and monitor the combustion processes of cryogenic films of the azide material are presented.

2.1 Synthesis of Fluorine Azide

Fluorine azide was synthesized in a continuous manner using a variation of the method of Haller.¹ FN₃ was generated by reacting HN₃ with F₂: HN₃ was produced by the thermally activated reaction of NaN₃ with stearic acid.⁹ The NaN₃-stearic acid reaction was found to have several advantages over the NaN₃-H₂SO₄ reaction as a method of HN₃ production. Specifically, the stearic acid reaction produced a bone dry flow of HN₃. In contrast, the sulfuric acid reaction required a downstream CaSO₄ trap to remove water. Furthermore, explosive compounds were noted to be formed around metal fittings between the CaSO₄ trap and the HN₃ generator. CaSO₄ was also found to significantly attenuate the HN₃ flow, raising the possibility of explosive compound formation in the trap. In addition to being 'cleaner', the NaN₃ reaction displayed more day-to-day predictability, yielded a more constant and controllable output and produced reaction by-products (solid sodium stearate) which were more easily handled and discarded. A schematic diagram of the FN₃ generator is shown in Fig. 2. Several of the important features of this device will be described in the following subsections.

Safety - Potential experimenters should be warned of the dangers of working with many of the compounds discussed in this report. FN₃ is a chemical deserving of much respect. It is a primary explosive, having twice the stored energy per unit mass of TNT. The previously noted observations of Haller regarding the explosive force of this material have been confirmed in our laboratory as well. Detonations of microscopically thin (10-20 μm) films of this material routinely severely cracked the 1 inch diameter 0.25 inch thick CaF₂ substrates used to support the films.

To handle FN₃ safely, particular care must be exercised to prevent condensation of any significant quantity of the liquid or solid. Also, reaction of the gas with other materials to form other explosive compounds is a serious potential problem.

Haller¹ reports that FN₃ gas can be adsorbed irreversibly on KF at room temperature to form a compound that explodes upon heating. We have found that an explosive film, most likely copper azide, is formed when FN₃ gas is passed over copper metal. By keeping the fluorine azide concentrations below 10 Torr, using only glass, teflon or stainless steel for construction, and avoiding condensation of large amounts of the material, we were able to prevent accidental explosions. 'Flashbacks' were occasionally observed in the teflon lines used to transport the material. We strongly recommend the use of blast shields, sand fills, barricades and other safety features as discussed in the following subsection.

The HN₃ which is produced during the synthesis of FN₃ has similar explosive tendencies. Thus, equal attention to safety is required. Procedures for handling NaN₃ are available from the manufacturer. While less energetic than FN₃ and HN₃, NaN₃ is, nevertheless, an energetic material which is capable of spontaneous decomposition if activated by excessive heating or friction. Also, NaN₃ can react with acids to form HN₃, and with metals to form explosive metal azides. All azides are highly toxic; thus, care must be taken to prevent exposure.

HN₃ Generator - Figure 3 shows a cross sectional view of the HN₃ generator subassembly. A 2 liter Kimax reaction kettle containing the NaN₃ and stearic acid was supported inside a 400 watt electric deep fat fryer by a stainless steel support structure. The temperature of the cooking oil which filled the pot was measured with a metal band thermometer. Stainless steel cooling coils in the annulus between the reaction kettle and the pot were attached to a source of tap water. In an emergency or at the end of an experiment, quenching of the NaN₃- stearic acid reaction was achieved via cooling the oil bath through admission of water into the cooling coils. A heavy stainless steel lid placed on top of the reaction kettle was sealed to the ground glass mating surface by a Viton O-ring. The helium carrier gas entered the kettle via an electronic mass flow meter, a vacuum regulator and the steel lid. The regulator was set to maintain a 350 torr absolute pressure inside the kettle. The helium flow was maintained at 3.5 sccs. A 1 RPM gear motor with a 600 in. oz. torque shaft rating was mounted on top of the lid. A teflon coated paddle was mated to the motor shaft and passed through the lid via a Viton O-ring seal. Operation of the HN₃ generator without

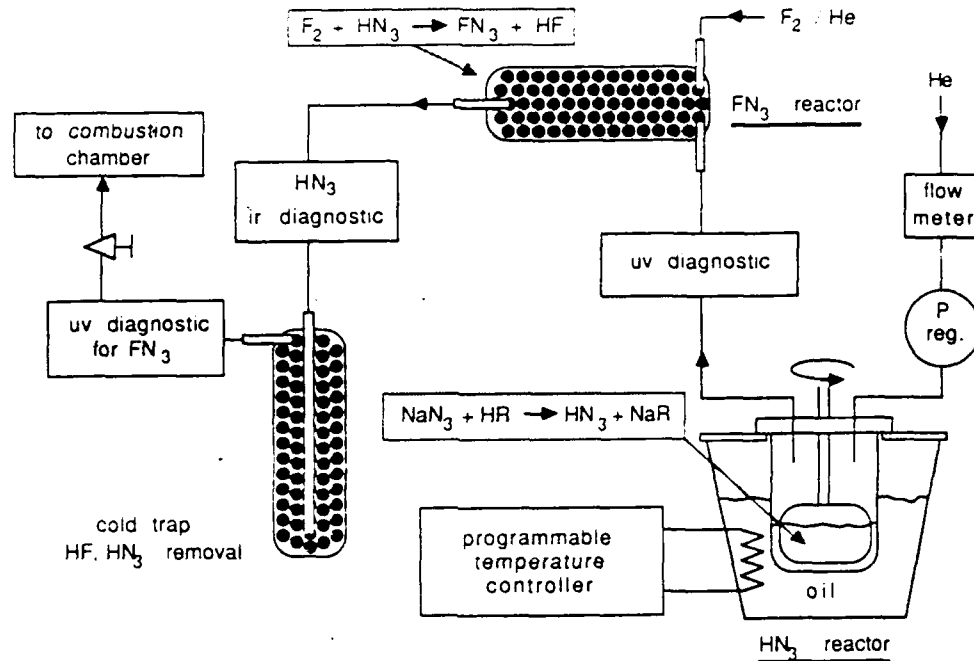


Fig. 2 Schematic diagram of fluorine azide generator.

stirring caused the yield to fall off quickly, raising concerns about the possibility of explosion in the event of stir-motor failure. Consequently, the entire HN_3 generator subassembly was operated inside a vented 0.25 in. thick lexan blast enclosure which was located inside a conventional fume hood.

FN_3 Generator - Contrary to Haller's observations,¹ copper was found to be incompatible with FN_3 . Mixing of HN_3 and F_2 over copper shot produced very little FN_3 and the shot became coated with a greenish compound. This compound exploded when struck forcefully with a hammer. Therefore, the $\text{HN}_3\text{-F}_2$ reaction was conducted inside a 0.6 liter stainless steel cylinder which was packed with 0.25 in. dia. stainless steel balls. The $\text{HN}_3\text{-He}$ flow was admitted to this reactor along with an adjustable flow of 8-10% F_2 in He through a nozzle which prevented rapid mixing of the reagents. A copper tube carrying resistively heated tap water was soldered onto the exterior of the reactor to allow maintenance of constant reactor temperature.

Cold Trap - The output gases of the FN_3 reactor were passed through a cold trap to remove the HF by-product of the $\text{HN}_3\text{-F}_2$ reaction and any residual HN_3 . Early experiments which utilized a NaF trap were discontinued because the FN_3 was severely

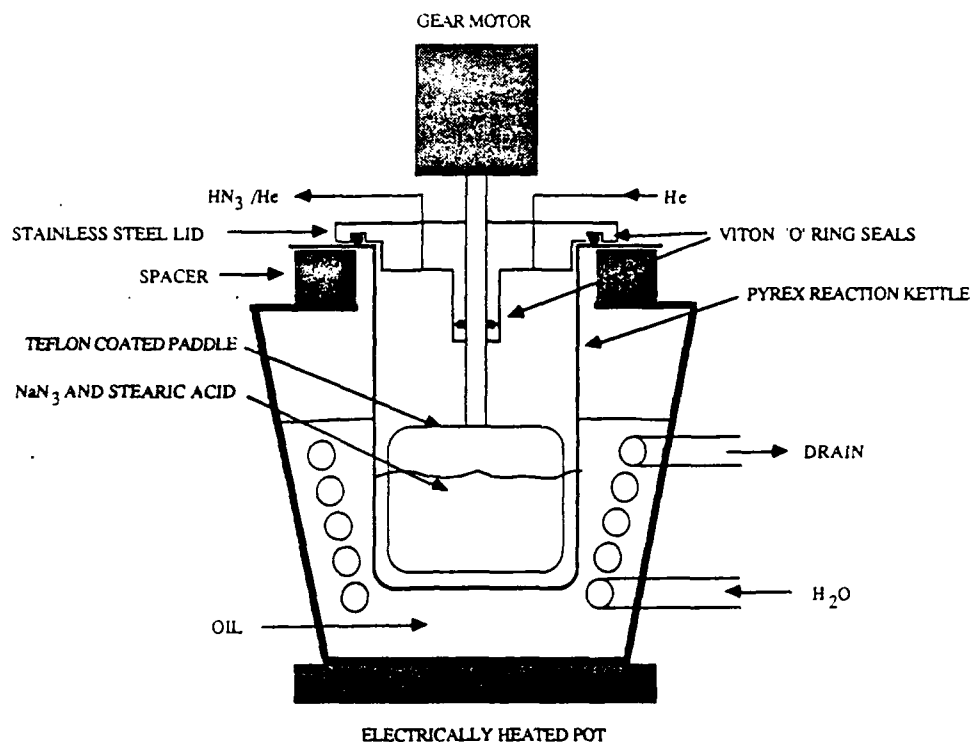


Fig. 3 Detailed view of HN_3 generator.

attenuated, again, raising concerns about eventual trap detonation. The trap was constructed of a 0.3 liter stainless steel cylinder having a dip tube. One third of the trap was filled with 0.25 in. dia. stainless steel balls. A copper cooling coil, soldered to the exterior, was connected via insulated lines to a sealed 5 liter liquid nitrogen dewar. To cool the trap, two 50 watt, 10 ohm power resistors in the bottom of the dewar were used to boil off 77 K nitrogen. The lid of the dewar was spring loaded to provide pressure relief. The temperature at the base of the trap was monitored with a thermocouple gauge. The dewar power resistors were powered by a Variac and a 120 to 24 volt stepdown transformer rated at 100 watt. Since unintentional condensation of either HN_3 or FN_3 in the trap could lead to detonation, the trap was buried inside a sand filled aluminum cylinder having 1 in. thick walls. This trap-assembly was further barricaded inside a vented 0.25 in. thick lexan blast shield which was housed inside a conventional fume hood. The sand was kept dry with a continuous purge of N_2 through the base of the aluminum cylinder. With this arrangement, trap temperatures of -100°C could be

maintained for approximately 1 hr. with a single dewar fill of liquid nitrogen. The trap was typically operated between -85°C and -92°C to effectively remove HF from the flow without significantly attenuating the FN₃ concentration (Fig. 4).

UV Cell - For diagnostic purposes, absorption cells were inserted in the lines following the HN₃ and FN₃ reactors and the cold trap. The first cell, located at the output of the HN₃ generator was operated at 253.7 nm using a Hg lamp as the source. The intensity of the lamp was attenuated by passage through a pinhole. The lamp supply was driven from a 60 watt constant voltage harmonic neutralized transformer to prevent line voltage induced variations of lamp intensity. The probing radiation was directed through a 0.5 in. dia., 25 cm pathlength stainless steel absorption cell which was outfitted with quartz windows. The radiation was then passed through a Hg resonance line interference filter and was detected by a 1P28 photomultiplier tube. With no HN₃ in the cell, a bias of 750 volts generated a steady photocurrent of 100 μ A. Under normal operating conditions, the HN₃ in the cell attenuated the radiation causing a 25-50 μ A reduction in output photocurrent. Based on the known extinction coefficient (10) of HN₃ at 253.7 nm, this reduction corresponds to a HN₃ yield of 2-4% relative to the flow. This diagnostic provided a continuous monitor of the HN₃ generator which was independent of other reactions occurring further downstream.

Preliminary experiments tested the operation of the HN₃ generator using a similar absorption cell of commercial design with a D₂ lamp source. Initially, the generator was charged with 2.0 mol stearic acid and 0.5 mol NaN₃. As shown in Fig. 5, application of constant heater power (using a Variac) produced an exponential approach to a constant temperature over several hours. At the same time, the yield of HN₃ (as measured by absorption) was found to initially increase with the rising temperature and then fall off as the NaN₃ concentration diminished. The flow rate of gas through the reactor was controlled by a downstream metering valve. Since the generator pressure was regulated, the total gas flow through the metering valve was constant. Consequently, as HN₃ gas evolved, less He flow was required to maintain the pressure in the reactor. The generation rate of HN₃ could, therefore, be monitored by the change of He flow through the mass flowmeter. Unfortunately, as the absorption signal began to diminish due to reagent depletion, the change in He flow continued to decrease, indicating that a second gaseous product was evolving in the HN₃ generator. It was theorized that this gas was CO₂. This product presumably results from second order

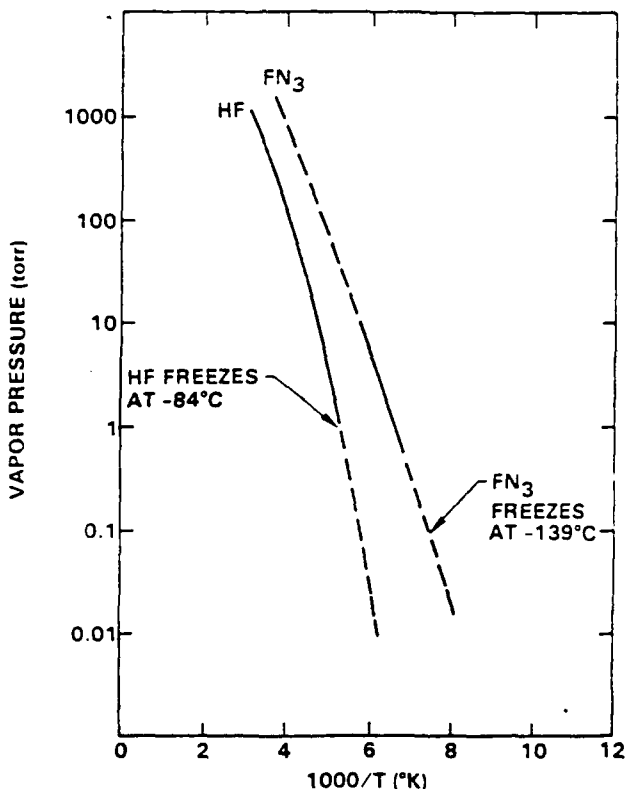


Fig. 4 Vapor pressure curves of FN_3 and HF.

reactions of the sodium stearate by-product. To test this hypothesis, the experiment was repeated with the amount of NaN_3 reduced to 0.1 mole. The flow rate of the He carrier gas was adjusted to the same level in both experiments to give approximately the same HN_3/He ratio, permitting measurement of HN_3 yield with the same diagnostic. As shown in Fig. 6, reducing the NaN_3 mole fraction had the intended effect. Therefore, the mole ratio of NaN_3 to stearic acid used in all subsequent experiments was 1 to 20.

IR Cell - The output of the FN_3 generator was passed through an infrared absorption cell. The function of this cell was to detect residual HN_3 without being affected by interferences from FN_3 or HF. Haller¹ found that excess F_2 reacted slowly with FN_3 to yield NF_3 and N_2 . Consequently, the FN_3 yield peaks when the HN_3 and F_2 flows are titrated. Also, it was undesirable to condense residual HN_3 in the cold trap. Therefore, the residual HN_3 diagnostic was required. The selection of an infrared wavelength of $3.0 \mu\text{m}$ for this diagnostic was based on knowledge of uv, vis and ir absorption spectra of FN_3 , HN_3 and HF.^{3,10,11}

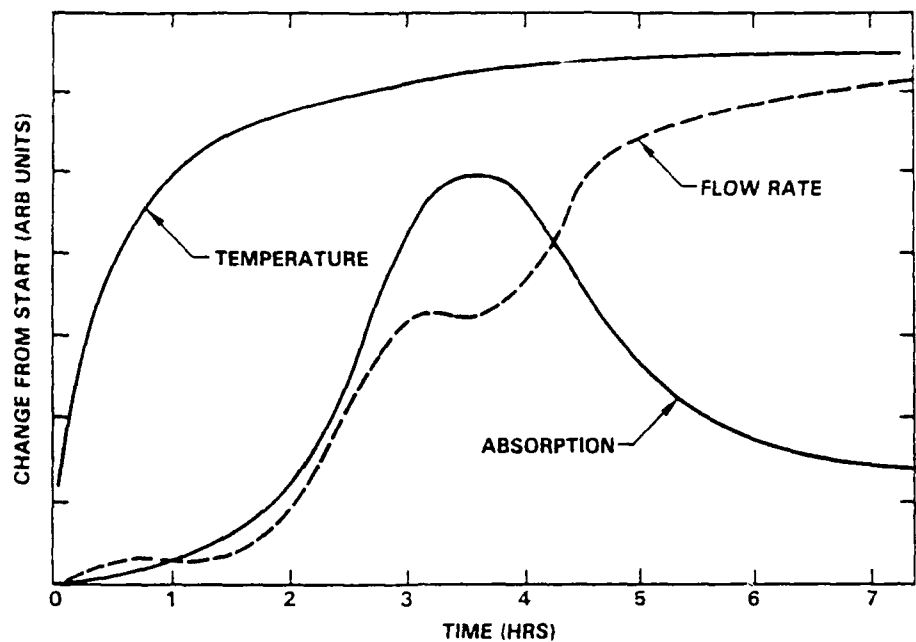


Fig. 5 Temporal behavior of HN_3 generator with constant heater power and 0.5 mol NaN_3 with 2.0 mol stearic acid.

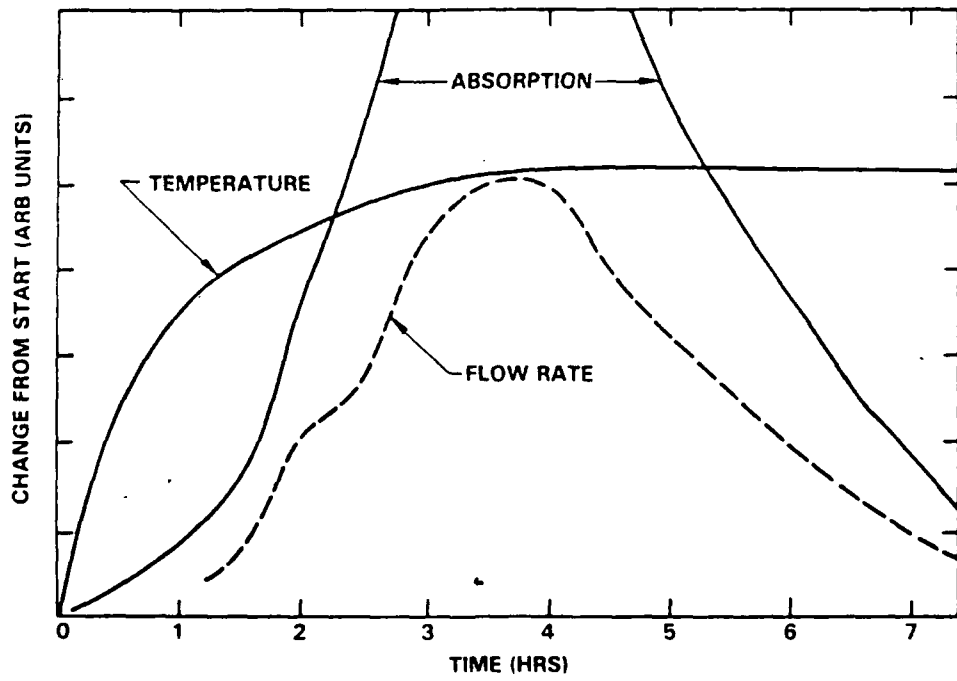


Fig. 6 Temporal behavior of HN_3 generator with constant heater power and 0.1 mol NaN_3 with 2.0 mol stearic acid.

The infrared diagnostic diagrammed in Fig. 7 was constructed of a 19 mm O.D. Suprasil quartz tube. The 1 meter long tube was equipped with sapphire windows on both ends. The radiation source was a temperature regulated 900°C blackbody emitting through a 3 mm dia. aperture. A 1 KHz mechanical chopper was interposed between the blackbody and the cell entrance window. The chopped output radiation was detected by a room temperature $0.4 \times 0.4 \text{ cm}^2$ PbSe semiconductor detector that was biased at 75 volt. Output photocurrent was passed to a lock-in amplifier via a 2 pole RC bandpass filter to limit out-of-band noise. The lock-in amplifier was referenced to the chopper. Typically, with 10 seconds of integration, 100 μV signals, having a signal-to-noise ratio of approximately 10, were recovered.

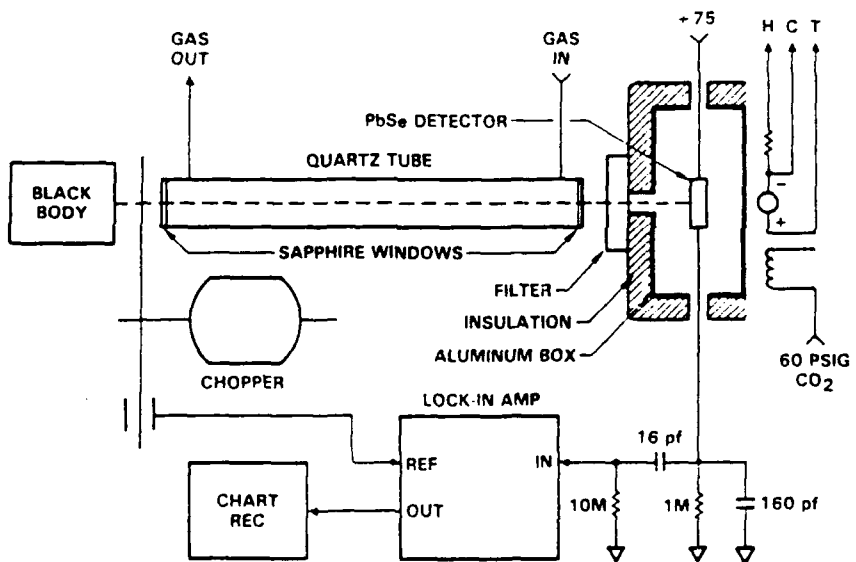


Fig. 7 Schematic diagram of infrared absorption diagnostic.

Signal amplitudes were, however, found to be sensitive to variations in the temperature of the detector. It was, therefore, necessary to stabilize the detector temperature. A copper plate carrying a resistive heater, a temperature sensing element and a small expansion nozzle was fit to the back of the box which housed the detector. The entire assembly was encased by fiberglass insulation. Application of 60 psig of CO_2 to the nozzle produced a steady cooling action which was counteracted by the resistive heater to maintain a constant temperature. The feedback circuit shown in Fig. 8 was

employed to maintain the proper resistor current. The circuit was adjusted to balance at room temperature, and the test point was monitored with a voltmeter to check the feedback stability. From the amplitude and the frequency of the stable oscillation of the test point about the mean, it was possible to calculate that the temperature variation at the sensor was less than $\pm 0.1^\circ\text{C}$. Application of the temperature stabilizing circuit cured the drifts in the detector output.

The infrared diagnostic was tested by using it in series with a commercial ultraviolet absorption cell while operating the HN_3 generator. The results are shown in Fig. 9. Clearly, the infrared and ultraviolet diagnostics track the same species; the infrared diagnostic being 'noisier'. The baseline drift of the ultraviolet diagnostic was traced to adsorption of HN_3 onto the windows of the absorption cell.

Programmed Power Supply - The time profiles of HN_3 shown in Figs. 5, 6 and 9 were still problematical with respect to yield variation during the course of the experiments, since continuous adjustment of the F_2 flow was required to maintain an optimal titration of the HN_3 flow. Therefore, the circuit shown in Fig. 10 was employed to program the power to the oil bath of the HN_3 generator in such a way as to counteract yield variation. The circuit operates by switching the heater on and off, and by slowly varying the on-off duty cycle. The circuit is designed to operate full power, at constant reduced power and at a power level that linearly increases with time, depending on the chosen position of a selector switch. Initially, the power is set to full until the oil bath reaches a specified temperature (155°C) and then the circuit is switched to reduced power for typically 3.5 hr. During this time the temperature falls to a constant level near 100°C and the HN_3 generation rate builds up in a rather complicated, yet reproducible manner, due to the slow melting of the stearic acid. Following this period, the HN_3 would begin to slowly decline due to reagent depletion if the temperature was held constant. Thus, to maintain constant HN_3 output the reactor temperature is slowly increased over the next 4 hr period by operating the circuit in the linear power ramp mode. The output of the HN_3 generator when operated in the described manner is shown in Fig. 11.

To achieve stable HN_3 output, the internal controls of the power supply must, of course, be adjusted to produce the temperature profile that is displayed in Fig. 11. The adjustments to the numbered control points on Fig. 10 achieve the following:

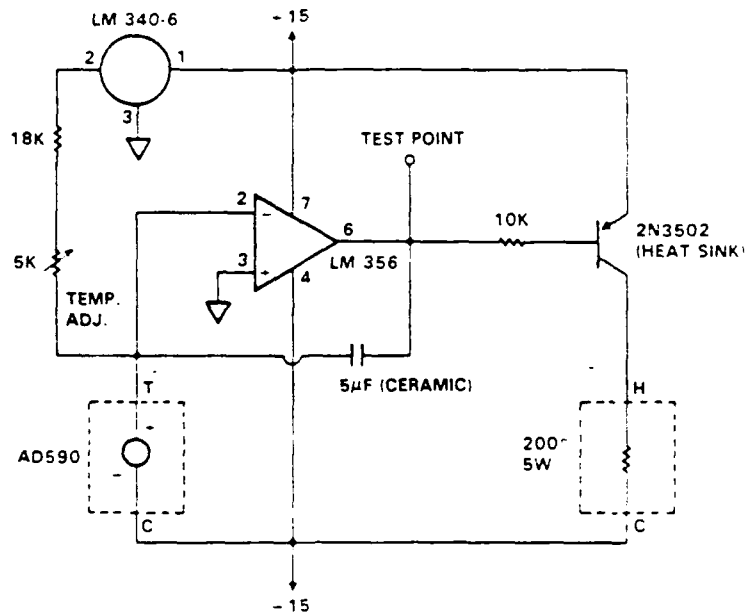


Fig. 8 Feedback circuit for temperature stabilization of PbSe detector.

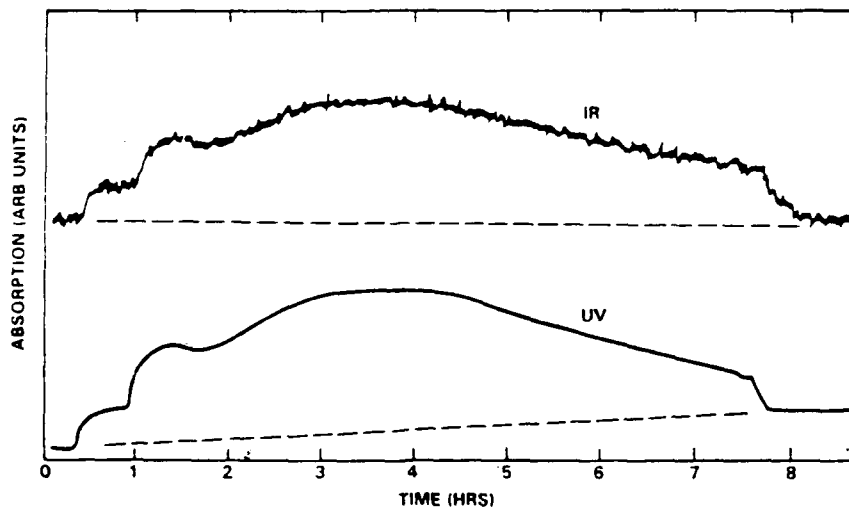


Fig. 9 Comparison of infrared and ultraviolet absorption diagnostic with constant heater power.

(1) controls the cycle rate and should be set for a 60 sec cycle period, (2) controls the continuity of the transition from low power to ramped power, (3) controls the low power setting, and (4) controls the amplitude of the ramp. These controls can be set relatively quickly by trial and error and by using control voltage measurements coupled with linear

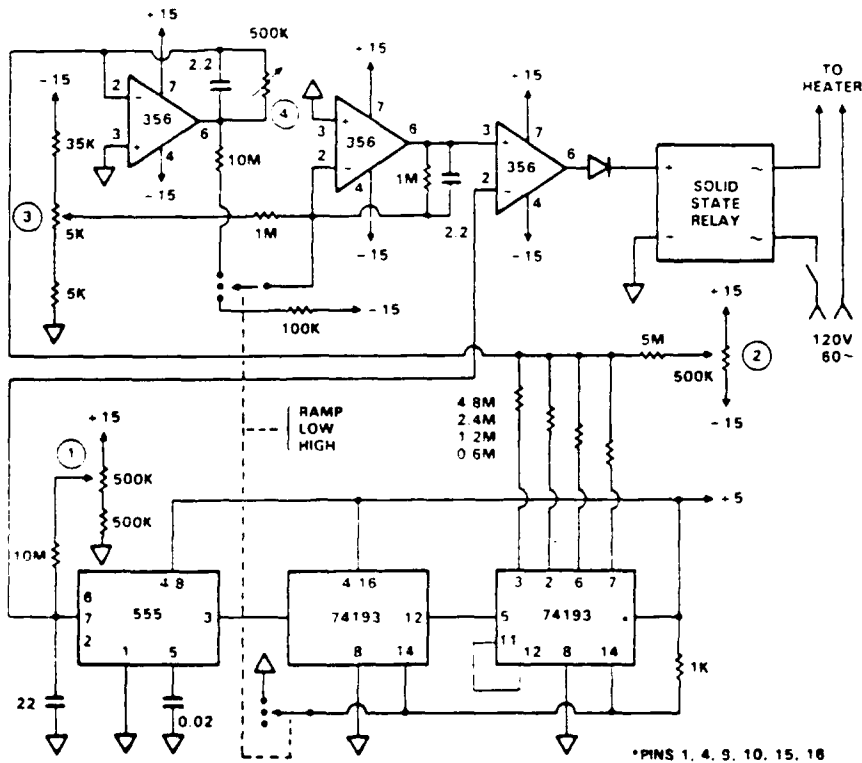


Fig. 10 Schematic diagram of programmed power supply used to stabilize HN_3 generation rate.

extrapolation of two or more experimental results to predict the desired control voltages. Once set, the stabilized production of HN_3 is quite reproducible if sufficient care is given to precise loading of the generator, the initial heating peak and the time of switch over to ramp power operation. The use of high heat at early times accelerates the melting of stearic acid and has a profound effect upon the HN_3 time profile.

As a safety measure, to prevent prolonged heating at high power, the automatic temperature control on the electric pot is set at 200°C . Normally, the pot will be cooler and the pot control will be inactive (always on). The pot controller will, however, prevent voltage provided from the programmed power supply from heating the oil beyond 200°C . This effectively provides protection against thermally induced decomposition on NaN_3 , which has an onset temperature of 250°C .⁹

Once the HN_3 yield was stabilized, it was possible to test the infrared absorption diagnostic during FN_3 generation. As shown in Fig. 12, following HN_3 yield

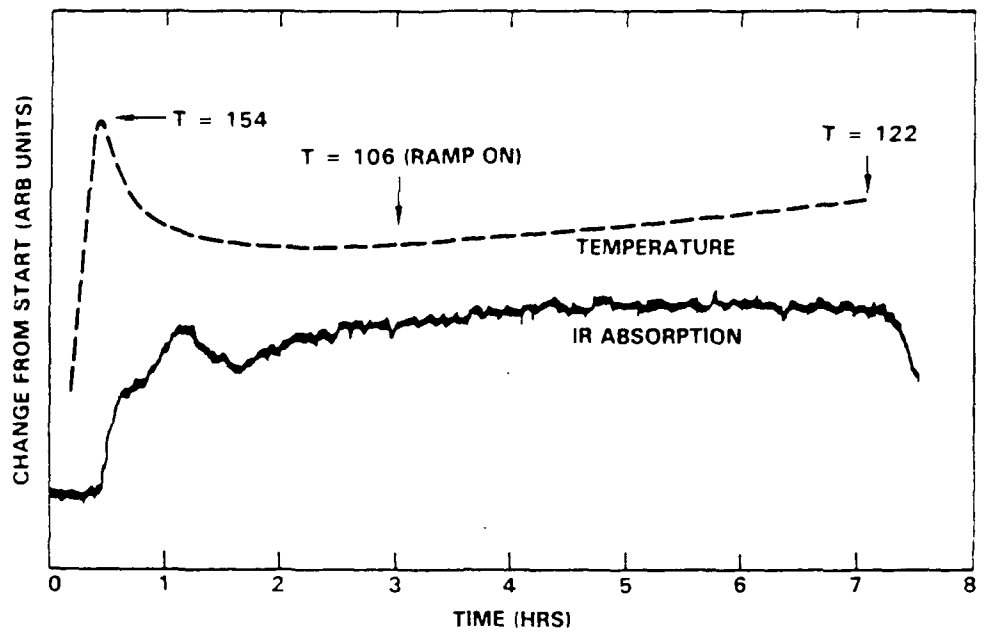


Fig. 11 Temporal behavior of HN_3 generator using programmed power supply.

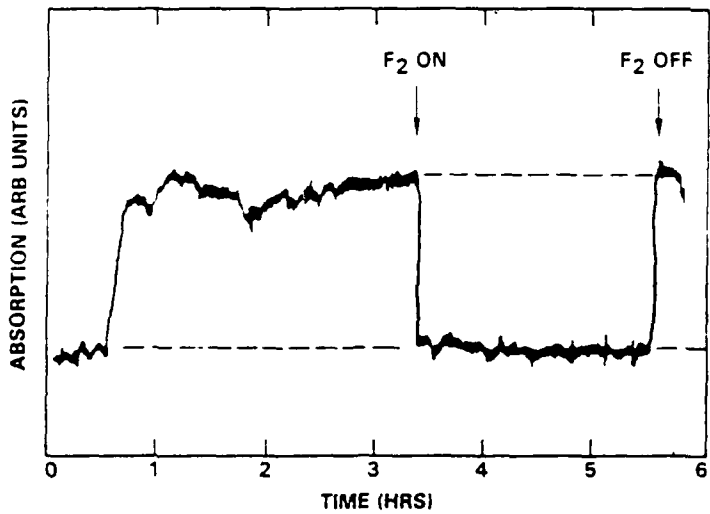


Fig. 12 Response of infrared absorption diagnostic to generation of FN_3 .

stabilization, the F_2 is added in sufficient quantity to react all of the HN_3 . The complete disappearance of absorption shows that the infrared diagnostic is insensitive to F_2 , FN_3 and HF. This apparatus has been found to be an effective and reliable monitor of the titration endpoint.

uv-vis Cell - Finally, after passage through the cold trap, the gas flow is passed into a 6 cm long stainless steel cell with quartz windows. The cell is placed inside a commercial spectrophotometer that is operated at 420 nm (tungsten lamp source). At this wavelength, FN₃ can be detected without interference from HF or HN₃.^{3,10,11,12} During a typical stabilized run, the 420 nm transmission decreases from 100% to 92-94%. Using Ghilivand's data for the extinction coefficient of FN₃,³ a yield of 7 Torr of FN₃ in 350 Torr He buffer was typically calculated. Also, the conversion efficiency of FN₃ to HN₃ was found to be 50-100%. The metering valve which controls the gas flow rate through the entire reactor was placed at the exit of the uv-vis absorption cell. After passage through the metering valve, the flow is directed through either 0.25 in. dia. stainless steel or teflon tubing to the experimental station where condensed phase FN₃ films are formed and studied.

Miscellaneous - Several additional features of the FN₃ generator, not shown in Fig. 3 are discussed below. Some of these features have significant safety consequences. Large area coarse glass frits were placed in the gas lines at the exit of the HN₃ and FN₃ reactors. These frits act as filters to stop entrainment of particulates. A frit is required downstream to the FN₃ reactor because solid NH₄F can be formed under conditions noted by Haller.¹ Also, the flow meter monitoring the flow of He into the HN₃ reactor was alarmed to provide an audible warning of the potential buildup of HN₃ if the flow stops due to vacuum pump failure, clogged valve, etc. The stainless steel balls in the FN₃ reactor should be checked for signs of corrosion or by-product deposits at regular intervals to prevent buildup of explosive compounds. With daily use of the apparatus, only trace amounts of NH₄F were observed upon routine inspection at 3 month intervals. Finally, while a small floor pump could provide the needed vacuum, the generator output was exhausted to a 300 cfm mechanical pump. To prevent significant accumulation of organic azides in the pump, the oil was changed on a monthly basis.

FN₃ Holding Tank - For safety reasons the output of the FN₃ generator could not be directly connected to the cryogenic film combustion chamber. Safe handling of FN₃ required, instead, that cryogenic films be formed from a small amount of the material which could be held in a storage tank. A schematic diagram of this holding tank and associated plumbing is shown in Fig. 13. The tank consisted of a 4 liter teflon-lined stainless steel vessel which had a cooling coil brazed to the exterior. The tank was

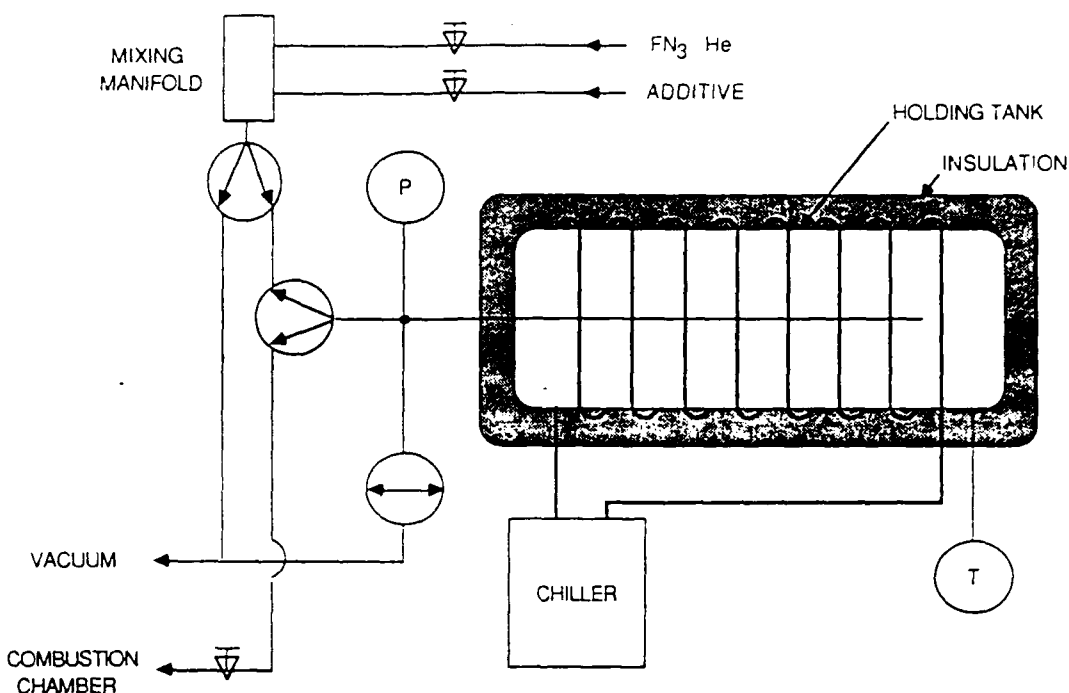


Fig. 13 Schematic diagram of FN₃ transfer and storage system.

wrapped with an insulating blanket. The cooling coil was attached to a closed loop chiller which used a water-ethylene glycol mixture as coolant. For many of the initial experiments, the tank was cooled to approximately 8°C (the minimum temperature achievable with the chiller used). The tank was cooled because both Haller¹ and Gholivand³ observed that FN₃ decomposes to N₂F₂ and N₂ slowly in the gas phase at a rate which is strongly temperature sensitive. On the basis of Gholivand's³ measurement of an increase in half-life from 20 minutes to 5 hr. for a 5 mbar sample that was cooled from room temperature to 0°C, even the modest chilling performed here was expected to substantially increase the FN₃ tank lifetime. (These workers also note that the lifetime is pressure dependent.)

The cooled tank was typically filled to 100 Torr with the 4% FN₃-He mixture, enough material to form several cryogenic films. After obtaining several non-reproducible experimental results, it was suspected that the lifetime of FN₃ tank fill was much less than anticipated. Mass spectrometric analysis of the holding tank output as a function of time showed that, indeed, the magnitude of the mass 66 (N₂F₂) signal

increases and the mass 61 (FN_3) signal decreases. As shown in Fig. 14, the half-life of the FN_3 in the holding tank under the conditions noted here is approximately 1 hr. After this discovery, a new chiller, capable of attaining lower tank temperatures (-4°C), was installed. The methodology of our experimentation was also altered: The holding tank was completely replenished with a fresh fill of FN_3 prior to collecting any presentable data. This is necessary because, as will be shown, ignition and combustion phenomena can be profoundly affected by even trace levels of impurity.

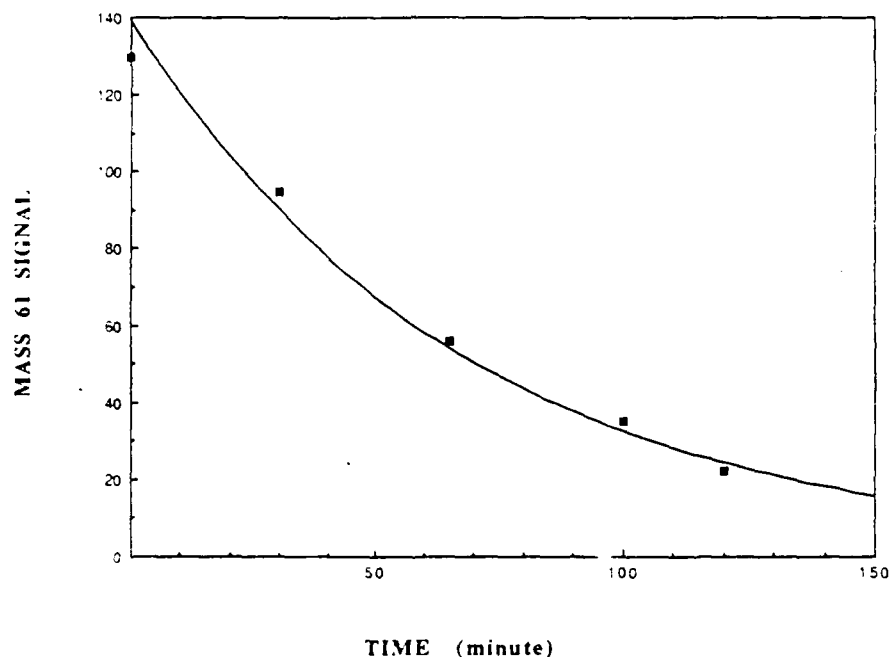


Fig. 14 Magnitude of the FN_3 mass signal in the 8°C holding tank gases at various times.

Gas Sample Characterization - The holding tank gases were also characterized by fourier transform infrared spectroscopy. Figure 15 shows the FTIR spectrum of a sample of gas phase FN_3 that was drawn from the holding tank and flowed through a 166 mm stainless steel absorption cell having KBr windows. The observed frequencies are tabulated in Table I in addition to the absorption frequencies and assignments for gas phase FN_3 as reported by Gholivand.³ There is close agreement between the two data sets for the bands of FN_3 . Several other absorptions were observed, as well. The $2360\text{-}2340\text{ cm}^{-1}$ PR bands and the 667 cm^{-1} band are undoubtedly CO_2 absorptions. This

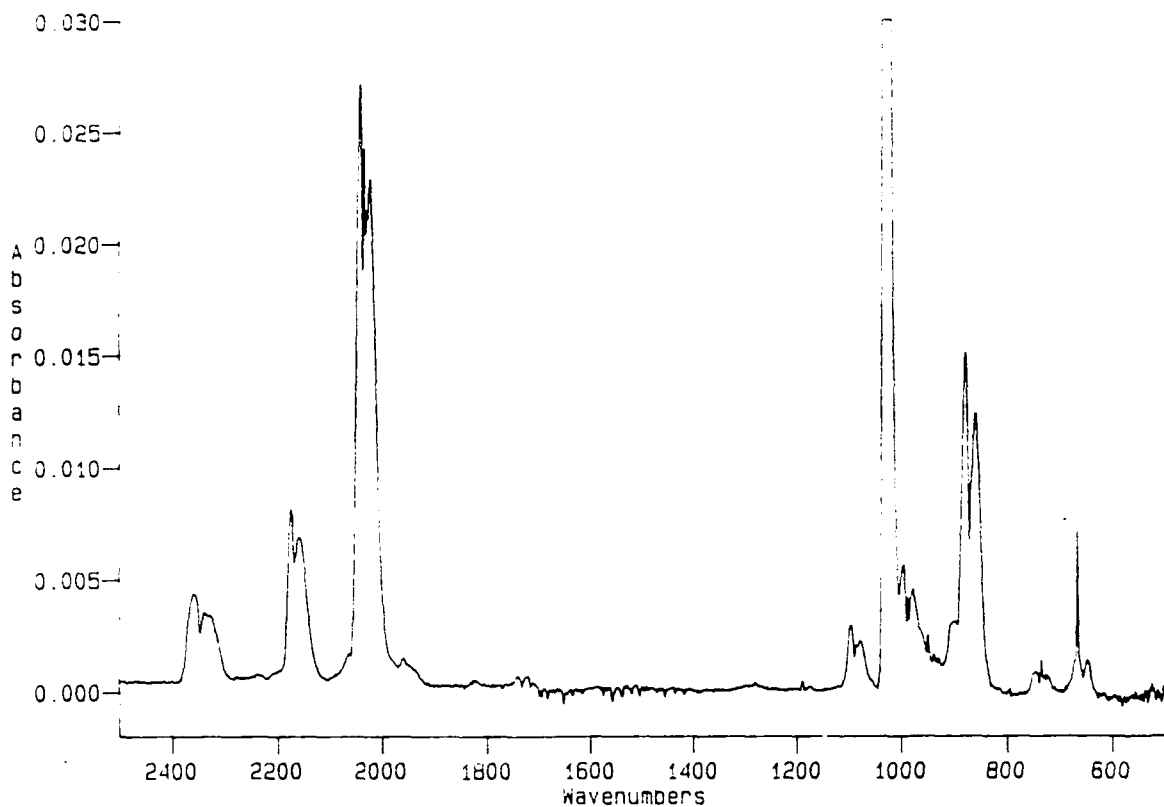


Fig. 15 Gas phase infrared spectrum of holding tank stored FN_3 .

species, as mentioned earlier, is known to be produced in the HN_3 reactor. Additionally, CO_2 has a substantial vapor pressure at -100°C , and would thus not be completely trapped by the generator cold trap.

Some of the other absorptions can be identified as those of cis and trans N_2F_2 . The strong gas and condensed phase absorptions of these species have been previously reported^{13,14} and are tabulated in Table 2. On the basis of the known intensities of the listed transitions, it is expected that if each species is present with comparable concentration, the ν_5 , ν_2 and ν_6 bands of the cis species and the ν_5 band of the trans species will be observed with comparable intensity. The two combination bands of the trans species (Table 2) are 40-fold less intense than the ν_5 band, and thus may not be observable. Through close examination of Fig. 15, the PQR structure of the ν_5 band of trans can be identified as the 998.0 -, 989.3 - and 979.9-cm^{-1} features. The PQR absorption features at 747.0 -, 736.9 - and 725.2-cm^{-1} are assigned as the ν_6 band of cis

Table I
Assignments of Infrared Absorption Bands Observed in Holding Tank Gas

<u>This Work</u>	<u>Gholivand (3)</u>				
<u>absorption</u> (cm ⁻¹)	<u>Δv (PR)</u> (cm ⁻¹)	<u>intensity</u>	<u>absorption</u> (cm ⁻¹)	<u>Δv (PR)</u> (cm ⁻¹)	<u>assignment</u>
2176.0	16.5	s	2171.5	16	2v ₂
2159.5					
2044.1					
2035.8	19.2	vs	2037.0	20	v ₁
2024.9					
-----	---	w	1953	18	v ₂ + v ₃

1741.8	20.1	vw	1736.0	18	2v ₃
1721.7					
1096.8	17.3	m	1090	18	v ₂
1079.5					
903.0		sh	897		v ₄ + v ₅
880.8	18.7	s	873.5	17	v ₃
667.3	18.9	m	658	16	v ₄

other observed absorptions					
2360				CO ₂	
2335					
667.3				CO ₂	
1034					?
1029					
998.0				trans N ₂ F ₂	
989.3					
979.9					
951.8				cis N ₂ F ₂	
747.3				cis N ₂ F ₂	
736.9					
725.2					

Table 2
Infrared Absorptions of cis and trans N₂F₂
Intense infrared absorptions of N₂F₂ (13,14)

cis N ₂ F ₂ (gas)			trans N ₂ F ₂ (gas)		
(cm ⁻¹)	assignment	intensity	(cm ⁻¹)	assignment	intensity
952	v ₅	vs	990	v ₅	vvs
896	v ₂	vs	1581	v ₃ + v ₅	s
737	v ₆	vs	1993	v ₂ + v ₅	s

trans N ₂ F ₂ (solid)		
(cm ⁻¹)	assignment	intensity
970	v ₅	vvs
1552	v ₃ + v ₅	s
1995	v ₂ + v ₅	s

N₂F₂. Similarly, the feature at 956.1 cm⁻¹ is identified as the Q branch of the v₅ band of the cis species. The v₂ band of this species is obscured by the presence of the intense v₃ and (v₄ + v₅) bands of FN₃ in the 950-840 cm⁻¹ region of the spectrum.

The remaining unidentified feature in the spectrum shown in Fig. 15 is an intense 1034-1029 cm⁻¹ band. A blown up view of this region of the spectrum is shown in Fig. 16. Possible absorbing species are: HN₃, HF, N₂F₄ and NF₃. HF can immediately be ruled out, as this species displays a classical well resolved broad vibrational/rotational band at very high frequency (ca. 3600 cm⁻¹). As the v₁ band of the NF₃ species reportedly¹⁵ appears at 1031 cm⁻¹, the band of Fig. 16 is potentially identified. However, the most intense absorption of NF₃ is the doubly degenerate v₃ mode at 907 cm⁻¹. Since no absorption of intensity comparable to the 1034-1029 cm⁻¹ band is observed at 907 cm⁻¹ in Fig. 15, it must be concluded that NF₃ is not present in this system. The infrared spectrum of the remaining candidate, HN₃, is displayed in Fig. 17. This spectrum is in close agreement with that observed by Pimentel.¹⁶ It is clear from a comparison of Figs. 15, 16 and 17 that HN₃ is not the contaminant responsible for the

unassigned absorptions. Finally, N_2F_4 exhibits very strong infrared absorptions at 1031-, 1023-, 1010-, 958-, 945- and 933-cm^{-1} .⁴⁵ As many of these bands are not apparent in Figs. 15 and 16, this species can also be ruled out. The absorptions highlighted in Fig. 16 are presently unassigned.

2.2 Formation and Characterization of FN_3 Films

In the manner described below, films were formed by spraying the FN_3 -He mixture onto a cooled substrate. Also, as will be subsequently described, the films were spectroscopically characterized to show that the FN_3 retains its chemical identity and to determine the identity in the film and concentration of film impurities.

Combustion Chamber - The films were formed, characterized and combusted in the chamber illustrated in Fig. 18. The combustion chamber contains a salt substrate mounted in a copper holder that was maintained at the boiling point of liquid nitrogen. Typically, the substrate material was 6 mm thick, 25 mm dia. CaF_2 flats, although in many of the FTIR spectroscopic studies, NaCl and KBr optical windows were used. These optical flats were mechanically secured, and thermally coupled to the copper holder through a crushed gasket of indium wire. As shown in Fig. 18, the cryogenic film was formed by spraying the FN_3 onto the cooled substrate through a nozzle. The nozzle was constructed from a 0.25 in. dia. stainless steel tube, one end of which was constricted to a diameter of 0.013 in. The nozzle was coupled into the chamber via an Ultatorr vacuum fitting. This permitted variation of the nozzle-substrate distance, providing effective control over FN_3 film thickness and topology. The chamber was initially constructed with a nozzle-substrate distance which was fixed at a distance which was too close to the substrate. Consequently, in many of the earlier experiments the studied films did not have a uniform topology. Rather, they displayed a 'mountainous' appearance, being thicker in the center than at the edges. Upon ignition, these films routinely caused the substrate material to shatter, reducing the experimental duty cycle. By trial and error, the proper nozzle-substrate distance for formation of films having a uniform topology was found. Substrate shattering then became a rare occurrence.

A substrate cleaning procedure was instituted upon observation that films occasionally failed to form on SiO_2 substrates. During the phase of this research involving characterization of the emission spectrum of the combustion products, the

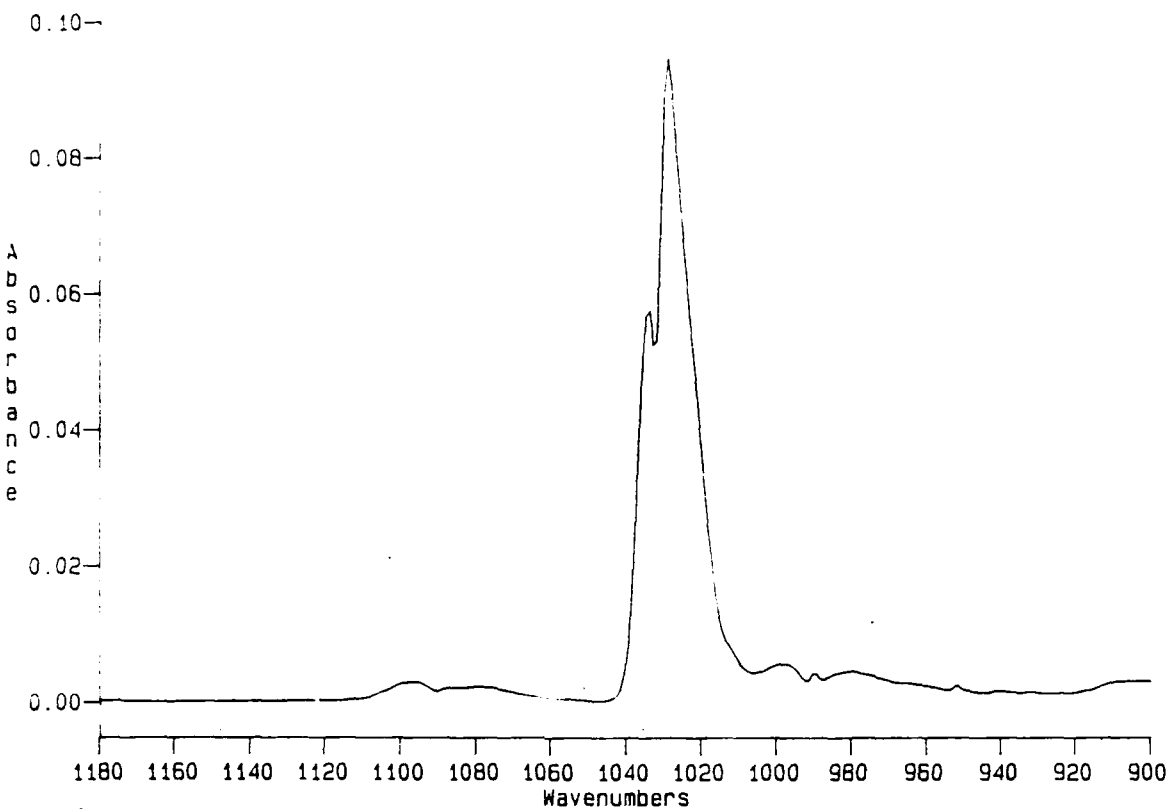


Fig. 16 Expanded view of the 1000 cm^{-1} region of the gas phase FN_3 spectrum.

substrates were discharge cleaned in situ via the following procedure. The nozzle was connected to a miniature neon sign transformer having a secondary rating of 3000 volt at 18 milliamp and the copper substrate support block was grounded. A discharge was struck while flowing pure He through the nozzle at a pressure of 0.5 Torr. Prompted by observation of spurious bands in the emission spectrum of the FN_3 combustion products, the methodology of film formation was thoroughly scrutinized. The use of He ion bombardment to remove adsorbed species was discontinued when, upon close substrate inspection, it was noted that the discharge actually deposited a microscopic residue of what appeared to be a metallic substance. Subsequently, substrates were cleaned by swabbing with 200 proof ethanol.

As shown in Fig. 18, the vacuum chamber, housing the substrate-holder assembly, consisted of a stainless steel cube. Four sides of the cube were outfitted with 6 mm thick- 25 mm dia. CaF_2 Viton O-ring sealed windows. The chamber was exhausted to the previously mentioned 300 cfm mechanical pump. Chamber pressure and substrate

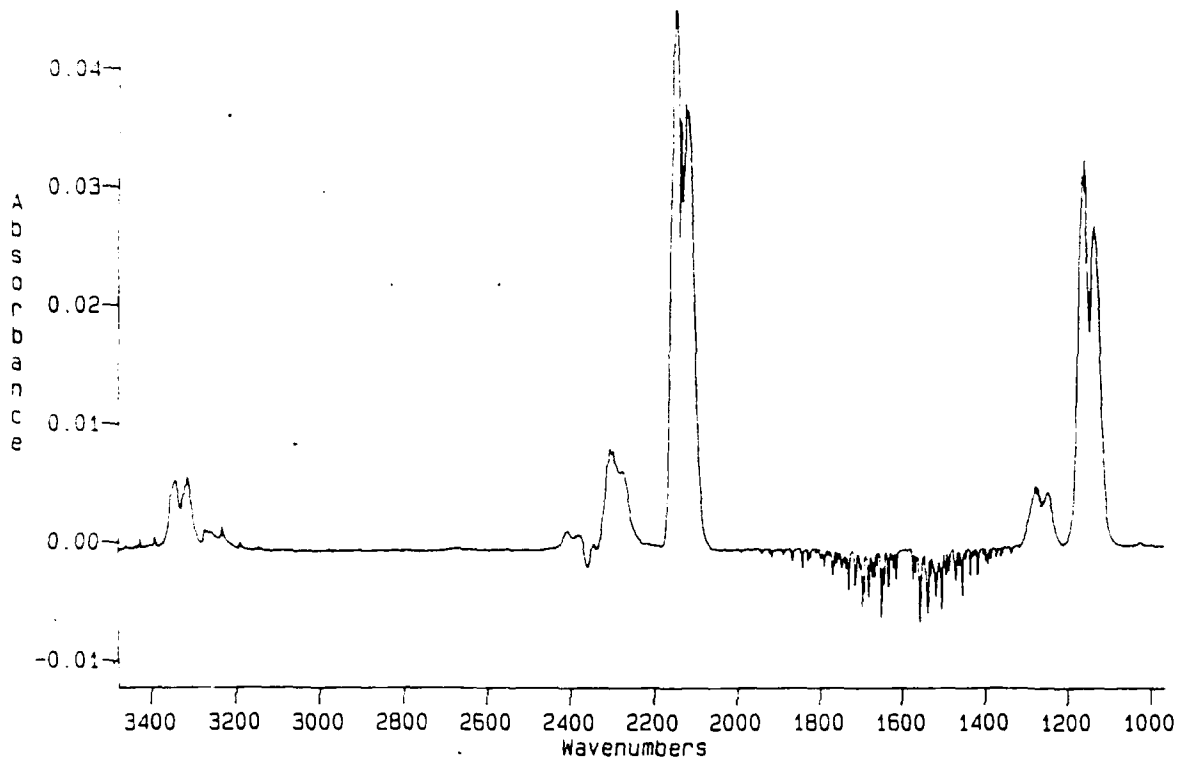


Fig. 17 Infrared spectrum of gas phase HN_3 .

temperature were monitored with a capacitance manometer and a thermocouple, respectively.

Film Characterization - The fluorine azide films have been both qualitatively and quantitatively characterized. Qualitatively, the films appear as a light yellow-tinged 'frost' to the naked eye. Also, they very strongly scatter direct light, permitting the previously mentioned estimate of uniformity. These observations are consistent with Brener's¹⁷ 'polycrystalline molecular solid' description of $\text{FN}_3(s)$. Since, in molecular solids, molecular identity is wholly retained, the spectroscopy of the gas and condensed phases should be very similar.

The visible absorption spectrum of a fluorine azide film is shown in Fig. 19. This spectrum was manually recorded using a tungsten lamp source and a 0.5 meter monochromator. The monochromator was equipped a cooled GaAs photomultiplier at the exit slit. As expected on the basis of the spectrum of gas phase FN_3 ,³ and the nature of molecular solids the only identifiable absorption in Fig. 19 appears at approximately

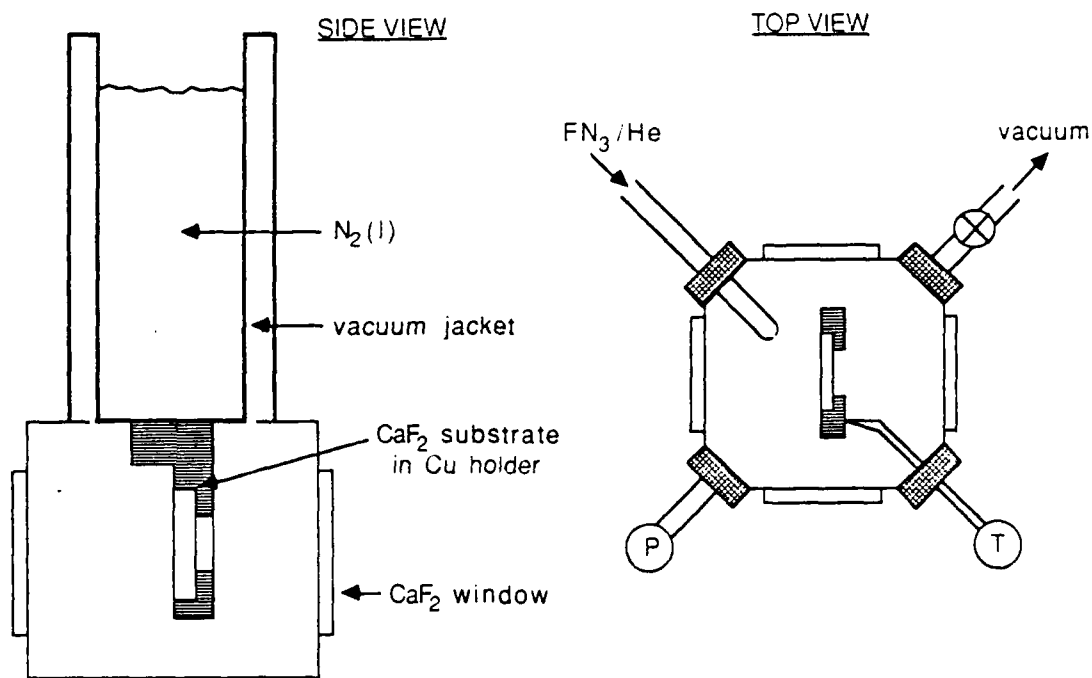


Fig. 18 Schematic diagram of azide film combustion chamber.

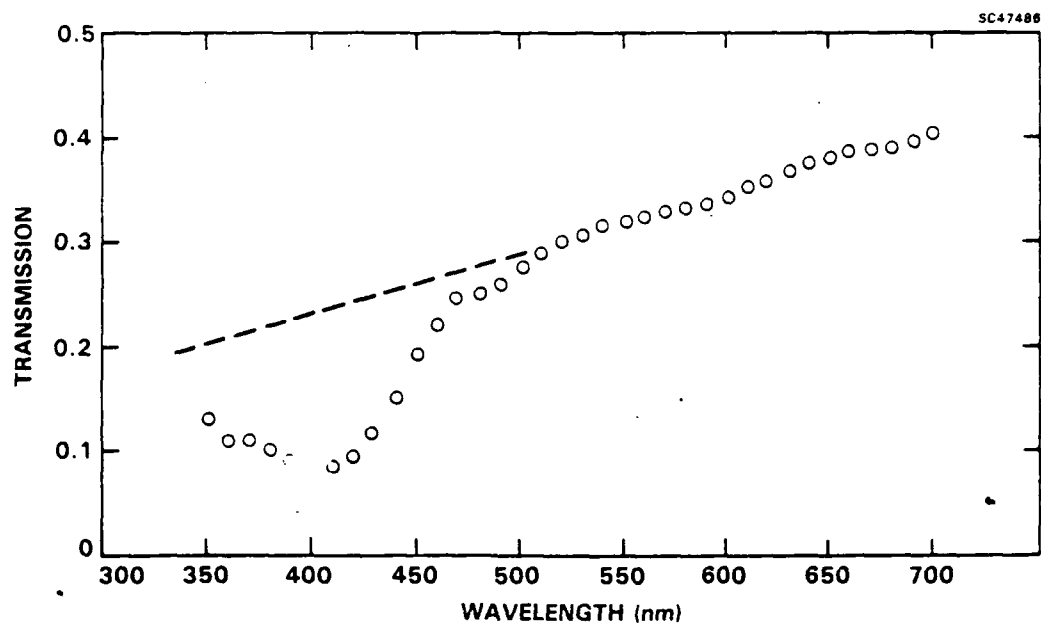


Fig. 19 uv-vis absorption spectrum of cryogenic FN_3 film.

420 nm. Also, the severely attenuated and sloping baseline is consistent with the high degree of scattering by the polycrystalline solid. Using Brener's¹⁷ calculated value for the density of solid FN₃ and Gholivand's³ measurement of the extinction coefficient for gas phase FN₃ at 420 nm, an estimate of approximately 10 μm for the film thickness can be deduced from I/I₀ made at 420 nm for several of the films studied in the experiments reported here.

The FN₃ films have also been characterized via infrared spectroscopy. The spectrum displayed in Fig. 20 was obtained for a film which was formed immediately after filling the FN₃ holding tank. The detonation chamber, equipped with a KBr substrate, was placed into the sample compartment of a BioRad FTS-7 fourier transform spectrometer to obtain this spectrum. It is the result of 16 scans at 2 cm⁻¹ resolution. The frequencies and assignments of the observed absorptions are listed in Table 3. Also tabulated are the published³ absorption frequencies for solid FN₃. Comparison of Fig. 20 with Fig. 15 and Table 1 with Table 3 indicates that, as expected for this molecular solid, the change in phase has relatively little effect on the vibrational spectrum. The bands of solid FN₃ are relatively narrower, but are centered at the same frequency. The major difference between Figs. 15 and 20 are due to impurity absorptions. Observed solid phase impurity bands can be identified as H₂O, CO₂ and N₂F₂, as the assignments of Table 3 indicate. Similar to the gas phase spectrum, an intense unidentified absorption appears at approximately 1040 cm⁻¹. From the observations presented in this section it is clear that the chemical identity of the FN₃ molecule is retained upon deposition onto the cooled substrate. Further, the films are relatively impurity free.

2.3 Ignition and Combustion Diagnostics

As illustrated in Fig. 21, several macroscopic changes to the fluorine azide film occur as a result of ignition. This figure shows the observable change to the bulk material and surroundings at various times subsequent to ignition. Following pulsed laser ignition at the center of the film, combustion intermediates and products are expelled from the surface, forming a gaseous plume. The decomposition proceeds from the ignition site into the unburned material in all radial directions along the surface. As this occurs even more gaseous species are propelled from the substrate, enhancing the development of the plume. There are several methods for interrogating this process, some of which are: (1) analysis of plume emission, (2) analysis of plume velocity,

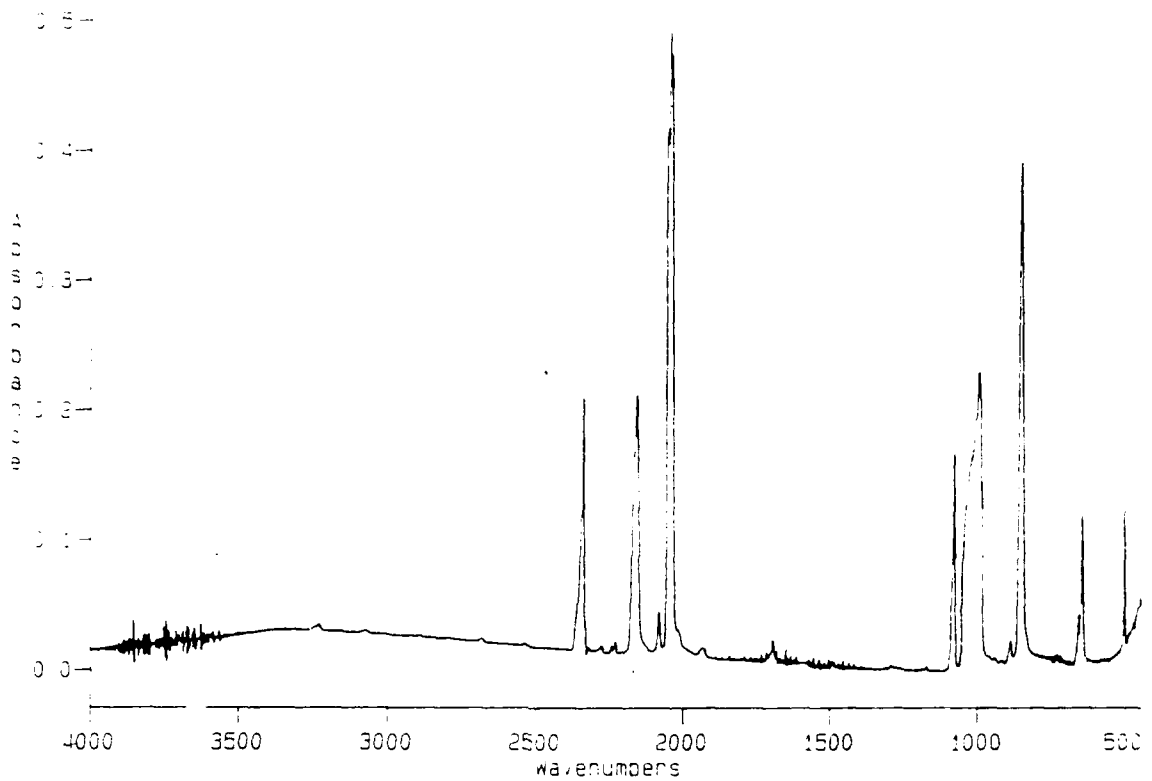


Fig. 20 Infrared spectrum of cryogenic FN₃ film on KBr substrate.

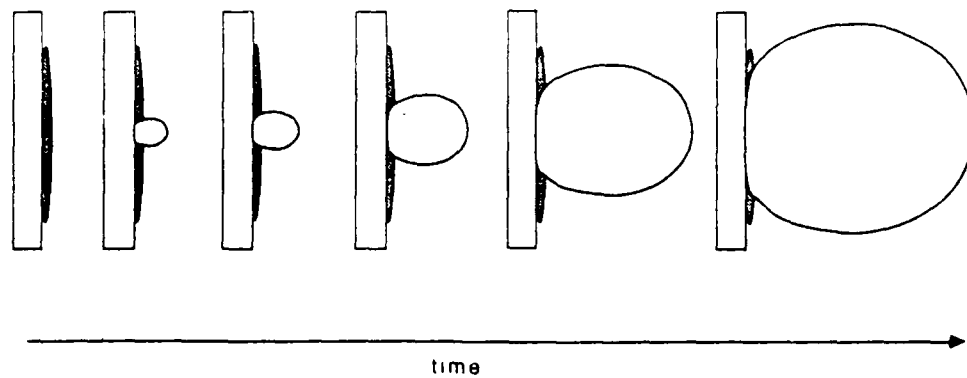


Fig. 21 Cartoon depicting evolution of burning azide film.

(3) analysis of material burn velocity and (4) analysis of ignition delay. The techniques used to affect these measurements are presently described.

Table 3
Assignments of Infrared Absorptions of Observed in FN₃ Films

IR absorptions of FN₃ (solid)

<u>this work</u>	<u>Gholivand (3)</u>	<u>intensity</u>	<u>assignment</u>
2168.9	2170	s	2v ₂
2162.6			
-----	2052	v s	v ₁
1941.4	-----	w	v ₂ + v ₃
1082.1	1084	v w	2v ₃
889.6	893	sh	v ₄ + v ₅
852.9	853	s	v ₃
660.4	649	m	v ₄
649.0			
505.8	505	w	v ₆

other observed absorptions

3300	ice
1697	
2342.1	CO ₂
667.8	
1040.7	?
992.6	
990.0	trans N ₂ F ₂ (?)

Ignition Lasers - In the experiments described in this report, the fluorine azide films have been ignited in one of two ways. In the emission spectroscopy experiments a Photochemical Research Associates model LN-1000 nitrogen laser provided the ignition energy. For ignition, a 1 millijoule, 337 nm, 600 picosecond pulse from this laser was

focussed to a sub-millimeter spot in the center of the film. The precise mechanism for coupling of the optical radiation into the film is unknown; FN_3 does not exhibit an absorption at 337 nm.³ Presumably, enough energy is coupled into the system through the tail of the 420 nm absorption to initiate decomposition. Regardless of the coupling mechanism, combustion proceeds from a hot-spot located in the center of the film.

In the remainder of the experiments the films were ignited using a home-built N_2 -pumped dye laser. The N_2 pump laser was the one described above. The dye laser consisted of a quartz cuvette filled with stilbene 420 in methanol. The laser was operated broadband by forming a cavity with a 100% reflector and a 4% reflector (CaF_2 wedge). The output, as characterized with an optical multichannel analyzer, consisted of a 20 nm FWHM pulse centered at 425 nm. The pulse duration, being dependent upon the duration of the pump pulse, was nominally 600 picoseconds. This sub-millijoule pulse was also focussed to a submillimeter spot on the FN_3 film to initiate combustion. In this case, the energy couples into the film directly through the 425 nm electronic excitation of FN_3 .

Emission Spectroscopy - The spectroscopy and temporal behavior of the plume gases emissions were characterized using the apparatus depicted in Fig. 22. The spectral information was obtained using a lens to collect and focus emitted radiation onto a fiber optic bundle for delivery to a monochrometer. The 0.25 meter monochrometer was equipped with a 600 groove/mm grating. The dispersed radiation was detected on a photodiode array having 1024 elements on 25 μm centers. The electronics for this Tracor Northern Model TN-1710 multichannel analyzer operated on an internal time basis, reading and erasing the array voltage level once every 20 millisecond with a 0.5% duty cycle. Therefore, experiments must begin and end during the first 100 μs after the start of an OMA scan. Figure 23 shows (in block form) how the synchronization and OMA temporal gating functions were achieved. A ready signal (negative transition) from the OMA is applied to the synchronization circuit (Fig. 24). The voltage at the output of this circuit remains zero until the normally open fire switch is enabled. Then, the next OMA ready signal produces a pulse at the output and simultaneously disarms the circuit so that no more pulses are obtained. This single output pulse is used to fire the laser near the start of an OMA scan. The jitter between the command signal and the laser firing is still small compared to the 100 μs aperture time of the OMA. The sync pulse from the fast photodiode is then used to fire a pulse generator which produces a TTL output with

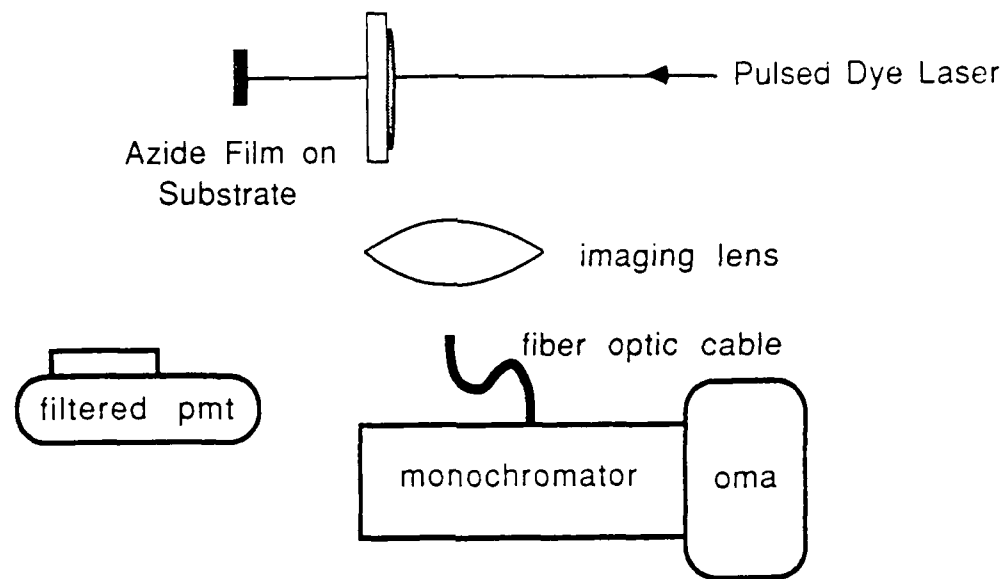


Fig. 22 Diagram of apparatus used to analyze plume emission.

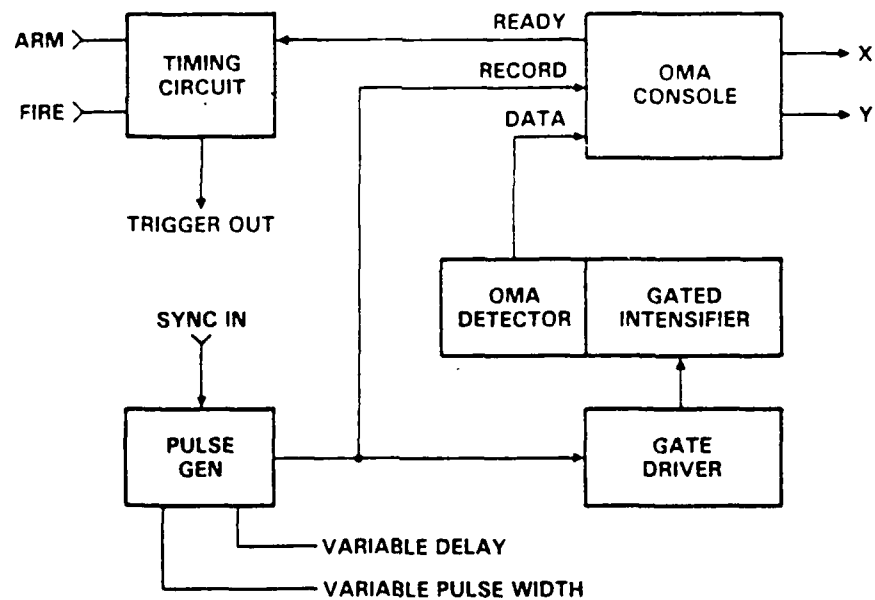


Fig. 23 Block diagram of optical detection system.

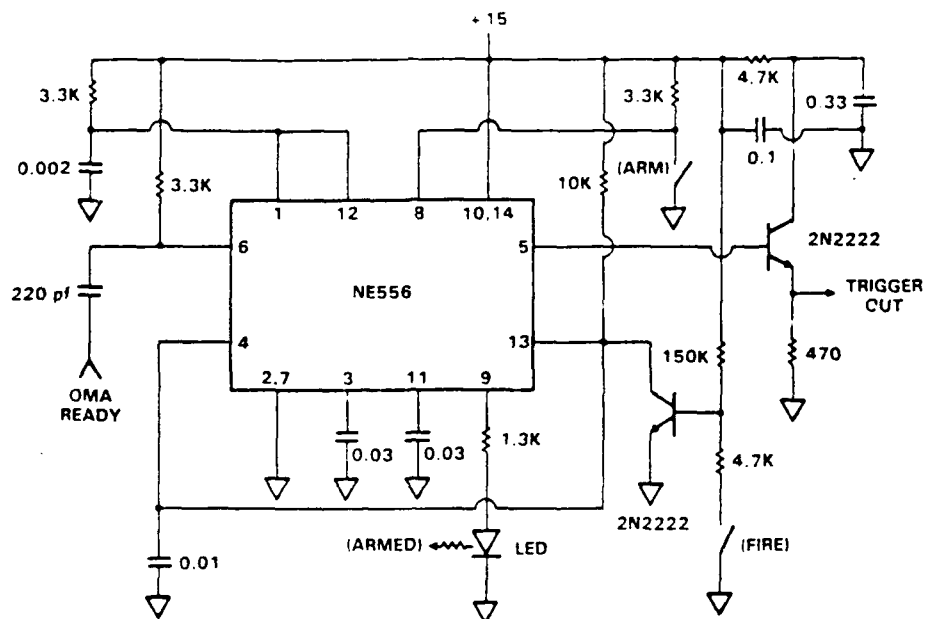


Fig. 24 Schematic diagram of synchronization circuit.

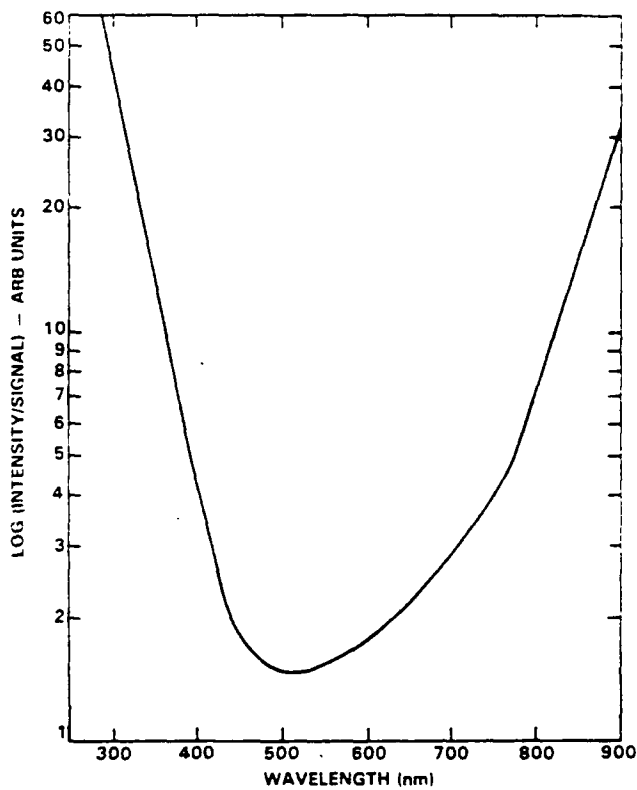
variable delay and width. In all of our experiments, the delay is set to zero. The width has been varied from 10 to 100 μ s. The pulse generator is also used to provide a signal to the OMA circuitry which causes the array output voltages to be stored in memory at the end of the sweep. Also, the pulse generator output is applied to an amplifier that drives the intensifier section of the array. This accomplishes the gating function. Accumulated delays in the photodiode, pulse generator, gate driver and intensifier result in a net 100 nanosecond delay between ignition laser output and array data acquisition. The recorded 150 nm emission spectrum is output to an X-Y chart recorder.

The OMA response function is shown in Fig. 25. This relative response-wavelength curve was measured using a blackbody source from 475- to 900-nm and a mercury lamp from 300- to 525-nm. The known relative intensities of the Hg lines¹⁸ were converted to absolute intensities by comparison to the blackbody source in the region of spectral overlap. The OMA was outfitted with 150 μm fixed slits, giving a 2 nm spectral resolution.

After identification of the spectral features, the temporal behavior of the emissions was elucidated by, as illustrated in Fig. 22, replacing the OMA system with an appropriately filtered photomultiplier tube (PMT). The narrow bandpass filters

Fig. 25

Instrument response function of OMA and monochromator.



typically had a 10 nm FWHM bandwidth: The PMT was an RCA 1P28 which was biased at 700 volt and whose output was dropped directly across the $1\text{ M}\Omega$ input impedance of a storage oscilloscope. A photographic record was kept of the signals captured on the storage oscilloscope.

Burn Velocity Measurements - The burn velocity of the films was characterized using several experimental techniques. Initially, a pulsed laser pump-delayed probe experiment to affect these measurements. As shown in Fig. 26 the experiment uses 425 nm, 600 ps output from the previously described N_2 -pumped dye laser. Approximately 5% of the laser output energy was split from the primary pulse and was sent along an optical delay line. The optical delay line consisted of a corner cube mounted on a optical rail. The primary beam was focussed to a spot size of approximately 3 mm dia. and was directed to the center of the cryogenic film. This ignition pulse was followed in time by the optically delayed probe pulse. The arrival time of the probe pulse relative to the ignition pulse was dependent upon the position of the corner cube along the optical rail. As the length of the optical rail was 5 ft, the probe pulse could be delayed by up to 10 ns. The function of the probe pulse was to measure the

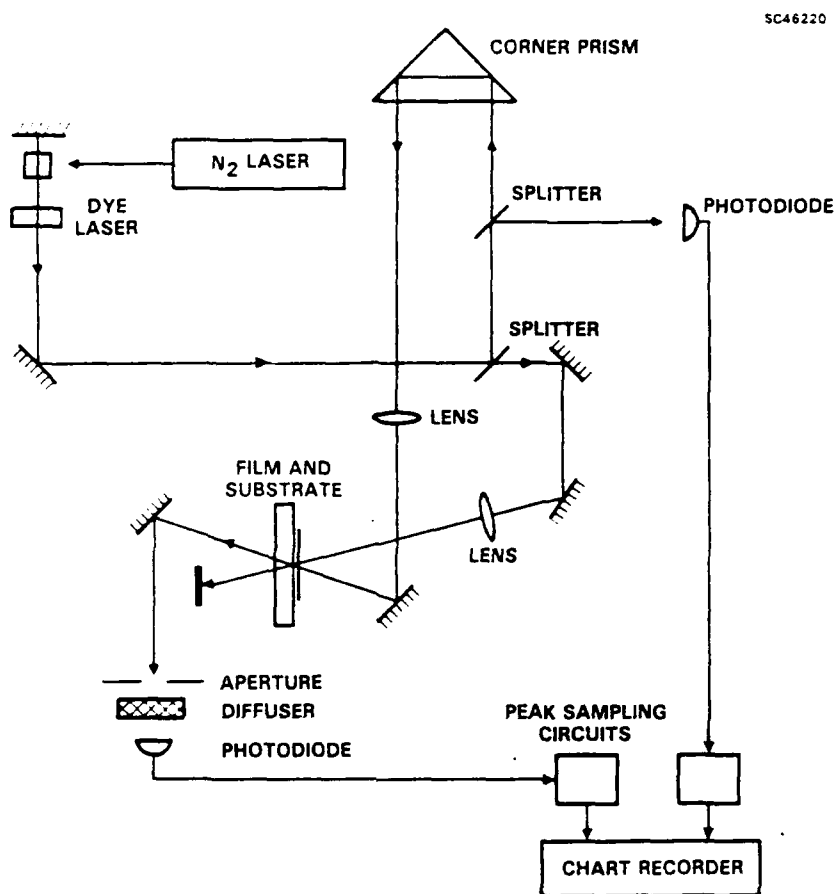


Fig. 26 Schematic diagram of apparatus used for delayed-pulse probe of film thickness.

thickness of the film (and consequently, the extent of FN_3 decomposition) subsequent to ignition. To achieve this measurement, the probe pulse, focussed to a spot size of approximately 0.5 mm dia., was passed through the direct center of the ignition spot on the film. Since the probe spot size was much smaller than the ignition pulse spot size, the possible confusing effects of sampling the film thickness over too large an area are avoided. These effects may arise if the edges of the ignition pulse irradiated spot burn at a slower rate than the center due to intensity variation. The probe pulse was then directed through an aperture which acts to reject stray light (mainly from the ignition pulse), and was then spread over the entire area of a silicon photodiode by a diffuser. The diffuser negates any subtle beam steering which may have occurred. The integrated output of the photodiode was captured by a home-built peak detecting circuit whose

output was fed to a stripchart recorder. The magnitude of the recorded signal was, then, proportional to film thickness. A second photodiode samples the intensity of the probe pulse prior to it passing through the FN_3 , providing a measurement of I_0 . In a typical experiment, the thickness of the film prior to ignition was first determined with the ignition pulse blocked. Then, with the path of the ignition pulse cleared, the dye laser was pulsed once again to initiate burning of the film. By comparing the magnitudes of photodiode outputs after ignition to those prior to ignition, the fraction of the burning film remaining at a particular time subsequent to ignition was inferred. A detonation velocity through the irradiated region of the film (normal to the substrate surface) may be inferred from this data and a knowledge of film thickness.

As will be illustrated in the discussion of the Kinetics Measurements section, the undesirable attribute of this technique was the pulsed nature of the probe pulse. All of the information on the progress of the combustion process was contained in this pulse, and it only sampled events over a 600 ps window. A continuous probe beam was, consequently, much more desirable. Thus, the burn velocity measurement technique, illustrated in Fig. 27, was developed. This apparatus was used to measure the burn velocity of fluorine azide along the surface of the substrate in the following fashion. The previously described 425 nm pulsed dye laser was focussed to a 0.5 mm dia. spot on one edge of the cryogenic film. A cw HeNe laser was focussed to approximately a 0.5 mm dia. spot which was located 3 mm from the ignition spot. Relative positioning of the spots was achieved by placing a ruled target on the substrate during system alignment. The transmitted HeNe beam was then passed through a 630 nm bandpass filter (to reject primarily the stray 425 nm radiation), and was then focussed to entirely fill the area of a silicon photodiode. The output of the EG&G SGD-100A PIN photodiode was amplified, and was subsequently captured with a Biomation 8100 transient digitizer. The amplifier had a gain of 10^5 , a response time of 10 ns and a 5 MHz bandwidth. The response time of the entire electronics train to scattered radiation of 600 ps duration was measured to be 150 ns. Hard copy of the signals were obtained using an X-Y chart recorder. Operationally, the experiment proceeded as follows: Initially the intensity of the HeNe laser radiation was at a relatively low level due to scattering of the beam by the polycrystalline azide film. When the ignition laser is pulsed, a second photodiode triggers the digitizer, and the radiation induces film ignition. The combustion propagates through the three millimeters which separates the ignition and probed spots, ultimately passing

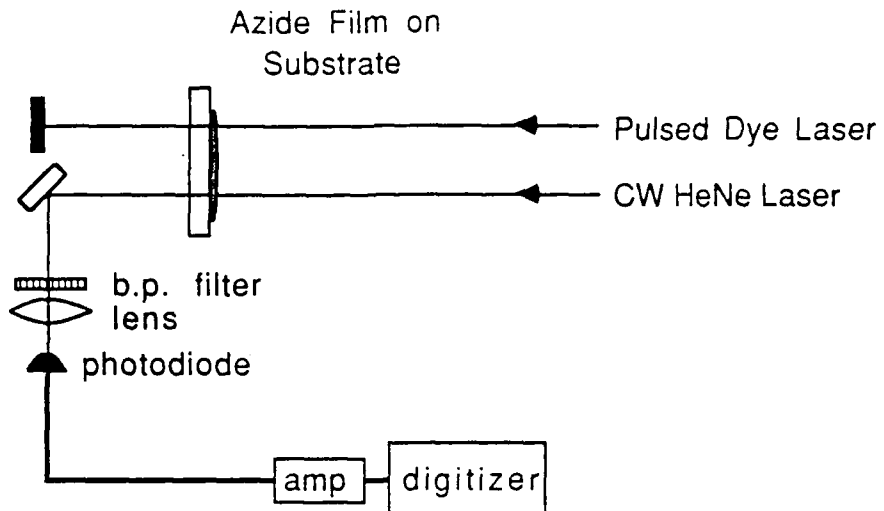


Fig. 27 Diagram of cw laser scattering apparatus for measurement of burn velocity along the substrate.

through the probed region. As the combustion of the azide in the probed region reduces the degree of scattering, the transmitted HeNe laser intensity increases. The time following ignition at which this event occurred is captured by the digitizer. Thus, from a knowledge of the beam separation distance and the arrival time of the combustion front to the probe beam, a burn velocity was calculated.

The same apparatus was used, as illustrated in Fig. 28, in a slightly different configuration to assess the dependence of ignition delay times upon ignition laser energy. In these sets of experiments, the 0.5 mm dia. spot of the focussed HeNe laser beam was directly centered within the 1.5 mm dia. spot of the focussed dye laser beam. The ignition energy was varied by placing various greyed glass neutral density filters into the path of the dye laser beam. Relative ignition energy measurements were affected by using a wedged CaF_2 optic to direct 4% of the dye laser beam into a EG&G SGD-100A PIN photodiode. The integrated unamplified output of the photodiode was recorded using a storage oscilloscope. The detection system monitoring the transmitted intensity of the HeNe laser was identical to that described above. Operationally, the experiment was performed in a fashion analogous to the burn velocity experiments. The information carried in the data from these experiments, however, the time required for the combustion wave to propagate to a distant site was removed by design. Again, the data

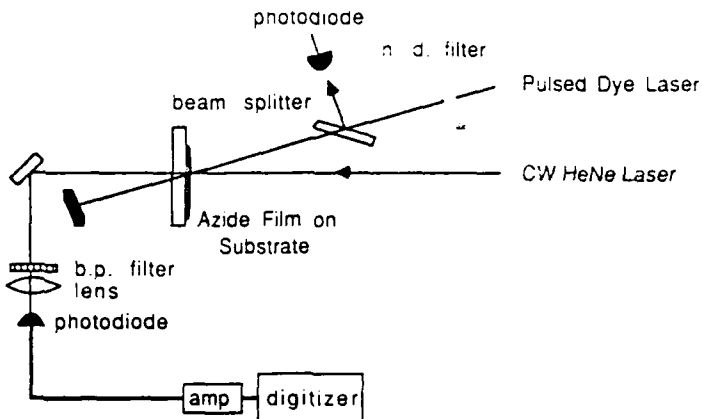


Fig. 28 Apparatus used for measurement of ignition delay time.

contain information regarding only the relationship between ignition energy and the time required for development of the combustion wave (delay time).

The above apparatus was used in yet another configuration to perform plume velocity measurements. The technique displayed in Fig. 29 is analogous to photothermal deflection, schlieren photography and shadowgraphy,¹⁹ and involves probing a line parallel to the surface of the film. In these experiments the HeNe beam was parallel to, and separated from the substrate by 2.0 ± 0.5 mm. After focussing onto a pinhole the beam was allowed to expand to fill the entire area of the previously described photodiode. After ignition, the presence of hot plume gases caused a change in the refractive index of the probed region, which consequently caused the probe beam to be lensed. Thus, many rays were defocussed off the pinhole and the light intensity sensed by the detector decreased. The remaining details of the experimental apparatus and procedure were identical to that previously described. Plume velocity was determined from knowledge of probe substrate distance and measurement of plume arrival times.

The most powerful technique used to perform FN_3 burn and plume velocity measurements was pulsed laser schlieren photography. In this technique, the refractive index change caused by the appearance of the gas plume defocusses rays of a uniform large area probe beam off of a pinhole. While similar in many respects to the line of sight deflection technique described above, schlieren differs in that the index disturbance in a plane normal to the substrate is imaged onto photographic film. As this is a pulsed probe laser based technique, variation of the timing of the ignition and probe pulse is

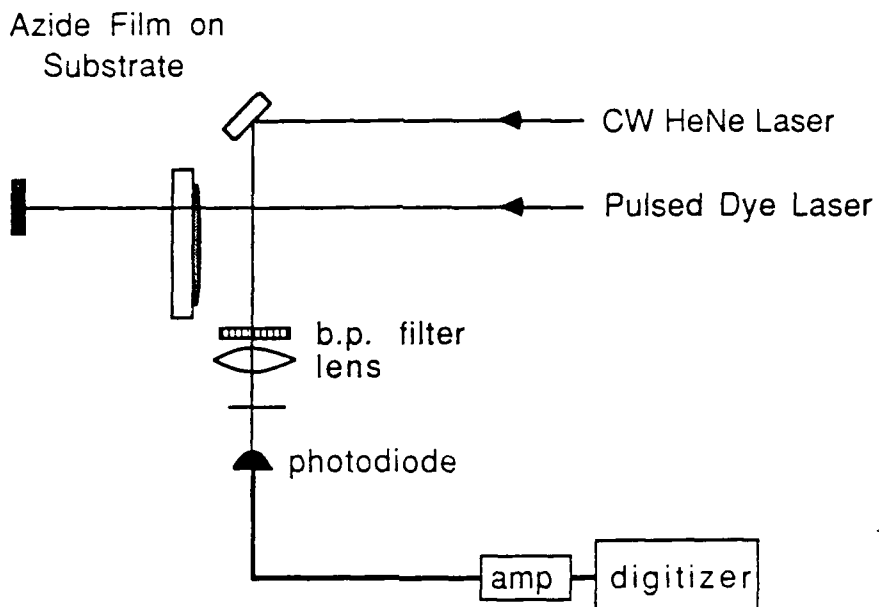


Fig. 29 Diagram of thermal lensing apparatus for plume velocity measurement.

used to elucidate the temporal evolution of the gaseous plume. The apparatus used for the measurements reported here is shown in Fig. 30. It consisted of a Lambda Physik Model EMG 101 excimer laser whose nominally 300 mJ, 14 ns output at 308 nm was used to pump a Lambda Physik Model 2002 dye laser. This laser was operated on Rhodamine 590 and provided the schlieren imaging beam. The 590 nm, 1 mm dia. output beam was spatially filtered, recollimated and, finally, expanded to a diameter of 25 mm. After passing through the combustion chamber parallel to, and above the CaF_2 substrate, the probe beam was passed through a colored glass filter which transmitted effectively blocked wavelengths shorter than 550 nm. A 150 mm focal length fused silica lens was used to focus the probe beam through a variable aperture. The lens was positioned at a distance of 2 focal lengths from the center of the azide substrate, and a standard back from a 35 mm camera was placed the same distance from the lens. The previously described 425 nm dye laser was used to ignite the azide film. A portion of the ignition beam was used to trigger a pulse generator, which in turn provided an output trigger pulse to the excimer pumped dye laser. The pulse generator provided precise control over the time between the arrival of the ignition and probe pulses. Standard 35 mm Kodak ASA 200 color film was used in the camera back. The proper exposure level a 590 nm laser pulse was found by a trial and error process: The pulse energy arriving at

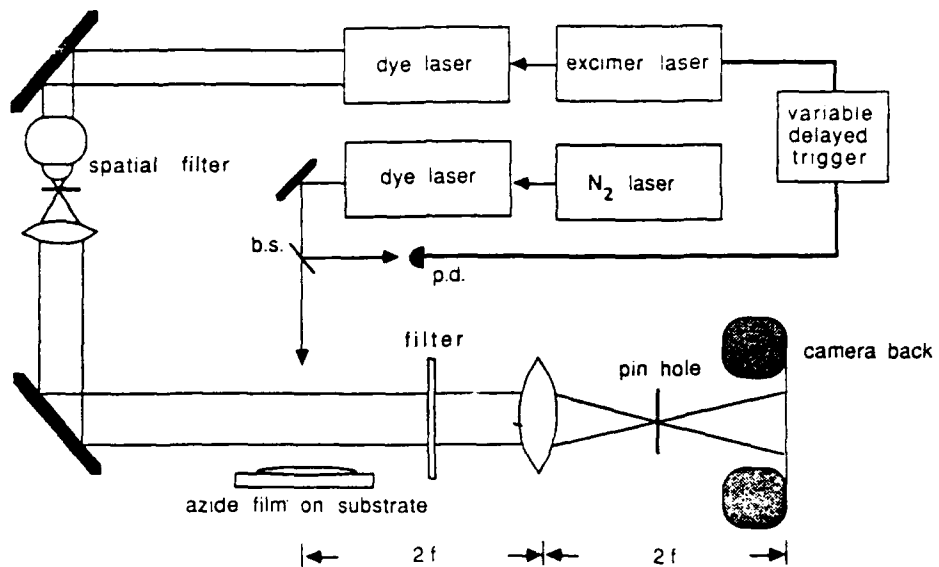


Fig. 30 Diagram of pulsed laser schlieren photography system.

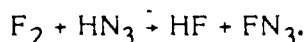
the film was less than 1 millijoule. The apparatus was operated as follows: The laboratory was completely darkened and the camera back shutter was opened. The azide was then ignited by an optical pulse from the manually triggered N_2 -pumped dye laser. Concurrently, the photodiode, sensing the ignition pulse, triggered the pulse generator, which after some preset delay period, triggered the excimer-pumped dye laser. Many of the rays present in the initially collimated probe beam, which would have been focussed through the variable aperture in the absence of additional optical elements, were defocussed as a result of the plume gas induced refractive index change, and were stopped by the variable aperture. Consequently, the photographic film was exposed to the schlieren image of the plume which formed during the (delay) time between firing of the ignition and probe lasers. The camera back shutter was, subsequently, closed, the experiment was repeated at various delay times to obtain time-resolved schlieren data. Since the 35 mm film was delivered to, and developed by, a commercial laboratory, this experiment had a very low duty cycle.

3.0 EMISSION MEASUREMENTS

During the first phase of this research, the apparatus required to reproducibly generate and combust fluorine azide films was built, and the emissions produced upon combustion were characterized. The goal of the emission studies was to provide the methodology required for subsequent measurements of burn velocity, and to develop a basic understanding of the combustion mechanism. In this section the results of the emission studies are presented.

3.1 Emission Spectra

All of the emission data were obtained prior to the incorporation of an FTIR spectrometer into the apparatus. Thus, it was necessary to probe for impurity emissions by analysis of emission spectra of intentionally doped films. In order to assess the effects of known potential impurities, spectra obtained from generator cold trap purified fluorine azide films were compared to spectra obtained following ignition of films formed with cold trap bypassed fluorine azide. Recall, the function of the cold trap is removal of residual HN_3 , CO_2 and the HF by-product from the reaction;



Spectra obtained upon ignition of films containing these impurities are shown in Fig. 31. The spectra displayed in Fig. 32 were obtained under identical conditions except that the generator cold trap was operated at -95°C during the production of FN_3 . Comparison of these two figures shows that the 337-, 356- and 387-nm bands do not depend on the presence of species removed by the trap. Some of the emissions in the 435-465 nm region are, however, attenuated by use of the cold trap. There are essentially no differences in the visible region of the emission spectra. Finally, there were no detectable emissions in the 600-900 nm region of the spectrum obtained upon ignition of cold trap purified FN_3 on CaF_2 substrates. Weak bands in this region of the spectrum of the cold trap bypassed material were determined to be impurity related. From these studies it is concluded that trapable impurities in the FN_3 gas stream do not contribute to the production of the emission bands observed below 400 nm.

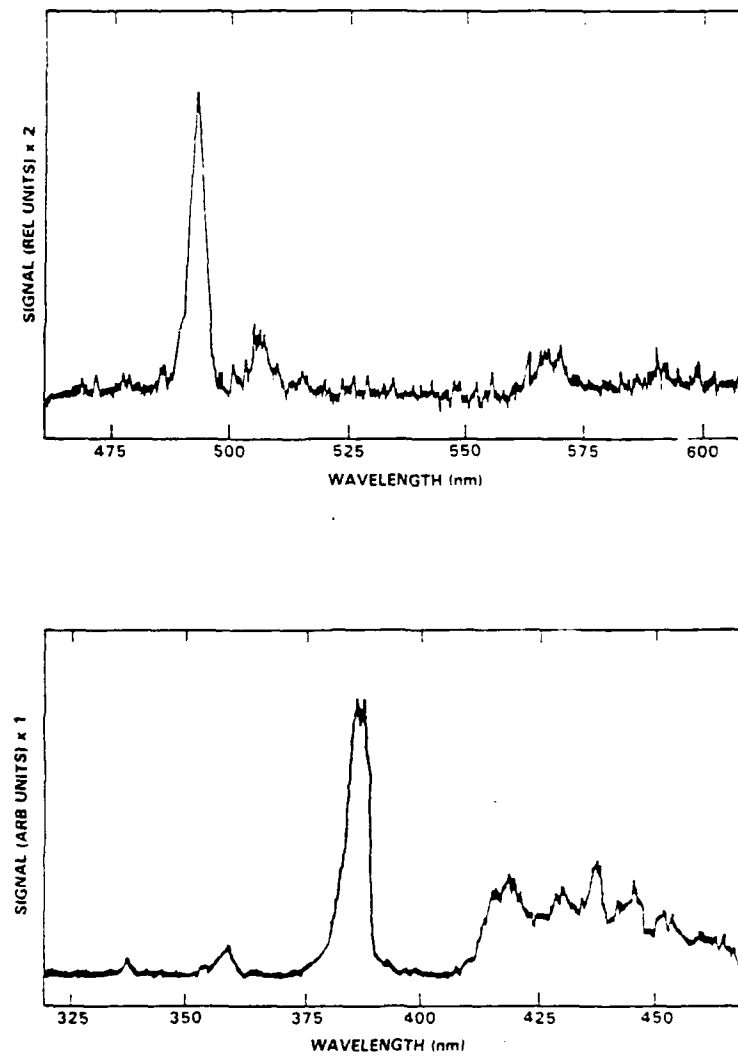


Fig. 31 Near-uv and vis emission spectra from combustion of film formed with cold trap-bypassed FN_3 on CaF_2 substrate.

The visible and near ultraviolet emission spectra obtained following ignition of FN_3 films which were formed on SiO_2 (quartz) substrates are shown in Fig. 33. Films were observed to form less readily on SiO_2 than CaF_2 . Consequently, the major difference between Figs. 32 and 33 is emission intensity. The frequencies and relative intensities of the observed emissions are essentially identical. From this limited amount of data, it is tentatively concluded that there is no chemical participation by the substrate in the combustion process. A secondary observation of 'surface pitting' of the quartz substrates after supporting the combustion of 3 to 5 films, however, indicates that

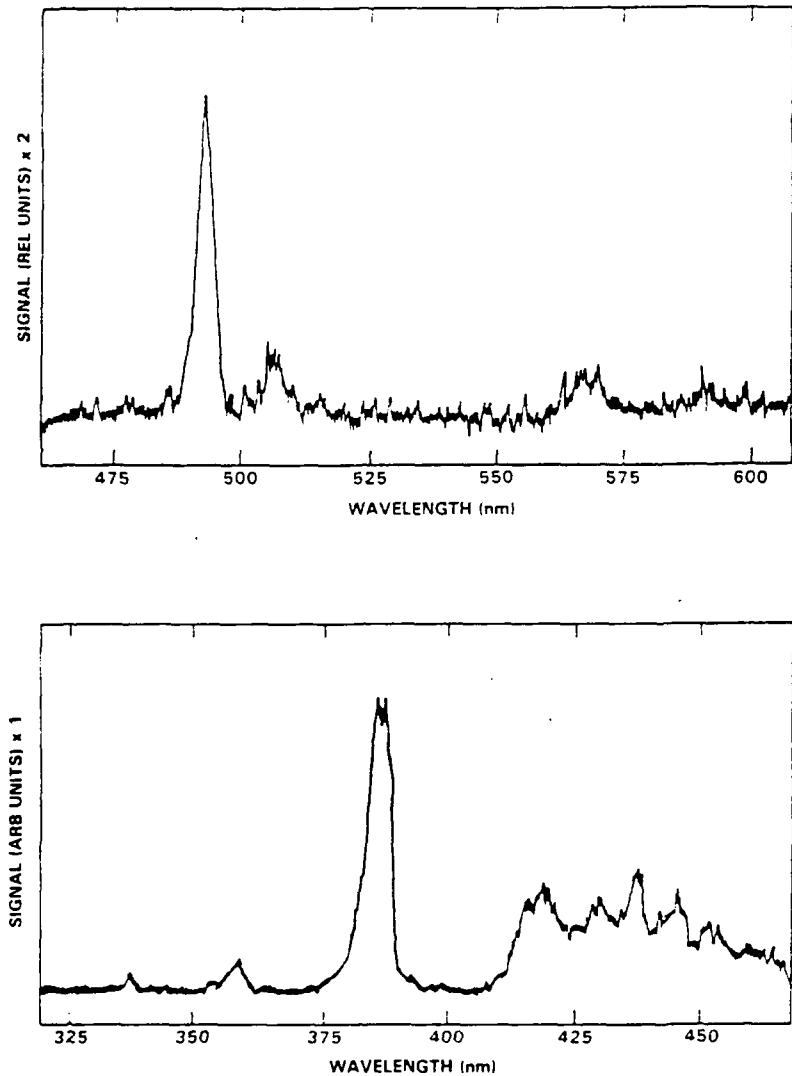


Fig. 32 Near uv and vis emission spectra from combustion of film formed with cold trap-purified FN_3 on CaF_2 substrate.

the substrates are not 'passive'. They are likely to be damaged mechanically by the forces exerted upon propulsion of the decomposition products off of the surface.

3.2 Analysis of Emitters

Ideally, the emission bands observed upon combustion of the films should be assignable to molecular fragments generated via FN_3 decomposition. On the basis of what is known of the gas phase decomposition pathways for fluorine azide,^{2,6} it might be

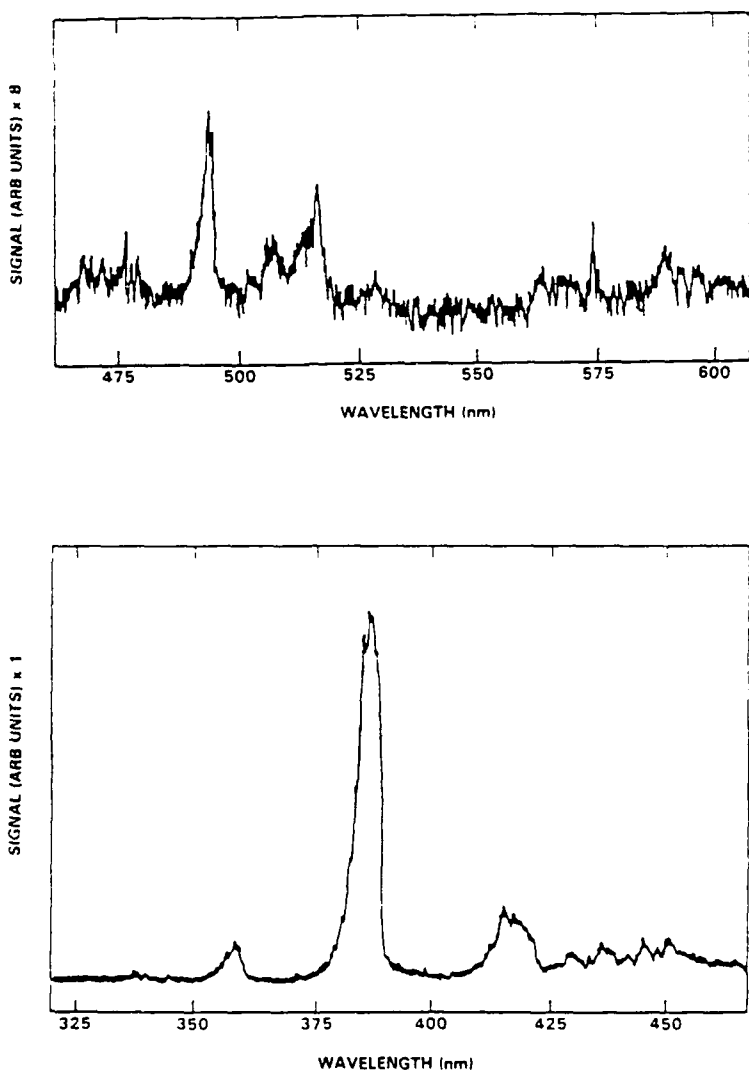
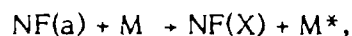


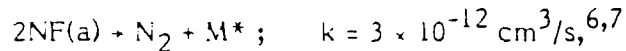
Fig. 33 Near uv and vis emission spectra from combustion of film formed with cold trap-purified FN_3 on SiO_2 substrate.

anticipated that the emission spectrum resulting upon combustion of condensed phase FN_3 would contain the bands characteristic of NF(a) and NF(b) emission. No 874 nm NF(a-X) emission was, however, observed in these experiments. This NF(a) species is exceedingly metastable, exhibiting a radiative lifetime of 5.6 s.²⁰ Thus, only two in a million NF(a) molecules can radiate within the 10 μs OMA aperture time typically used in our experiments. From realistic estimates of the NF(a) concentration (based on the amount of deposited azide), and the known sensitivity of OMA diagnostic,²¹ it can be concluded that our apparatus is insensitive to emission by the NF(a) produced in these

experiments. Further, while the NF(a) is relatively insensitive to quenching by a variety of collision partners at room temperature⁷ due to the presence of a slight barrier in the NF(a) + N₂ exit channel on the FN₃ potential energy surface,²² large concentrations of NF(a) are not expected to survive collisional quenching in the high temperature and high pressure combustion environment. In addition to,



NF(a) will be effectively removed via,



in a high density NF(a) environment. Thus, no additional effort was expended to monitor this species by enhancing our present OMA system or implementing new diagnostic procedures.

Even though the radiative lifetime of NF(b) is much shorter than that of NF(a) (20 ms²³), for a variety of reasons, it too is unlikely to be efficiently detected in these experiments. As mentioned earlier, it is not unlikely that few of these fragments can survive the high temperature collisional environment long enough to radiate. Further, NF(b) fragments which do radiate may generate an atypically weak emission spectrum. In most NF flame systems the NF(b+X) emission is easily detected as a narrow band at 528 nm. The Frank-Condon factors of this transition²⁴ tend to restrict the emission to the $\Delta v = 0$ sequence: The fragment has highly vertical potential curves. Also, in the chemiluminescent F + HN₃ flame,²⁵ NF(b) emission is characterized by low vibrational temperatures; with only the $v' = 0$ to $v'' = 0$ transitions being significant. In the combustion of an azide film, however, temperatures approaching 2000 K are expected.²⁶ Thus, emission from a variety of highly excited vibrational levels is anticipated. Weak, diffuse NF(b+X) emission may thus result for this system.

The appearance of the NF(b+X) emission from this 'hot' source can be estimated with the aid of the potential energy surfaces of NF shown in Fig. 34. While the surfaces for many NF states have been 'observed' via the ab initio calculations of Michels,²⁷ only the three lowest states ($X^3\Sigma^-$, $a^1\Delta$ and $b^1\Sigma^+$) have been experimentally observed. As the theoretical-experimental agreement was excellent for the lower states,

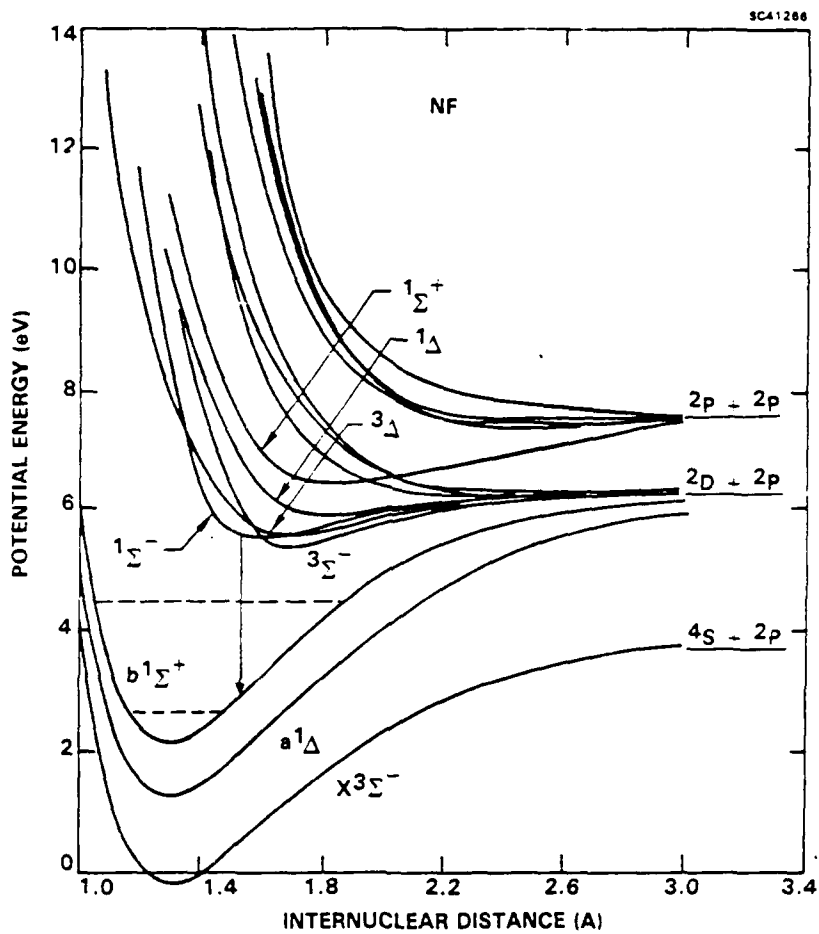


Fig. 34 Potential energy curves of NF.

it is anticipated that the calculated features of the higher lying states (Fig. 34) are without remarkable error. The results indicate that NF(b) is an excellent oscillator: As no high lying potential curves interact up to a level corresponding to 3 eV, NF(b) is capable of emission from unperturbed high lying vibrational states. From a plot of vibrational energy (or vibrational quantum number) against the emission wavelength for the NF(b+X, $\Delta v=0$) transitions (Fig. 35), it is predicted that the NF(b+X) emission band would be spread out from 528 nm to approximately 500 nm for a 1 eV mean level of excitation. Thus, the emission features between 528 and 475 in Fig. 32 can plausibly, but not definitely, be assigned to NF(b). If this assignment is correct, the absence of a discernible emission feature for the 528 nm ($v'=0 \rightarrow v''=0$) transition, implies the vibrational

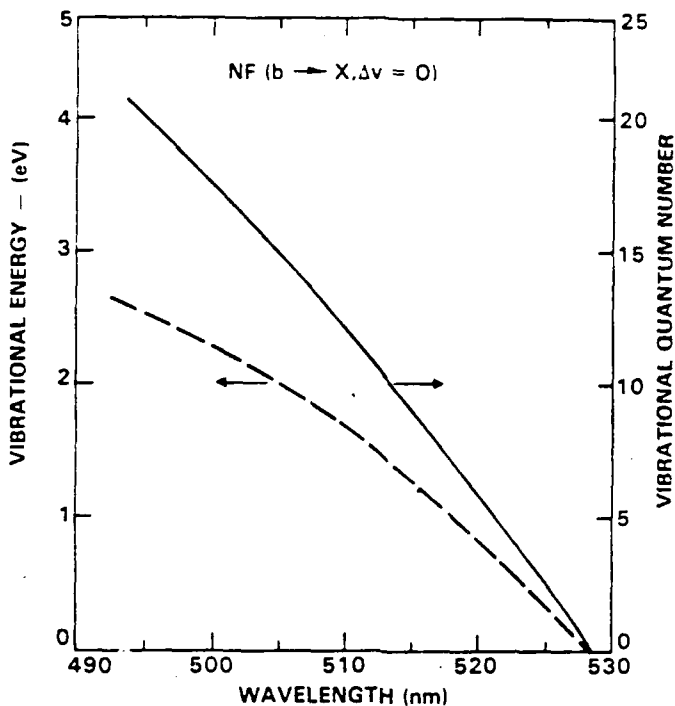


Fig. 35 Vibrational energy and quantum number of NF(b) vs wavelength of the $\Delta v = 0$ transition to NF(X).

distribution of the NF(b) fragment is strongly inverted. Inverted vibrational distributions are well known to result from highly exothermic light atom abstractions, as in the reaction of F atoms with hydrogenated species. It is stressed that this assignment is somewhat speculative, being largely based on the expected production of electronically excited NF fragments.

Comparison of the frequencies of the other visible and ultraviolet emission bands of Fig. 32 to the tabulated values¹⁰ for other probable emitters produced no clear assignments. Emission could not be assigned to atomic species. Also, there was no indication of the N₂ (B+A) emission which was observed upon detonation of PbN₃.²⁸ Comparison of the observed spectrum to that obtained from a low pressure N₂ discharge also ruled out the possibility of N₂ (C+B) emission.²⁹

Since the near-uv emission bands appear of diatomic origin, though clearly not due to N₂, F₂, NF(a) or NF(b), we were compelled to attempt to assign these features to emission by high lying states of NF. These states may be populated via energy pooling reactions of NF(a) and NF(b). Examination of Fig. 34 shows that transitions from the

more highly excited states of NF (at approximately 6 eV) to vibrationally excited levels of NF(a) and NF(b) can produce emissions at visible and near-ultraviolet wavelengths. Obase et al.³⁰ have reported observation of the NF(c+b) transitions from 440- to 570-nm upon reaction of NF₃ with metastable He in a discharge flow system. The spectrum obtained by these authors, however, does not correlate with the data in Figs. 32 and 33. The assignments of Obase are, however, disputed by other investigators³¹ who have sought the NF(c+b) transitions via laser induced fluorescence. Finally, assignment of emission to the NF(a)-NF(a) dimol, a species whose existence was postulated by analogy to the isoelectronic O₄* molecule,^{32,33} was ruled out since NF(a) dimols are expected to exhibit a structureless emission band at one-half the wavelength of the NF(a) emission (437 nm). No such feature is evident in Figs. 32 and 33.

The bands at 387-, 420- and 490-nm have been observed in a low-pressure flowtube experiment conducted as part of Rockwell International's IR&D program. In these experiments, F-atoms were reacted with H₂ and FN₃ in the presence of various catalysts. The 387 and 420 nm bands are intensified when hydrocarbons are added to the flow. The 490 nm band is best seen in the pure system. This result suggests that hydrocarbon impurities were present in the films. The 356-, 387- and 420-nm bands are assignable to the $\Delta v = -1, 0$ and 1 transitions of the CN(B+X) band system, respectively.¹⁰

A very intriguing secondary result is that while the F + HN₃ + hydrocarbon and F + H₂ + FN₃ flames each produced CN(A+X) in addition to CN(B+X) emission, only the CN(B+X) emission is observed upon combustion of the cryogenic films. The absence of detectable CN(A+X) emission in the 500-800 nm region of the spectrum implies that the mechanism of CN production upon combustion of FN₃ films is different than in the flowtube flame systems. Chemical sources of excited CN, such as the C + N₃ reaction, are likely to populate both B and A states, since they are not differentiated by spin quantum number. The selectivity of populating the CN(B) state in the film combustion experiments can be explained by considering the CN species, initially formed in the ground state, to be populated by resonant energy transfer from an excited precursor. Consequently, these data suggest the production upon film combustion of a species with at least 3.2 eV of excitation. The vibrationally excited NF(a,b) states are likely candidates.

The intensity of the 356-, 387- and 420-nm bands was greatly diminished after thorough cleaning of the combustion chamber and halting the discharge cleaning of the substrate material. Representative OMA emission spectra obtained upon ignition of much more highly purified films are displayed in Fig. 36. To gain some information about the temporal evolution of the spectra, the experiment was performed with the minimum possible OMA delay and with aperture times of 10 μ s and 50 μ s. Note that the intensity of the assigned impurity bands is weak relative to those of Figs. 32 and 33. Additionally, the 337-, 387- and 420-nm bands are evident at early times following ignition, while an intense feature centered at approximately 450 nm evolves into the emission spectrum on a much longer time scale. This emitter clearly dominates the spectrum at later times. (The 50 μ s aperture time data is plotted with vertical sensitivity which is reduced by a factor of eight relative to the 10 μ s data.)

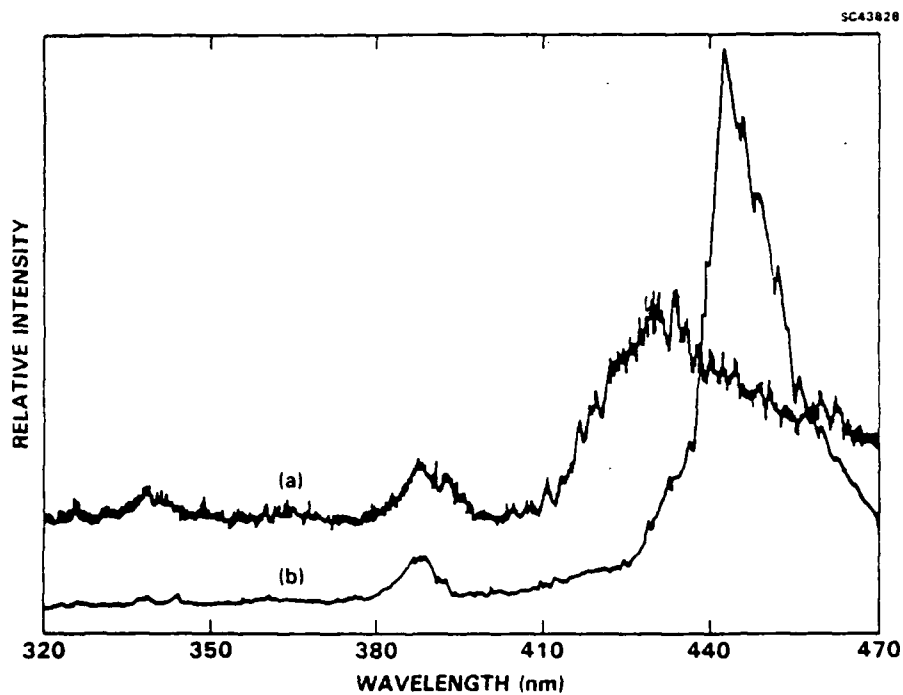


Fig. 36 Gated emission spectra of NF_3 film combustions with a 100 ns delay and aperture times of 10 μ s (a) and 50 μ s (b).

The appearance timescale of the 430-470 nm band suggested that the emitter is formed through secondary reaction chemistry occurring between nascent decomposition products. To more fully discern the temporal evolution of emissions, the intensity of the 385- and 490-nm emissions have been plotted as a function of aperture time (Fig. 37). Also plotted in Fig. 37 is the first derivative of the intensity-time curves. While the measurement is rudimentary, it is clear that both emissions originate from secondary processes.

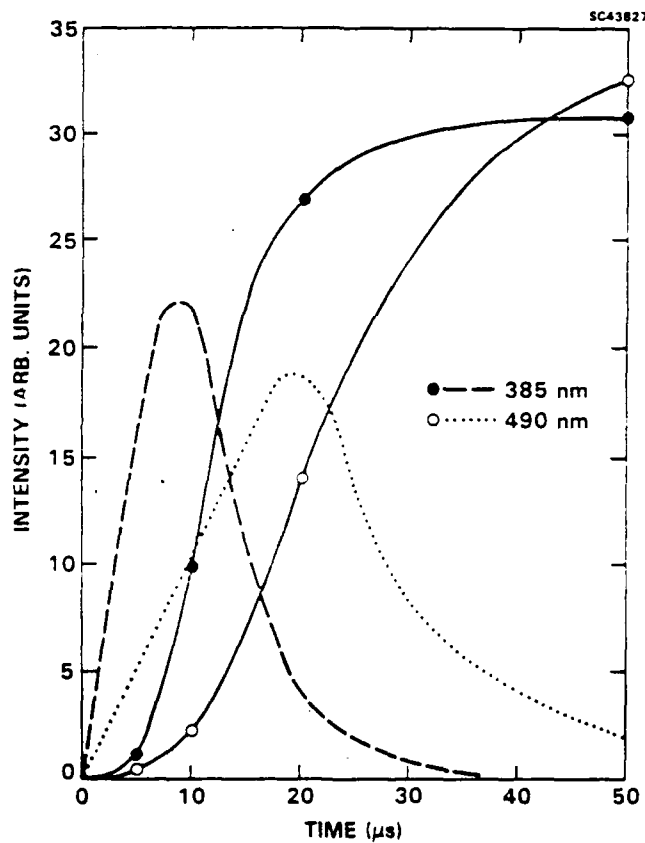
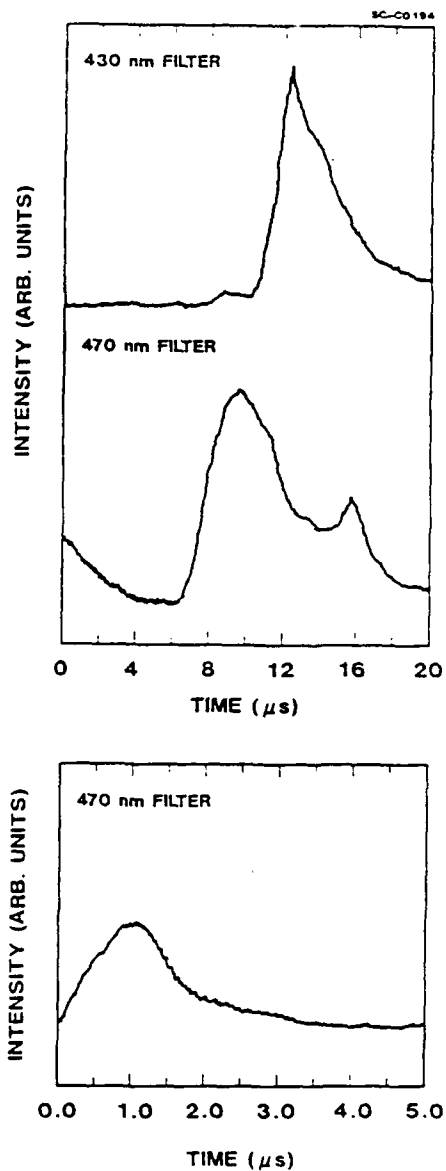


Fig. 37 Derivation of approximate time profiles from gated emission spectra.

More telling temporal information were obtained using the filtered PMT apparatus. The temporal profile on the high and low frequency side of the 430-470 nm band are displayed in Fig. 38. The temporal profile observed through a 450 nm narrow bandpass filter was nearly identical to that displayed for the 430 nm filter. From the

Fig. 38

Temporal profile of the emission feature at 430 nm and 470 nm.



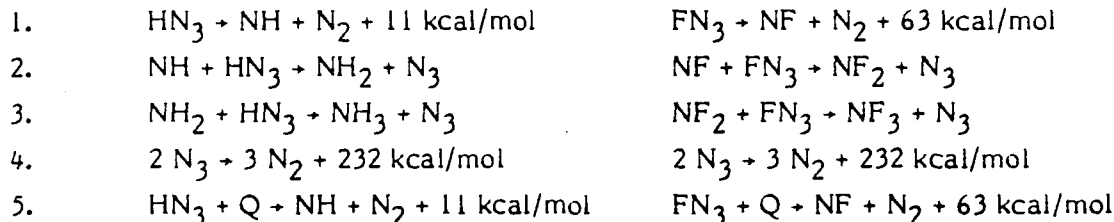
temporal profiles it is concluded that the emission feature blue shifts as it evolves into the spectrum. Although there is some 470 nm emission which peaks at approximately 1 μ s, the spectrum is dominated by the longer time scale emission.

The abrupt emission after a 6-10 μ s delay period is, indeed, remarkable for a chemical system. After careful consideration of several possible explanations of this phenomena, it was concluded that the effect must be due to the excitation of color centers in the CaF_2 combustion chamber view ports. The color centers are thermally

excited as the result of the arrival of the high temperature-high pressure plume gases to the view port. The 1 μ s emission at 470 nm is likely due to excitation of color centers in the CaF₂ substrate that supports the azide film. This effect has been observed during the detonation of PbN₃,²⁸ as well. From the time of emission onset and the substrate-view port distance a rudimentary estimate of 0.5 mm/ μ s for the plume velocity was deduced. This estimate is in good agreement with the results of the more sophisticated measurements discussed in the next section.

3.3 Decomposition Mechanism

Since no emitters which could be conclusively identified as combustion intermediates or products were observed, the results of the emission experiments provided little definitive information regarding the combustion mechanism of condensed phase FN₃. A mechanism which is consistent with many of our observations and our knowledge of azide chemistry can, nevertheless, be postulated. Although at present the details of even the gas phase combustion of FN₃ are not known, a combustion mechanism can be constructed by analogy to that of HN₃³⁴:



The ignition step (reaction 1) can be initiated either thermally or photochemically. The NX product of ignition reacts with XN₃ (X = H or F) to generate N₃ radicals (reaction 2). It is the energy released via the highly exothermic azide radical-radical recombination (reaction 4) which drives the further decomposition of XN₃ (through reaction 5).

The reaction mechanism can be further refined via comparison of the difference between the chemical physics of HN₃ and FN₃. Hydrogen azide is a stable species, having a 46 kcal/mol activation energy³⁵ for dissociation along the ground state potential energy surface: The metastable fluorine azide molecule has an activation energy of 15 kcal/mol (HM). Because of this difference, as well as the fact that the

amount of energy release in forming ground state fragments upon fluorine azide decomposition greatly exceeds that from hydrogen azide decomposition (63 vs 11 kcal/mol), FN_3 and HN_3 combustion may differ as follows. Reactions 2, 3 and 4 may be unimportant in FN_3 combustion: The exothermicity of the ignition step supplies the energy necessary for further FN_3 decomposition through reaction 5. The exothermicity of reaction 5 then supplies the energy required to decompose more fluorine azide and burning continues via an essentially thermal process. FN_3 can, thus, combust via a zero order process. The rate at which the bulk material decomposes will be equal to the rate at which the thermal wave (the moving front which separates burned from unburned material) propagates. As the material decomposes, the released energy either supports the thermal wave or is lost to the surroundings.

As written, reactions 1 and 5 imply that condensed phase fluorine azide decomposes to directly yield ground state NF and N_2 , a process which is spin forbidden. While, due to the presence of heavy neighbors in the solid lattice, efficient spin orbit coupling may facilitate the forbidden surface crossing required to form $\text{NF}(\text{X})$, reactions 1 and 5 of the combustion mechanism may represent an oversimplification of the decomposition of condensed phase FN_3 and may require modification. There is evidence for the production of nascent excited state species: Recall that the observed B state of the CN species was likely to have been populated via energy transfer from a nascent fragment. If, in fact, the condensed phase process mirrors the gas phase process, and $\text{NF}(\text{a})$ and $\text{NF}(\text{b})$ are nascent species, then the exothermicity of reactions 1 and 5 is reduced by the a-X and b-X splitting (33 kcal/mol and 55 kcal/mol, respectively). The reduced exothermicity may be insufficient to both sustain burning and overcome losses to the surroundings. Thus, the energy trapped in the a and b states must be efficiently collisionally quenched and transferred to the unburned material. $\text{NF}(\text{b})$ is known to be rapidly quenched to $\text{NF}(\text{a})$ by FN_3 . The approximately 22 kcal/mol transferred to the azide in this process exceeds the activation energy for further decomposition. As described earlier, the 33 kcal/mole carried by the $\text{NF}(\text{a})$ species are expected to be similarly disposed.

4.0 BURN VELOCITY DETERMINATION

The goal of phase two of this research was to enhance our understanding of the decomposition mechanism through measurements of the burn velocity of condensed phase fluorine azide. As originally conceived, these kinetic measurements were to be conducted by monitoring the emissions of nascent and secondary combustion products. As the system was not amenable to this type of analysis, several other probes were developed to characterize the bulk physical changes occurring upon ignition. In this section the results of measurements obtained using time-resolved scattering probes and laser schlieren photography are presented. Subsequently, the results of these measurements will be discussed within the context of detonation theory.

4.1 Time-Resolved Scattering

The apparatus depicted in Fig. 26 was used in an attempt to measure the burn velocity of the fluorine azide in the direction normal to the substrate. As illustrated in the section on experimental details, in the technique used to make this measurement, a portion of the 420 nm ignition pulse is split, sent along an optical time delay path and, subsequently, used to interrogate the ignited region of the film. An example of the type of data obtained in these experiments is displayed in Fig. 39. For this experiment, the photodiode output was fed to a storage oscilloscope, rather than the peak detecting circuit shown in Fig. 26. Only the magnitude of the oscilloscope traces at time zero is important in these experiments. (The fall rate of the signals represents the RC of the circuit and contains no information of a physical-chemical nature.) The magnitude of trace (a) at time zero represents the transmitted probe laser intensity through a clean CaF_2 substrate. After depositing a film the probe laser transmission, with the ignition beam blocked, falls to the level represented by trace (b). As illustrated in Fig. 19, the 420 nm probe is attenuated by both scattering and fluorine azide absorption, and is proportional to film thickness. Finally, trace (c) corresponds to the delayed probe transmission through the burning film 10 μs following arrival of the ignition pulse. The data in Fig. 39 indicate that, in this experiment, the level of scattering and absorption is reduced by approximately 20% at the indicated probe delay time. After relating the transmitted probe intensity to a film thickness, these data can potentially be used to calculate a burn velocity.

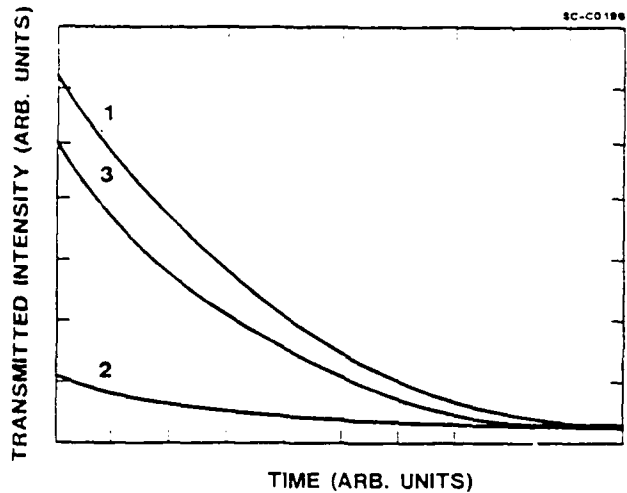


Fig. 39 Storage oscilloscope traces corresponding to laser intensity with no film (1), with azide film before ignition (2) and 10 ns after film ignition (3).

Caveats which relate to the subtle process of ignition must be presented along with the above type of burn velocity analysis. On passage through the film, absorption of the ignition pulse dissociates fluorine azide, creating a distribution of NF radicals and causing the temperature of the film to rise. If the temperature rise is sufficient to overcome the activation barrier for FN_3 dissociation, ignition of combustion will be prompt. If on the other hand, the amount of absorbed energy is sufficiently low that the threshold ignition temperature is not immediately attained, the onset of combustion will be delayed by the time required for the exothermic chemical reactions of, perhaps, the NF species to appropriately raise the temperature of the system. Thus, the change in film characteristics monitored by probe beam is a function of the intensity of the ignition beam. A second notable feature of this type of experiment, is that the combustion propagates into laser pre-heated material which contains a distribution of reactive fragments. The measured burn rate is not into virgin unburned fluorine azide. In so far as the ignition laser is responsible for the preconditioning of the material, the rate of burning into film will significantly dependent upon the ignition laser pulse intensity.

These effects are, in part, responsible for the highly non-reproducible nature of the above this type of pulse laser pump-pulsed laser probe experiments. In most

experiments no change in the probe transmission was recorded at even the maximum delay time (10 ns). One experiment indicated nearly complete removal of the film on a 1.5 ns timescale. And, yet another experiment indicated some change within 10 ns. Even for experiments conducted films on formed on the same day and ignited using the same ignition laser energy and spot size, there was a similar inconsistency in the results. A quantitative value for burn velocity could not be determined from this data. Qualitatively, the conclusion from these experiments was that changes in the film do occur on a very early time scale following irradiation, and that there is a high degree of film-to-film variability, of an unspecified nature, in these early time events. Valuably, these experiments led to the recognition of the inadequacies of the pulsed laser pump-probe technique and facilitated the development of a more powerful diagnostic.

CW Probe of Burn Velocity - It was quickly realized that elucidating the erratic temporal behavior of the burning films with a pulsed diagnostic was futile. Consequently, the cw diagnostic illustrated in Fig. 27 was implemented. In the manner described in the experimental section, this diagnostic serves to measure the burn velocity from the ignited area through unirradiated FN_3 by continuously monitoring the change in the scattering of a HeNe focussed through the film a distant site. Examples of raw burn velocity data are shown in Fig. 40. The signals, which were obtained from the burning of two separate films of different thickness, represent the intensity of the HeNe probe laser versus time. At time zero the ignition laser is fired and an emi/rfi noise spike is recorded by the detection system. There is then a brief period where the intensity of the probe laser remains constant (ca. 3 μs). During this period, a combustion wave develops and propagates to the probed spot, which in this case is separated from the ignition spot by 3 mm. The signals are then observed to change amplitude in first a negative and then a positive direction. The change in the positive direction is due to an increase in probe laser intensity caused by disappearance of the film (decrease in scattering). The magnitude of the positive portion of the signal is proportional to film thickness. The preceding negative signal, as will be more fully illustrated later, is due to a decrease in HeNe probe laser intensity resulting from negative lensing of beam by the gaseous product plume. By dividing the beam separation distance by the time at which the signal changes in a positive direction a burn rate of ca. 1 $\text{mm}/\mu\text{s}$ can be determined. A more precise value of the burn velocity will be presented after describing the effects of film thickness, and the influence of ignition delay time upon these measurements.

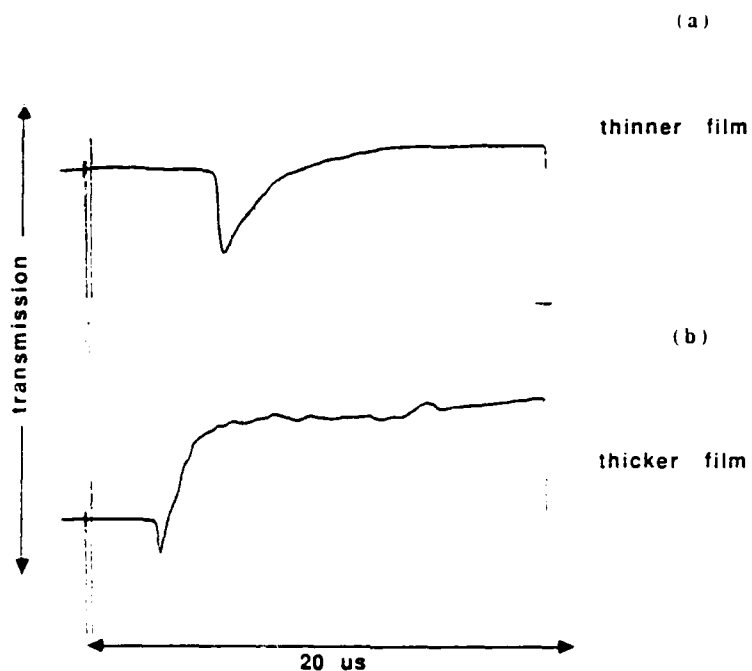


Fig. 40 Data from laser scattering measurement of burn velocity for a thin film (a) and a thicker film (b).

Effect of film thickness upon burn rate - It is apparent from Fig. 40 that there is some degree of signal-to-signal variation in the delay time between firing of the ignition laser and perturbation of the probe laser beam. It might be expected that thinner films experience losses to the substrate of a greater percentage of the released energy. Contrarily, a greater fraction of the energy released on burning a thicker film might be expected to be absorbed by neighboring molecules. If the heat loss percentage is lower, the temperature and velocity of the combustion wave propagating through the thicker film will be larger. To determine if the delay time variation observed in Fig. 40 is due to the changes in film thickness, delay time for 19 films of varying thickness was examined. The resulting delay time-film thickness data are displayed in Fig. 41. The scale of the x-axis is labelled with arbitrary units: The range of film thickness studied in these experiments varied from approximately $5 \mu\text{m}$ (the minimum thickness which would ignite) and $40 \mu\text{m}$. (Films thicker than $40 \mu\text{m}$ routinely cracked the substrate upon ignition.) The data define a line with a linear least squares slope of (-0.015 ± 0.009)

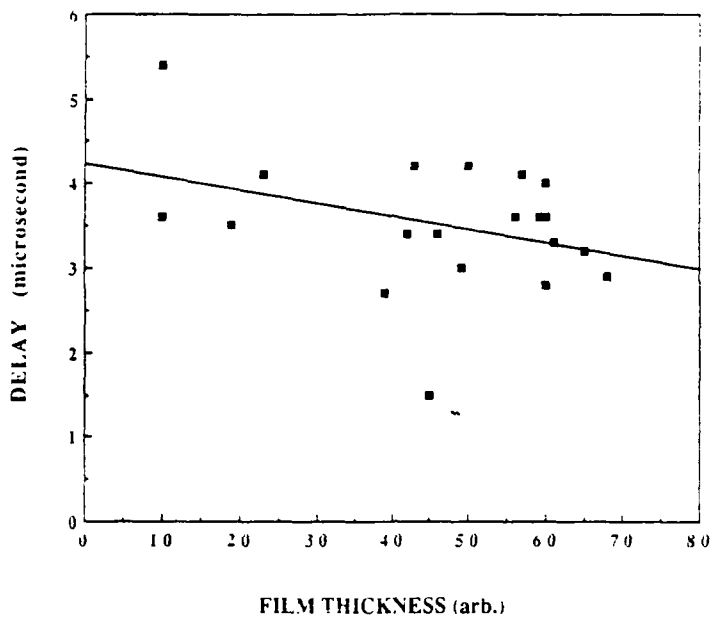


Fig. 41 Plot of delay time to scattering probe site vs FN_3 film thickness.

$\mu\text{s}/\text{arb}$ (1 sigma). Thus, while being highly scattered, the data indicate no strong dependence of delay time upon thickness. The statistically valid conclusion is that burn time is independent of film thickness over the range studied. Thus, the data of Fig. 41 give an average delay time of $(3.5 \pm 0.8) \mu\text{s}$ (1 sigma). For the 3 mm ignition-probe site separation, this corresponds to a burn rate of $(0.9 \pm 0.2) \text{ mm}/\mu\text{s}$ (1 sigma).

The rather high level of scatter in the data of Fig. 41 can arise from either true variations in the time required for the developed combustion front to propagate to the probed site, or it can result from a variation in the time required for the combustion front to actually develop. Variations in propagation time may result from the change in the concentration of some low level impurity. Potential impurities include N_2F_2 and CO_2 . The effect of these species upon the burn velocity was examined during phase 3 of this research, and will be subsequently discussed. Presently, experiments designed to determine variations in the time required for the combustion wave to develop are discussed.

Effect of laser ignition energy upon ignition delay - Several experiments were conducted to determine whether the scattered nature of our burn velocity was due to

pulse-to-pulse variations in laser ignition energy. As described earlier, ignition delay times are a function of ignition energy. The apparatus depicted in Fig. 28 was used for these measurements: Recall that ignited and probed regions of the film are the same. Thus, in this experiment variability of propagation time from the ignition region to the probed region is not an issue. As the ignited region is directly probed any measured variations are truly due to changes in ignition delay time. An example of the signals generated via this experiment are displayed in Fig. 42. Again, the signal represents probe laser intensity as a function of time. Also, as described earlier, the initial oscillation in the trace is noise generated by the ignition laser discharge and the negative portion of the trace is due to lensing of the probe laser by plume gases. For purposes of this experiment, the time delay between firing of the dye laser (beginning of noise) to the beginning of the plume gas signal is defined as the ignition delay time. A plot of ignition delay time against relative dye laser energy is shown in Fig. 43. The arbitrary x-axis represents a factor of 2 variation in ignition energy. The range spans the maximum energy obtainable from the ignition laser and the minimum energy which would ignite the films. The data, as expected, do show a correlation between delay time and ignition energy. Using the results of a linear least squares fit of the data it was estimated that a 50% variation in dye laser energy will alter the ignition delay by only 0.4 μ s. As the pulse-to-pulse variations of our ignition laser was determined to be less than 10%, the effect is too slight to account for the observed variations in the previous data. This result is vividly illustrated in Fig. 44, where the ignition delay-ignition energy data have been plotted using the same ordinate scale as that of Fig. 41: Comparison of Figs. 41 and 44 shows that approximately 0.5 μ s of the total delay is due to ignition delay, and virtually none of the scatter in the total delay measurements is due to ignition delay variation caused by ignition energy variations. The scatter in the data of Fig. 41 is, thus, likely a result of impurity induced variations in the propagation rate of the combustion front.

Finally, a rather subtle, yet important point about these experiments was noted. Inspection of Fig. 43 shows that even for ignitions with the same laser energy the delay data can be scattered by as much as 0.4 μ s. This, indeed, is a 100% variation in ignition delay time which must be attributed to something other than ignition energy. Again, it is speculated that a film impurity acts as an ignition inhibitor.

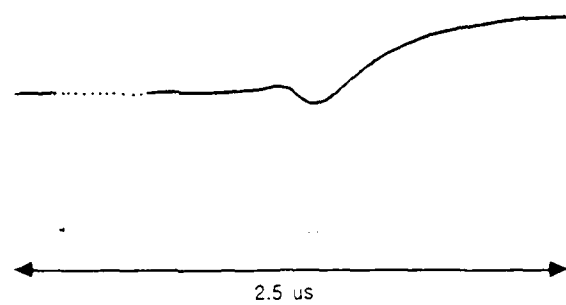


Fig. 42 Example data from measurement of ignition delay via laser scattering.

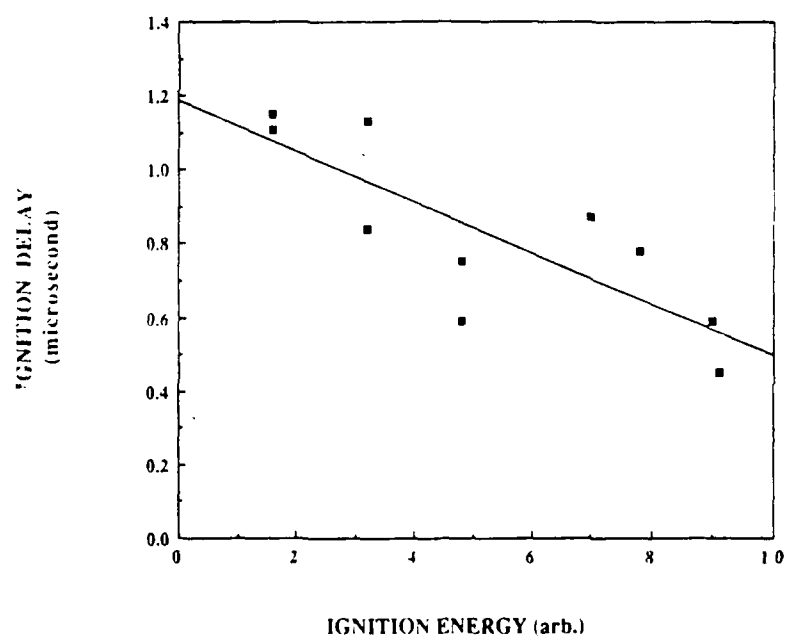


Fig. 43 Plot of ignition delay against ignition laser energy.

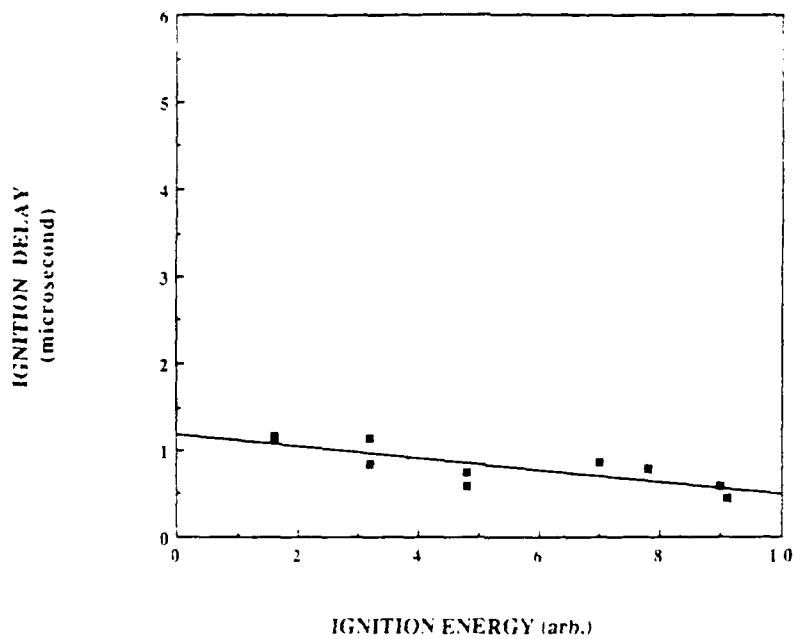


Fig. 44 Plot of ignition delay against ignition laser energy on same scale as Fig. 41.

Plume gas velocity analysis - As illustrated in the data presented in previous sections, the effect of plume gas lensing of the HeNe probe beam has been observed in all of the delayed scattering measurements. Consequently, this effect was used to estimate the velocity of the plume utilizing the apparatus shown in Fig. 29. As mentioned earlier, plume velocity can be determined from film-probe distance and the time between firing the ignition laser and the occurrence of the HeNe probe beam disturbance. An example of a plume velocity signal is shown in Fig. 45. From this signal, which represents the intensity of the HeNe beam during the 20 μ s subsequent to ignition, it is evident that a negative lens created by the gases is at a maximum at approximately 3.5 μ s. Defining the arrival time as the time for the signal to reach the half-maximum value, a plume velocity which is slightly greater than 1 mm/ μ s can be calculated. As the arrival time in line of sight measurement has been somewhat arbitrarily defined, the reported plume velocity is certainly approximate. From a series of measurements, the estimated error limits place this value at 1 ± 1 mm/ μ s.

A maximum plume velocity can be calculated by assuming that the plume is comprised of ground state NF and N₂. These species are propelled by the energy

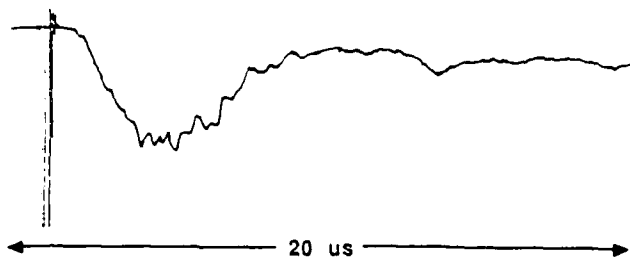


Fig. 45 Example data from plume velocity measurement via thermal lensing.

released upon FN_3 decomposition and subsequent NF^* quenching (63 kcal/mol). Assuming that one third of the released energy is partitioned into translational modes: $(63/3) \text{ kcal/mol} = 1/2 mv^2$, $v = 1.2 \text{ mm}/\mu\text{s}$. Thus, the estimated value is not dramatically different from that expected from this simple calculation. Also, as will be discussed shortly, the measured value is in close agreement with that determined from the more refined schlieren photographic technique.

4.2 Schlieren Photography

To more fully characterize and simultaneously measure the burn rate and plume velocity following ignition of FN_3 films, the time-resolved laser schlieren photographic technique was employed. Using the apparatus depicted in Fig. 30, the schlieren image of the burning film and expanding plume were recorded at various times following ignition. Figure 46 displays the schlieren image taken of the combustion environment 1.8 μs following ignition. In this figure the black block towards the bottom of the photograph is the CaF_2 substrate. The dye laser traverses the evacuated path just above the substrate, interacting with any index disturbance caused by the plume. The wrinkled triangular shaped object clearly visible on the substrate surface is the schlieren image of the plume. Within the 1.8 μs between irradiating the film with the ignition pulse and arrival of the imaging pulse, the plume has developed to a radial diameter of 7.0 mm. Within this same period gases created early on by ignition at the center of the film have been launched from the substrate to a distance of approximately 3.5 mm. Thus, three dimensionally, the plume can be represented by a cone whose height is equal to the radius of the base. The radius of the base is a minimum measure of the distance



Fig. 46 Schlieren photograph of expanding plume at 1.8 μ s following ignition.

through which the combustion wave has propagated in the azide material during the specified delay time. Therefore, a burn velocity and a plume velocity can be deduced from the schlieren image.

The schlieren image taken at various times subsequent to ignition are displayed in Fig. 47. To observe the sequential development of the plume using still photographs, of course, required the formation and ignition of several different films. Further, it was necessary to handle the FN_3 used to form each film in exactly the same way to obtain meaningful consistent results. It was particularly important that each film be formed from FN_3 that was held in the holding tank for the same amount of time. As will be subsequently illustrated, for a given delay time 'older' films were observed to have smaller plumes than films formed with FN_3 which was stored in the holding tank the minimum amount of time possible. The behavior is suspected to be due to the presence of some low level impurity. It is thus likely that that concentration of the impurity increases relative to FN_3 as the holding tank fill 'ages'.

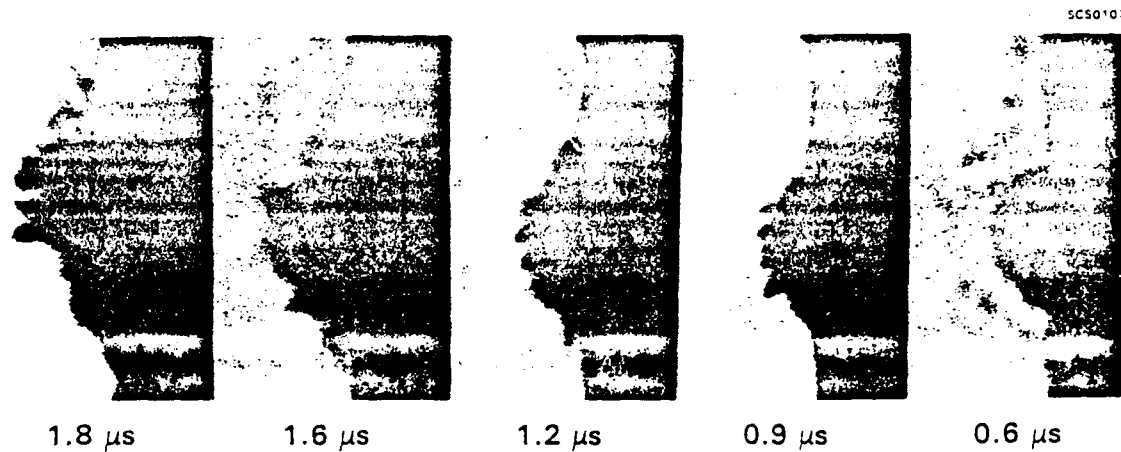


Fig. 47 Schlieren photographs of plume at various times.

The schlieren images of Fig. 47 were obtained using FN_3 held the minimum possible amount of time. A plot of the burn distance ($1/2$ the plume diameter) against delay time for eight such measurements is shown in Fig. 48. From the slope of the line formed by these data, a value of the burn velocity of $1.6 \text{ mm}/\mu\text{s}$ was determined. This value is somewhat higher than that determined via the scattering probe. As these schlieren data are of much higher quality, it is concluded that the minimum burn velocity for condensed phase FN_3 is $1.6 \pm 0.2 \text{ mm}/\mu\text{s}$ (estimated error limits).

Similarly, a plot of the plume height against delay time is shown in Fig. 49. From the slope of the curve a plume velocity of $0.4 \pm 0.2 \text{ mm}/\mu\text{s}$ (estimated error limits) is determined. This value is in agreement with the previous estimate and indicates that the combustion front moves with a higher velocity than does the reaction products.

4.3 Detonation of Condensed Phase FN_3

Many of the above observations are consistent with the decomposition of FN_3 via the process of detonation rather than deflagration. Understanding the distinctive differences in the physics of these two decomposition processes is vital for intelligently choosing methods to control FN_3 combustion. In combustion via deflagration the combustion wave front moves through the unburned material at a subsonic rate: The combustion rate is determined by chemical kinetics.^{36,37} The high pressures created by formation of product gases at the deflagration front are relieved by expansion of these

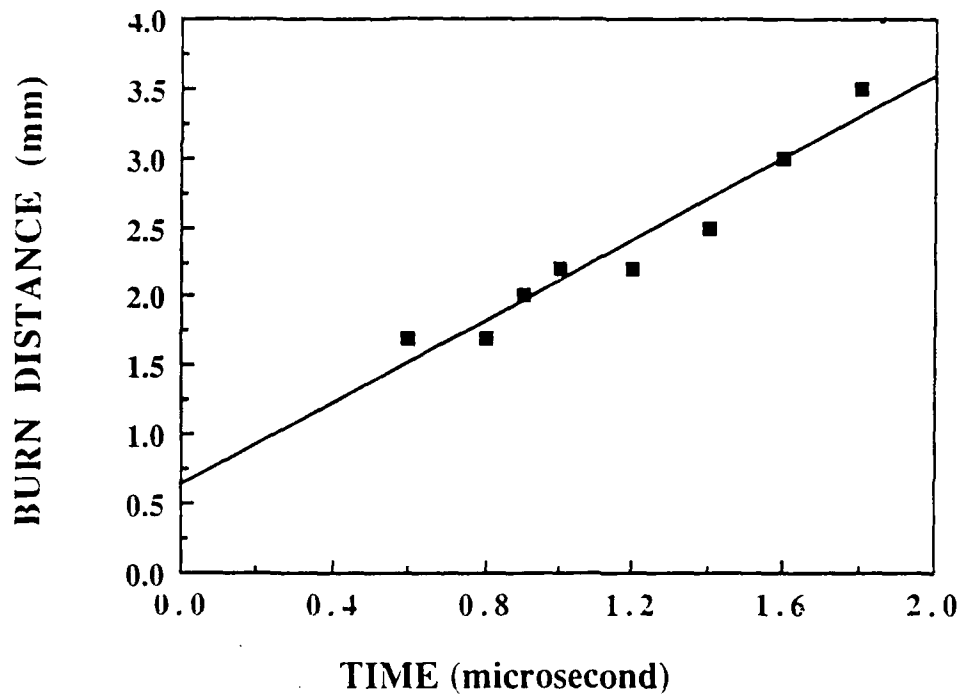


Fig. 48 Plot of schlieren measured film burn distance against time.

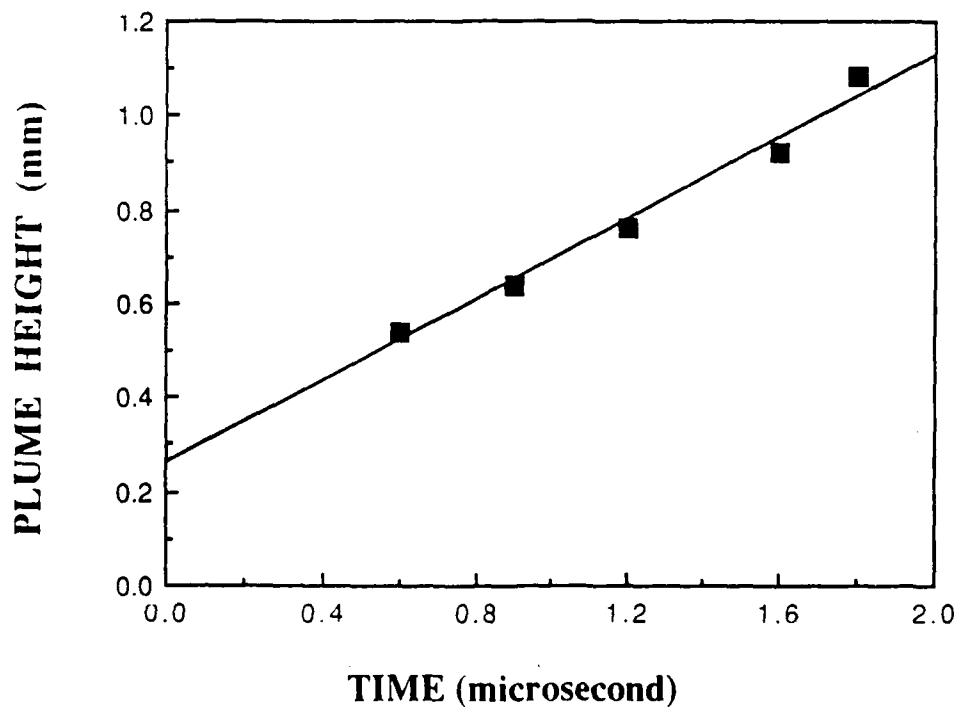


Fig. 49 Plot of schlieren measured plume height against time.

species away from the reaction zone interface. In highly energetic materials the decomposition rate can be accelerated due to the elevation in temperature which occurs if the rate of expansion is not adequate to effectively relieve the high pressures created. Concurrently, the unrelieved high pressure in the combustion zone compressively heats the unburned material into which the combustion wave propagates. This further accelerates the decomposition kinetics, hence the velocity of the deflagration and compression wave are enhanced. At some point the pressure buildup due to chemical reaction can no longer be relieved and the compressive wave is reinforced to the extent that it develops into a shock wave. At this point a detonation occurs; a supersonic shock wave, preceding a deflagration wave of equal velocity, propagates into unburned material. In this case product gases move in the direction of propagation and are compressed to exceedingly high pressures (100's of kilobar).³⁷ The material burn rate during detonation is largely controlled by hydrodynamics and thermodynamics.³⁷ However, the time between ignition and the development of a detonation wave (the run-up time or, equivalently, the run-up distance) is controllable via the chemical kinetics of the deflagration reactions.

A very important parameter in the decomposition of energetic materials is the physical width of the reaction zone. The relative large reaction zone width of a deflagration will narrow as the unrelieved pressure enhances the temperature and combustion rate. When the chemical reactions have accelerated to the rapid rates required for shock wave induced detonation, the reaction zone width can be exceedingly narrow. The magnitude of the zone width is a material dependent property, and is related to the failure diameter of the material. The failure diameter defines the minimum width of material below which detonation cannot be supported. When the width of the combustion zone and the material are comparable, the high pressures required for shock development at the deflagration front are absent due to the efficient pressure relief. This failure diameter is sub-millimeter for the detonation of azides,³⁸ while that for ammonium nitrate is tens of meters.³⁷

An important indication that condensed phase fluorine azide is detonating in these experiments comes from the observation that the burn rate is relatively independent of film thickness. It is apparent that the films were thicker than the failure diameter of FN_3 . If the failure diameter exceeded the film thickness, the burn velocity would have been found to significantly vary with the size of the ignited sample.

Accordingly, the width of the reaction zone, hence the failure diameter, is less than 25 μm . (The run-up distance, or the length of material that a deflagration propagates through before inducing shock detonation can be substantially longer than the failure diameter.)

The rate at which a detonation wave propagates is also a material dependent property. The detonation velocity, which is equal to the sum of the local speed of sound in the burned material and the particle velocity, can be estimated using the '7/32 law'. In this approximation, which is derived from an assumed equation of state for the product gases and standard thermodynamic relationships, the reaction enthalpy³⁷ is related to the detonation velocity (6) via; $Q = 7/32 D^2$. This relationship will tend to overpredict the detonation velocity for systems which do not attain equilibrium within the combustion zone. The absence of equilibrium, thus, implies that not all available energy³⁹ is used to reinforce the detonation wave and is released in afterburning. Despite this difficulty, the "7/32 law" is useful for predicting velocity ranges. It was calculated that only 10 kcal/mol is required to sustain a detonation wave with a velocity of 1.6 mm/ μs . As expected, only a small fraction of the available energy ($\Delta_f (\text{FN}_3) = 130 \text{ kcal/mol}$) contributes to propagating the detonation wave.

Typical detonation velocities for azides are between 4 and 10 mm/ μs .⁴⁰ By comparison, the measured value for FN_3 of 1.6 mm/ μs is somewhat lower than expected for an azide detonation. Nevertheless, other observations indicate that the decomposition is, indeed, via detonation. First, we again stress that the 1.6 mm/ μs value is a lower limit based on the schlieren measurements. Secondly, due to the low activation energy for FN_3 decomposition, low velocity (low energy) detonation waves may be readily sustained. Finally, features of the schlieren images are indicative of detonation.

Cartoons of the expected schlieren images for a deflagrating and a detonating film on a substrate are displayed in Fig. 50. The most notable characteristic of the schlieren image of the detonation is that the distance traversed through the film by the combustion front exceeds the distance traversed by the plume gases in the direction normal to the surface. As, again, the detonation velocity equals the sum of the local speed of sound and the particle velocity in the unburned material, as illustrated in Fig. 50, a cone-like plume is expected. If the decomposition was via deflagration the plume gases would form the more "balloonish" pattern depicted in the figure. Recall, the

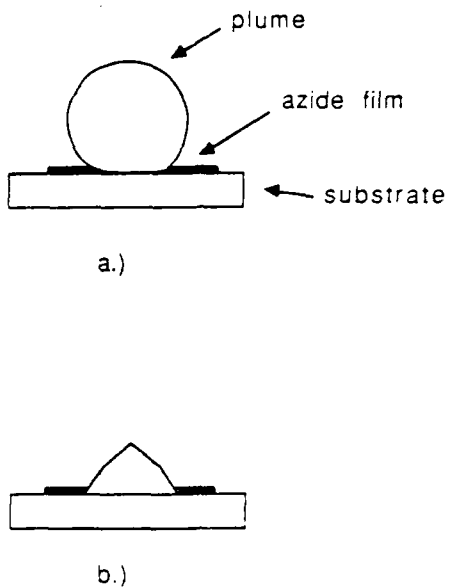


Fig. 50 Cartoon of plumes formed from film deflagration (a) and detonation (b).

schlieren images of actual burning azide films closely resemble that expected for a detonation (Figs. 46 and 48). Also, the wrinkled structure of the plume gases in Fig. 46 indicates local index of refraction variations resulting from density variations (turbulence). The turbulent mixing of the plume gases may be a result of the polycrystalline nature of the film, arising from the interaction of high pressure combustion waves in the detonation fronts of the many crystalline facets.

In summary, it appears that the combustion of condensed phase FN_3 occurs via a detonation process which can be simply represent as



where Δ_1 and Δ_2 are the enthalpy change associated with forming reactant and products, respectively, from the activated complex. As illustrated in Fig. 51, Δ_1 and Δ_2 are approximately 0.5 eV and 1.5 eV, respectively. Since the energy released upon decomposition is larger than the energy required for further decomposition, the reaction can be self-sustaining. The deflagration chemistry during the initial phases of the run-up

period may be more complex, involving quenching and reaction of NF^* . Nevertheless, the later stages of the run-up period can equally well be described by the above scheme. During detonation it is required that the released energy, Δ_2 , which is initially retained by the NF^* and N_2 fragments, be collisionally transferred to neighboring FN_3 molecules to induce further dissociation. Also, to maintain the observed value of the detonation velocity, it is required that electronic excitation of NF^* not be quenched by FN_3 . During the detonation period, quenching or reaction of NF^* subsequently occurs in the plume. This is the simplest conceivable model that is compatible with the experimental observations. Consequently, it was used to guide the search for 'stabilizers' during phase three of this research.

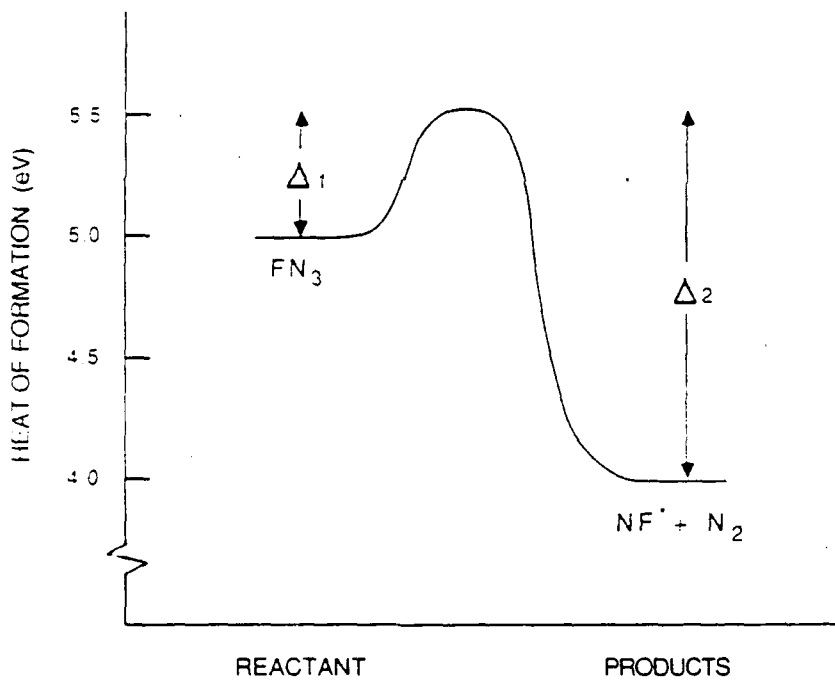


Fig. 51 Simple model for detonation of FN_3 films.

5.0 STABILIZATION STUDIES

There are potentially several methods for intelligently controlling the detonation of FN₃ which are evident in the above discussion. To forestall the deflagration-to-detonation transition, techniques to alter deflagration chemistry during the run-up period should be employed. As both the deflagration and detonation of fluorine azide is likely to be a thermal process, control over the combustion temperature is likely to be the most sensitive method of control over the decomposition rate. Control can be accomplished by incorporating additives which, for instance, endothermically decompose, or simply increase the heat capacity of the film. Since film ignition requires the input of some minimum energy (or attainment of some minimum ignition temperature), these types of additives should also effectively stabilize the films to unwanted ignitions.

During phase three of this research, the effects of additives upon the detonation velocity were examined. The research centered around additives which were already present as 'impurities' in the films as these species were suspected, from earlier experiments, to effectively alter the detonation velocity. Thus, infrared spectroscopy and mass spectrometry were employed to identify and monitor film impurities. Then, rather than rid the films of impurities, impurity levels were intentionally varied, and the effect upon the detonation velocity of fluorine azide was measured. The results of this final phase of this research are presented and discussed in the following subsections.

5.1 Infrared and Mass Spectrometric Analysis

In order to identify the impurities which were invoked in previous experiments to explain the observed variations in detonation velocity a series of experiments utilizing mass spectrometric and infrared spectroscopic analysis were conducted. Central to these experiments was the analysis of species which may adhere to the substrate after film ignition, stable impurities which are always present in the system and unstable impurities that may be formed via decomposition of FN₃.

It is conceivable that a solid state species, or a species which is reactive toward the substrate material is generated via the combustion of the FN₃ films. If, indeed, the substrate contained remnants from previous films, the velocity of subsequent

film detonations may be altered due to either reaction of FN_3 with the remnant or, perhaps, by altering the heat capacity per stored unit energy of the film. Figure 52 shows the infrared spectrum of a fluorine azide film before (a) and after (b) ignition. The with the exception of the broad weak absorption at approximately 3300 cm^{-1} , the bands in spectrum of Fig. 52 (a) have been previously assigned. The 3300 cm^{-1} is water (ice) absorption. Other weak ice absorptions are expected and can be observed at approximately 1750 cm^{-1} and 750 cm^{-1} . From the spectrum taken of the substrate after film ignition (Fig. 52 (b)), it is clear that almost all of the FN_3 is removed from the substrate and no new prominent absorption features appear. In addition to the very weak ν_3 , ν_1 and $2\nu_2$ absorptions of FN_3 , the entire base line appears to be shifted slightly and a broad low level absorption at approximately 3000 cm^{-1} is evident. This broad, very weak absorption overlaps the equally weak ice absorption in this region.

Similar experiments were conducted on intentionally contaminated substrates. Strong infrared absorption bands of a species, which form on the substrate as a result of removal of the cryogenic films by gentle heating, are easily observed. The infrared spectrum of the remnants generated by sequentially forming and heating to remove seven fluorine azide films on a KBr substrate is shown in Fig. 53. Strong absorptions at approximately 3000 -, 750 - and 500-cm^{-1} are evident. Although, these bands are presently unassigned, additional qualitative information on the nature of the absorbing species has been obtained. It is necessary for the substrate to be cooled for the absorber responsible for the 3000 cm^{-1} to be present. As shown in Fig. 54, which displays the infrared spectrum of the remnants formed on a NaCl substrate that was subsequently warmed, the 3000 cm^{-1} band is absent. The 750 cm^{-1} and (presumably) the 500 cm^{-1} bands persist.

To the naked eye, the remnant fouled substrate appears slightly clouded. Further, evidence for the reaction of the 750 cm^{-1} and 500 cm^{-1} absorbing surface deposit with FN_3 (or perhaps another impurity) has been obtained. The negative going absorptions at the appropriate frequencies in Fig. 55, indicate that the background spectrum to which the displayed spectrum is ratioed contained the absorptions of the surface deposit. Besides reaction, removal of the surface deposit via dissolution into the azide film can explain the disappearance of the low frequency absorptions. The effect of this species, as well as the 3000 cm^{-1} absorber, upon the results of the detonation

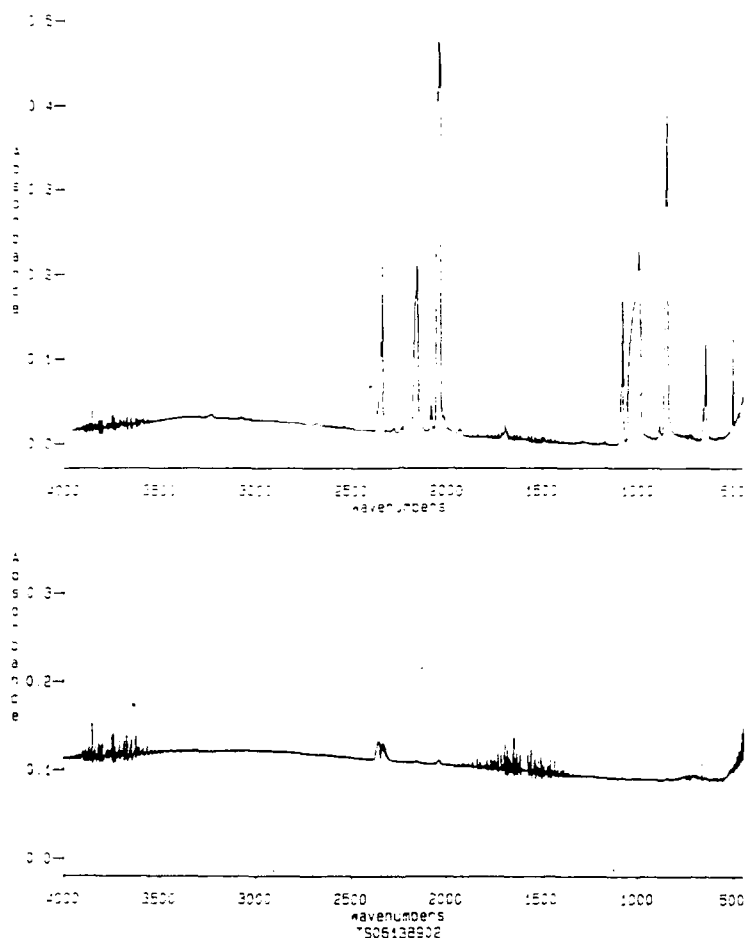


Fig. 52 FTIR spectra of azide film on an NaCl substrate before (a) and after (b) ignition.

velocity measurements is minimal since, as shown above, the rigorous combustion environment effectively cleans the substrate.

Of the many experimental parameters which had to be tightly controlled to obtain reproducible results in this research was the temperature of the HF trap of the FN_3 generator. As illustrated earlier, this trap removes impurities other than HF, with varying levels of efficiency. Consequently, a series of experiments were conducted to determine the relative levels of these impurities in the fluorine azide films. Figure 56 shows the infrared spectra of fluorine azide films formed by either first passing the azide through the -60°C cold trap or by diverting the FN_3 flow around the trap. It is

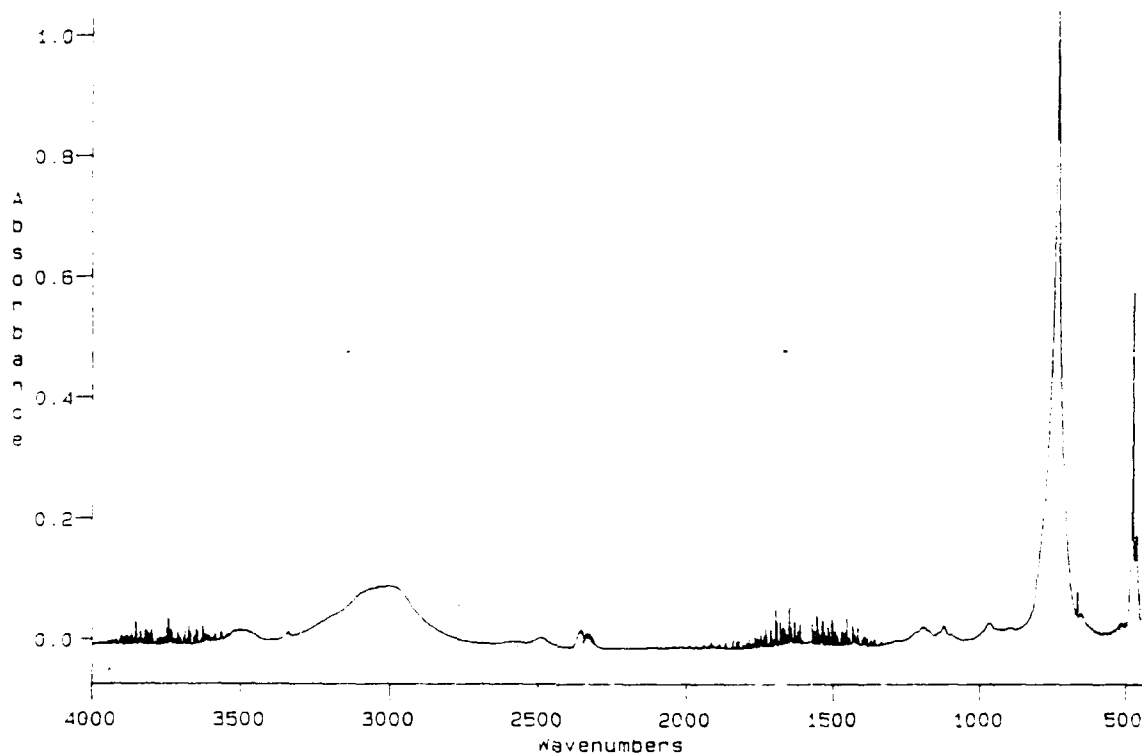


Fig. 53 FTIR spectrum of surface remnants which result from removing films from a KBr substrate by gentle heating.

immediately evident that the level of CO_2 (2344 cm^{-1} absorption) in the trap-bypassed azide film greatly exceeds the trap-purified azide film. Further, as the CO_2 has an appreciable and variable vapor pressure over the range of normal trap operating temperatures, it is likely that the level of this species was variable and non-negligible in the preceding experiments involving measurement of the detonation velocity. Day-to-day variations are highly likely. Also, comparison of the spectra in Fig. 56 shows that the 3300 cm^{-1} band of H_2O is present with or without use of the trap. This impurity was, although at a low level, persistent through out these experiments. As the cold trap should effectively remove this species, it does not appear to be a FN_3 stream impurity. Presumably, this species is desorbed from heated portions of the apparatus and subsequently condensed onto the substrate. Finally, the 995 cm^{-1} absorption, tentatively assigned to N_2F_2 , and the neighboring (overlapping) 1034 cm^{-1} absorption are present in the film formed with trap-bypassed azide; yet, absent in the film formed with trap purified azide. This may suggest that N_2F_2 is formed in the FN_3 generator and is

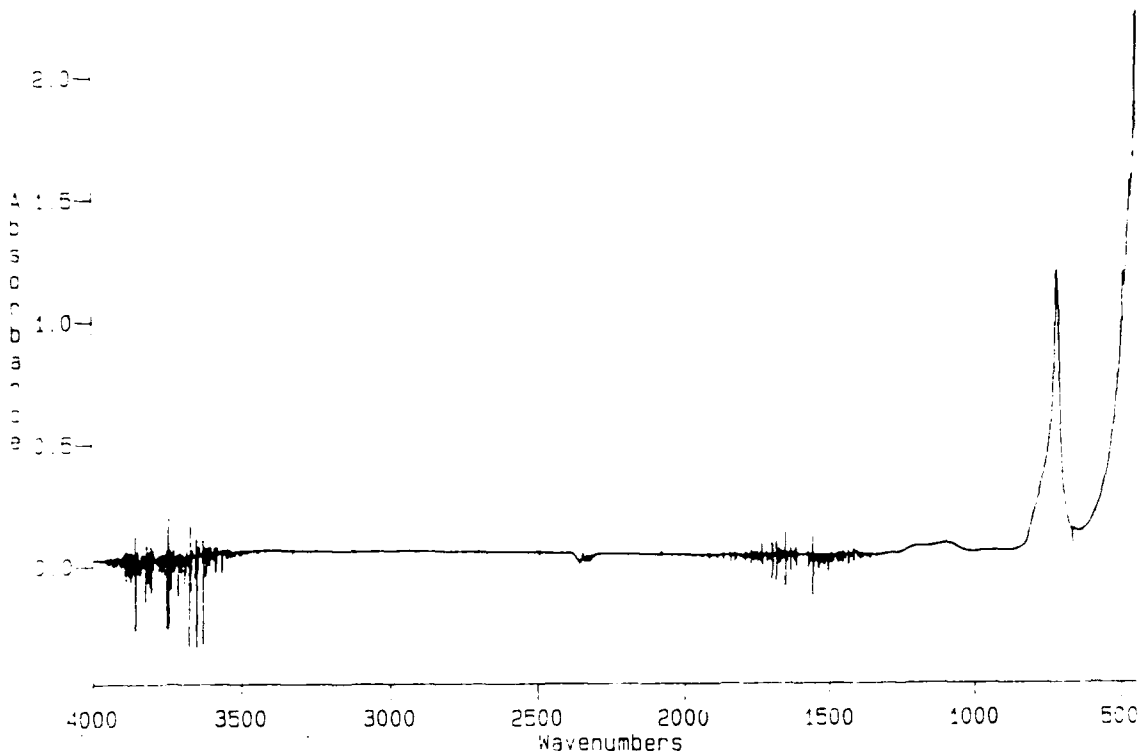


Fig. 54 FTIR spectrum of surface remnants on an NaCl substrate taken at room temperature in air.

effectively removed by the trap. As will be subsequently shown, however, these absorptions displayed phantom behavior in a variety of other experiments as well. Consequently, the above result is suspect. Whether N_2F_2 is responsible for the previously noted burn velocity variations is unclear from this experiment.

Similar experiments have shown that unreacted HN_3 is not responsible for the observed variability. In these experiments, the HN_3 generator output was intentionally undentrated and the resulting HN_3 -tainted FN_3 flow was used to form films. The infrared spectra of a films formed with this material are displayed in Fig. 57 (a) and (b). The film of spectrum (a) was formed using trap-purified azide, while that of spectrum (b) was formed from trap-bypassed azide. Comparison of these spectra shows the presence of new, yet very weak, absorptions at 1250 cm^{-1} and approximately 3200 cm^{-1} in the less pure film. As pure HN_3 films exhibit intense infrared absorptions at 3100 cm^{-1} , 2175 cm^{-1} and 1250 cm^{-1} (Fig. 58), the impurity absorptions in Fig. 57 (b) are expected.

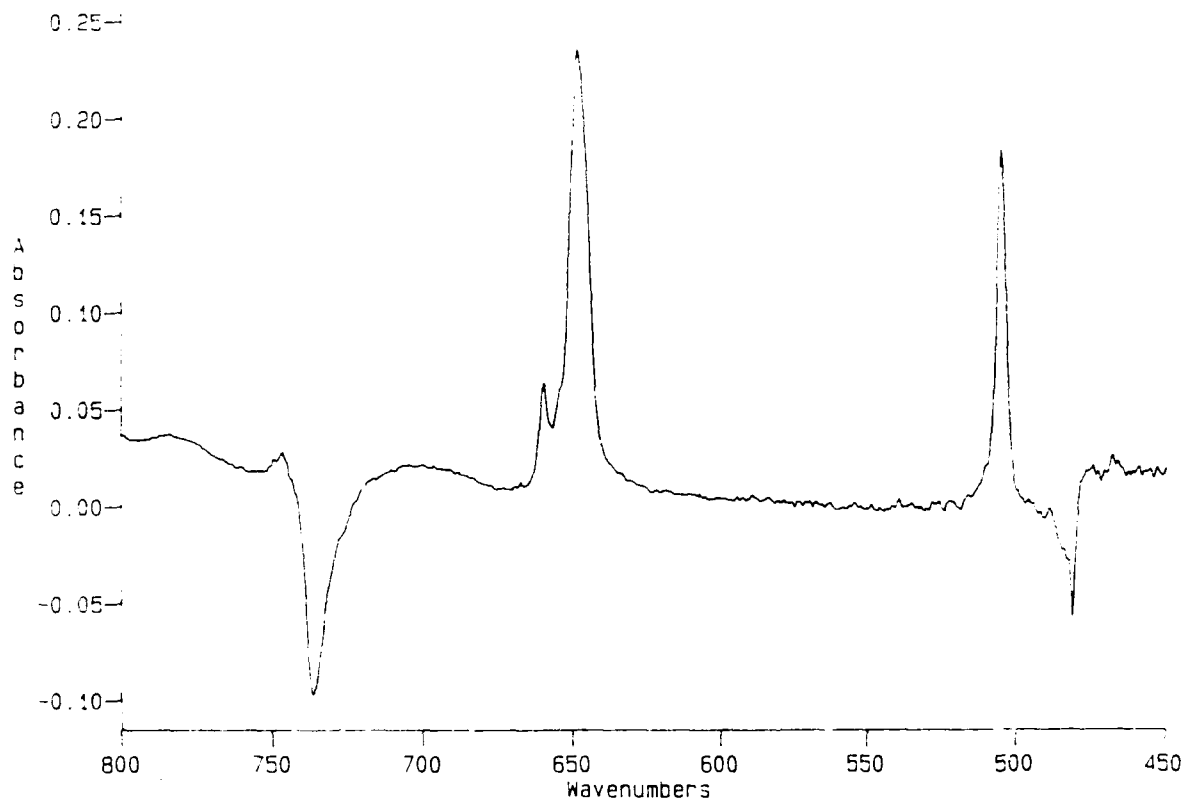


Fig. 55 FTIR spectrum showing disappearance of surface remnant upon deposition of an azide film.

Also, the 2175 cm^{-1} band of HN_3 are should overlap the $2\nu_2$ band of FN_3 . As illustrated in Fig. 59, the P branch of the $2\nu_2$ band is intensified due to this overlap. Note also that the PQR structure of the n1 band for the more highly purified film is also perturbed. This effect was unexpected and is unexplained. As will be subsequently shown, the effect illustrated in Fig. 59 can also be observed via comparison of films formed using 'fresh' azide and azide which has been aged in the holding tank for several minutes.

As repeatedly mentioned, the key parameters for obtaining consistent results from burn velocity measurements was the temperature of the FN_3 holding tank and the length of time which the material was held. It was suspected the products of FN_3 decomposition were responsible for the variation in burn velocity. An alternative explanation is that, since the amount of CO_2 relative to FN_3 increases as FN_3 thermally decomposes, carbon dioxide is the principal burn moderating impurity. Consequently, mass spectrometry experiments were coupled with IR experiments to identify the

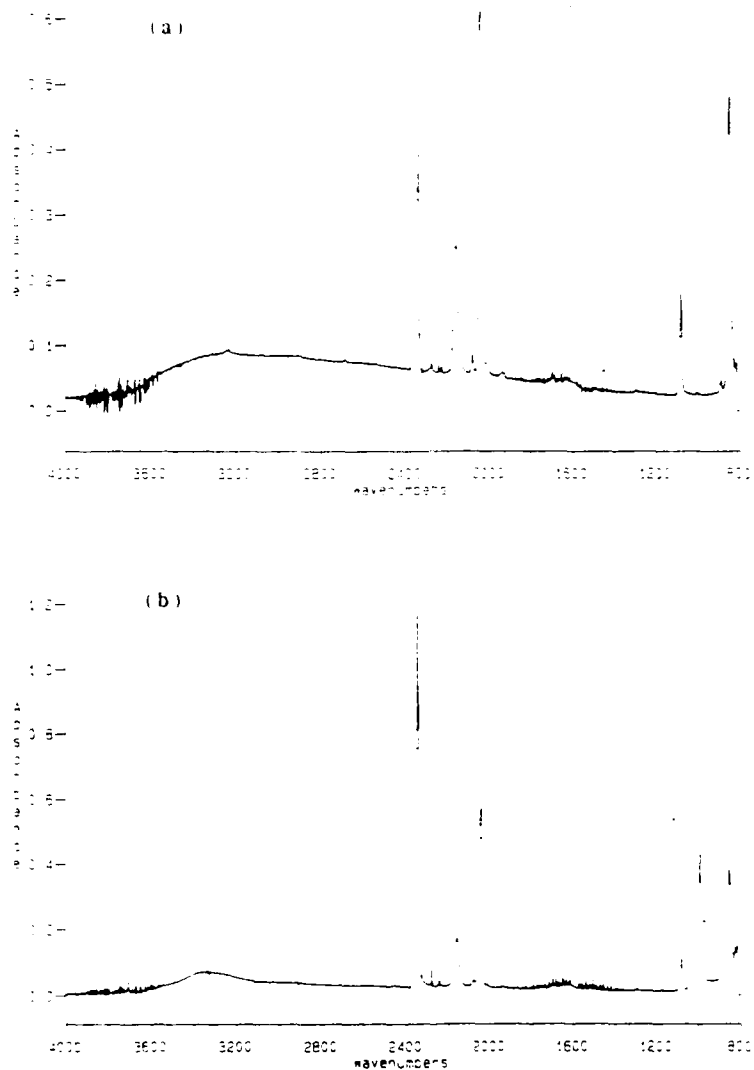


Fig. 56 Comparison of FTIR spectra of films formed from trap-purified (a) and trap-bypassed FN₃.

decomposition product impurities, determine their relative concentrations and to elucidate their relative effectiveness at burn velocity moderation.

The assigned mass spectrum of the contents of the -2°C FN₃ holding tank taken immediately after filling is shown in Fig. 60. The observed H₂O and O₂, as well as much of the CO₂ are attributable to background signal. In addition to the known product of the thermal decomposition of FN₃, N₂F₂, mass signals corresponding to NF, N₂F,

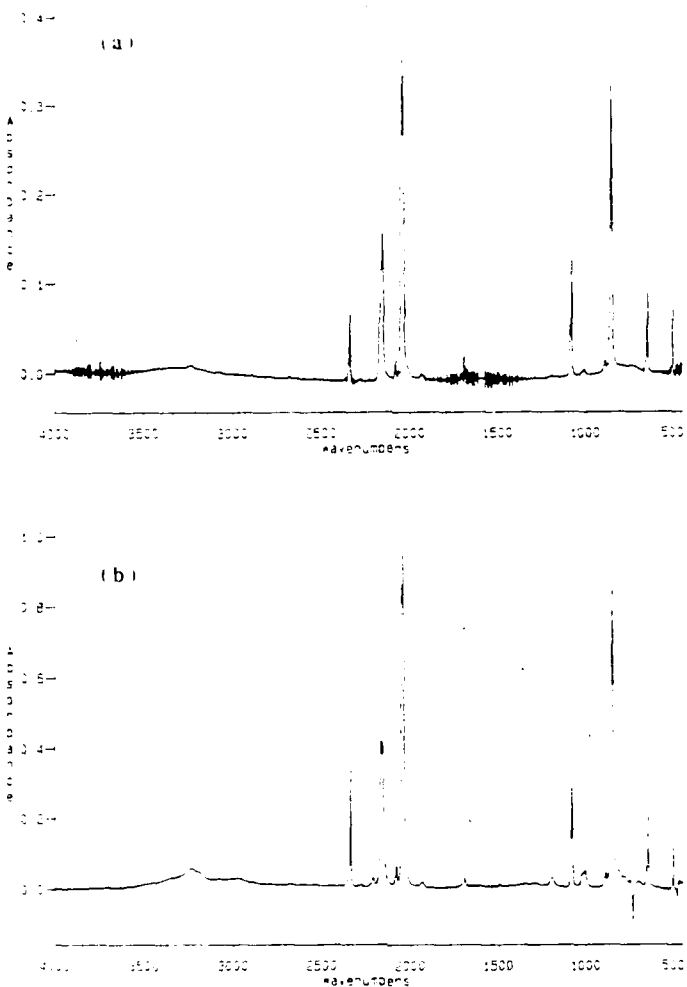


Fig. 57 Comparison of FTIR spectra of films formed from pure FN₃ (a) and HN₃ tainted FN₃ (b).

N₂F₃ and NF₂ are observed. These species are presumably formed in the mass spectrometer via decomposition of FN₃ and N₂F₂. Not shown in the figure are two other signals, the mass 71 and 85 signals, which were observed upon mass filtering to mass 120. The mass 71 peak (NF₃) was exceedingly weak, while the mass 85 (N₂F₃) peak was about 1/2 as intense as the FN₃ signal.

As anticipated, as the sample gas holding time increases, the magnitude of the FN₃ mass signal diminishes, and the ratio of the amount of CO₂ to FN₃ in the tank increases. This is illustrated in Fig. 61 (a), where the CO₂-to-FN₃ ratio is plotted

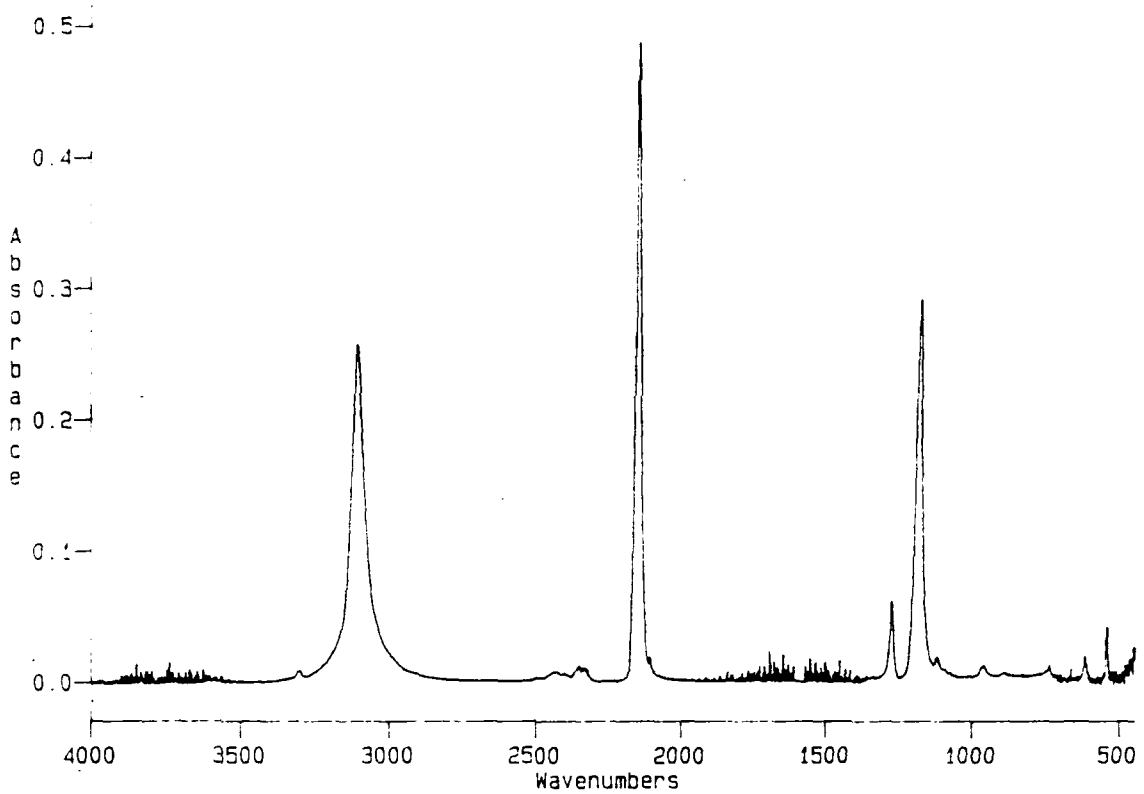


Fig. 58 FTIR spectrum of solid HN_3 .

against sample holding time. Similarly, the ratios of the FN_3 -to- N_2F_2 , FN_3 -to- NF_3 and FN_3 -to- N_2F_3 signals are plotted against the holding time in a 9°C tank. Although the data show that the relative amounts of all of these species increase relative to FN_3 , the absolute magnitude of the NF_3 signal remains minuscule.

The results of one of the infrared spectrometric experiments conducted to detect the species generated upon thermal decomposition of FN_3 are shown in Fig. 62 (a), (b) and (c). Spectrum (a) is that of a relatively pure FN_3 film. The film of spectrum (b) was formed after first passing the azide through a 1 foot coil of stainless steel which was heated to approximately 70°C. Finally, spectrum (c) was similarly obtained, except that the coil was heated to approximately 150°C. The newly appearing broad bands in spectrum (b) at 3200-, 1750- and 750-cm^{-1} are easily identified as those of water which is presumably being desorbed from the walls of the heated coil. The absorptions of N_2F_2 , FN_3 and CO_2 are present, and no other new prominent absorptions are observable. The N_2F_2 absorption at 994 cm^{-1} does, however, appear to be narrowed and more peaked.

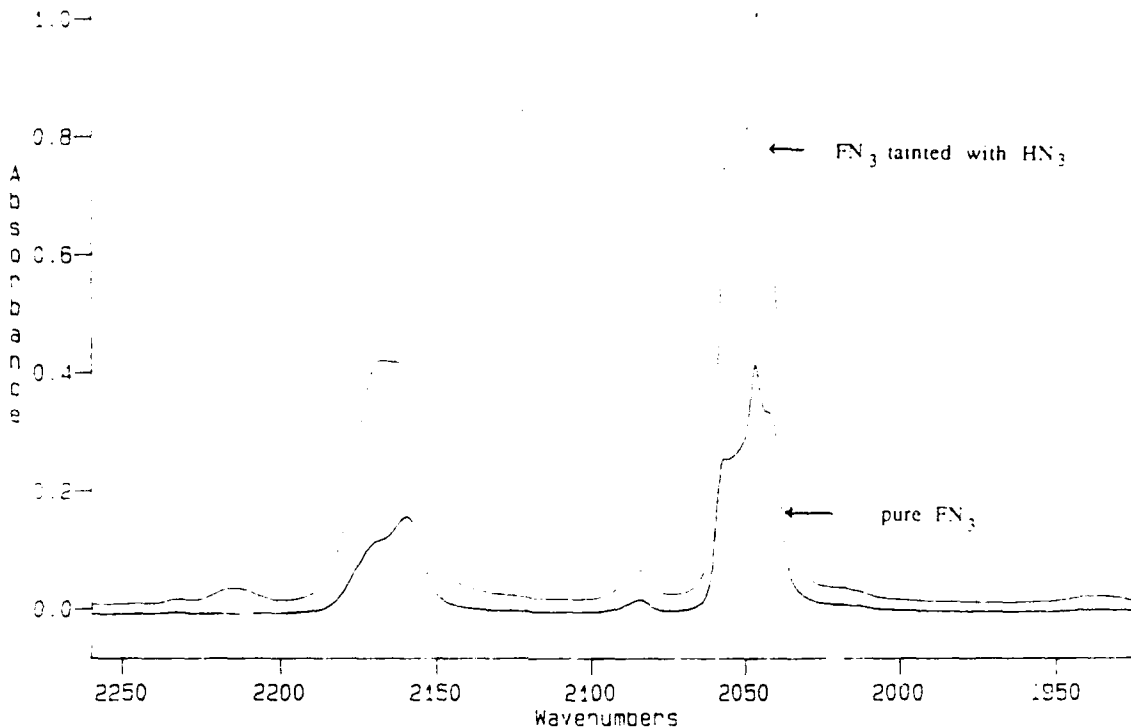


Fig. 59 Expansion of the 2100 cm⁻¹ region of the spectra displayed in Fig. 57.

This is likely due to an intensification of this band relative to the neighboring, overlapping 1034 cm⁻¹ band. Again, as N₂F₂ is a fluorine azide decomposition product, its infrared absorption is expected to be intensified in this experiment. In spectrum (c), the band of N₂F₂, and the 2344- and 667-cm⁻¹ bands of CO₂ are the only prominent features observable, other than the ice bands. The bands of FN₃ are greatly diminished. The 994 cm⁻¹ absorption is much more highly sharply peaked in this spectrum. These experiments indicate that N₂F₂ is the only decomposition product which can potentially moderate the burn rate of fluorine azide. As the expected NF₃ absorptions at 1031 cm⁻¹ and 907 cm⁻¹ were not observed, this species likely does not play a major role in the observed combustion processes.

Since N₂F₂ possibly behaved as a combustion moderator, it was desirable to determine the relative amount of this species in various films prior to ignition. Consequently, the infrared spectra of FN₃ films formed at various times after filling the holding tank were recorded. On the basis of the above mass spectrometric results, it was

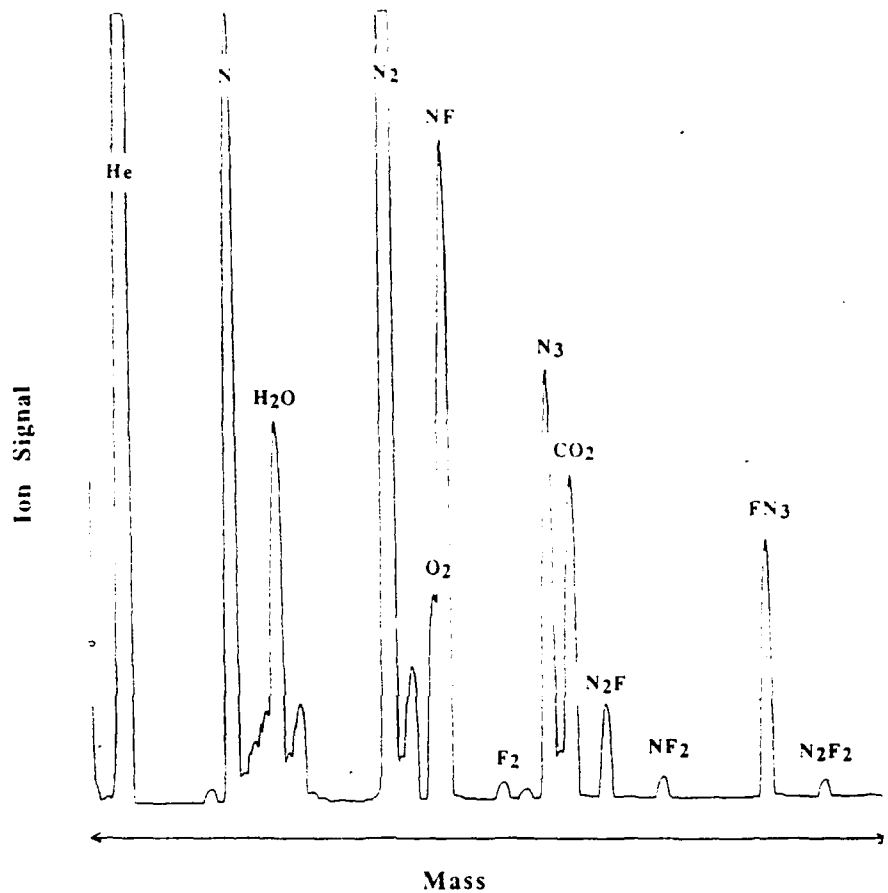
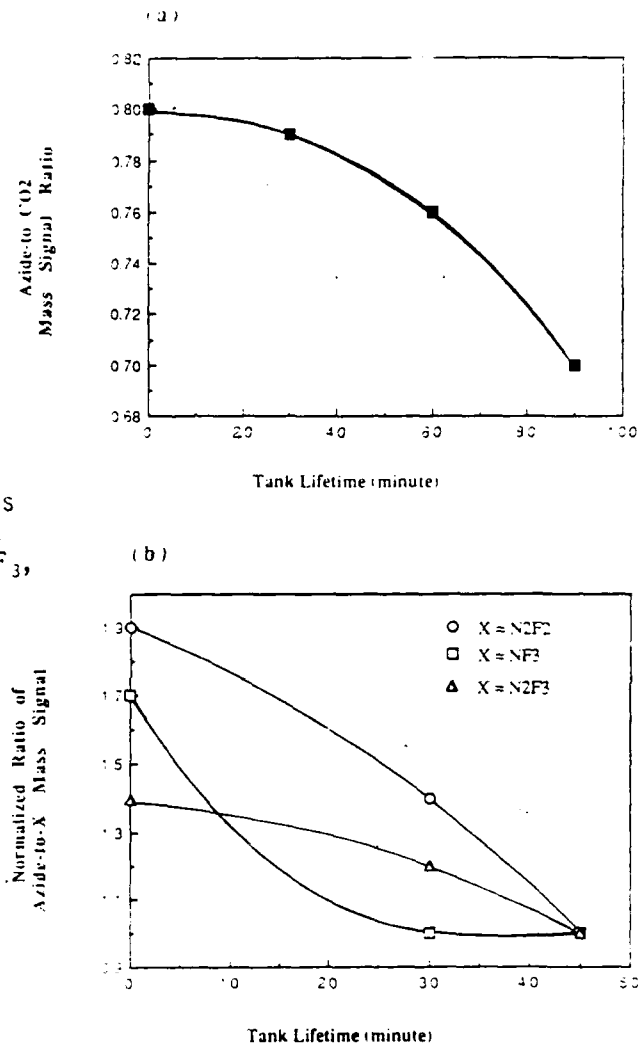


Fig. 60 Mass spectrum of holding tank gases tank immediately filling with output of FN₃ generator.

expected that the amounts of N₂F₂ in the films would increase as a function of time in the holding tank. As shown in Figs. 63 (a), (b) and (c), this expectation was not realized. The spectra in Fig. 63 were obtained for films formed from the same fill of FN₃ in the holding tank. Spectrum (a) is of the film formed with 'fresh' FN₃. The film of spectrum (b) was formed 23 minutes later, and the spectrum (c) is of a film formed 38 minutes after the first. Note that while complex overlapping band system in the 1000 cm⁻¹ region of the spectrum initially evolves and begins to resolve into three bands (see Fig. 64 for a blown up view) as the holding tank fill ages, the 'oldest' film (spectrum (c)) shows a near complete diminishment of the band in the 1000 cm⁻¹ region of the spectrum. The 'phantom' behavior of the 1000 cm⁻¹ is puzzling, indeed. As illustrated in the previously describe mass spectrometric studies, the level of N₂F₂ in the FN₃ gas

Fig. 61

Ratios of the mass signals of impurities to FN_3 for gases in the holding tank at various times: CO_2/FN_3 (a); N_2F_2 , NF_3 , and $\text{N}_2\text{F}_4/\text{FN}_3$ (b).



sample increases with the time in the holding tank. The contrary IR results may be due to reaction of N_2F_2 with an undetected substrate impurity. In several other similar experiments, this sort of 'phantom' behavior was repeatedly observed.

An observation which was equally consistent from experiment-to-experiment is illustrated in Fig. 65. This figure displays a blown up view of the high frequency bands of the solid FN_3 films formed from the same holding tank fill at the previously mentioned times. The evolution of the 2050 cm^{-1} band from a PQR system to the pattern shown in Fig. 65 was a completely reproducible observation. The displayed evolution of the 2160 cm^{-1} band was similarly reproducible. These experiments have illustrated that

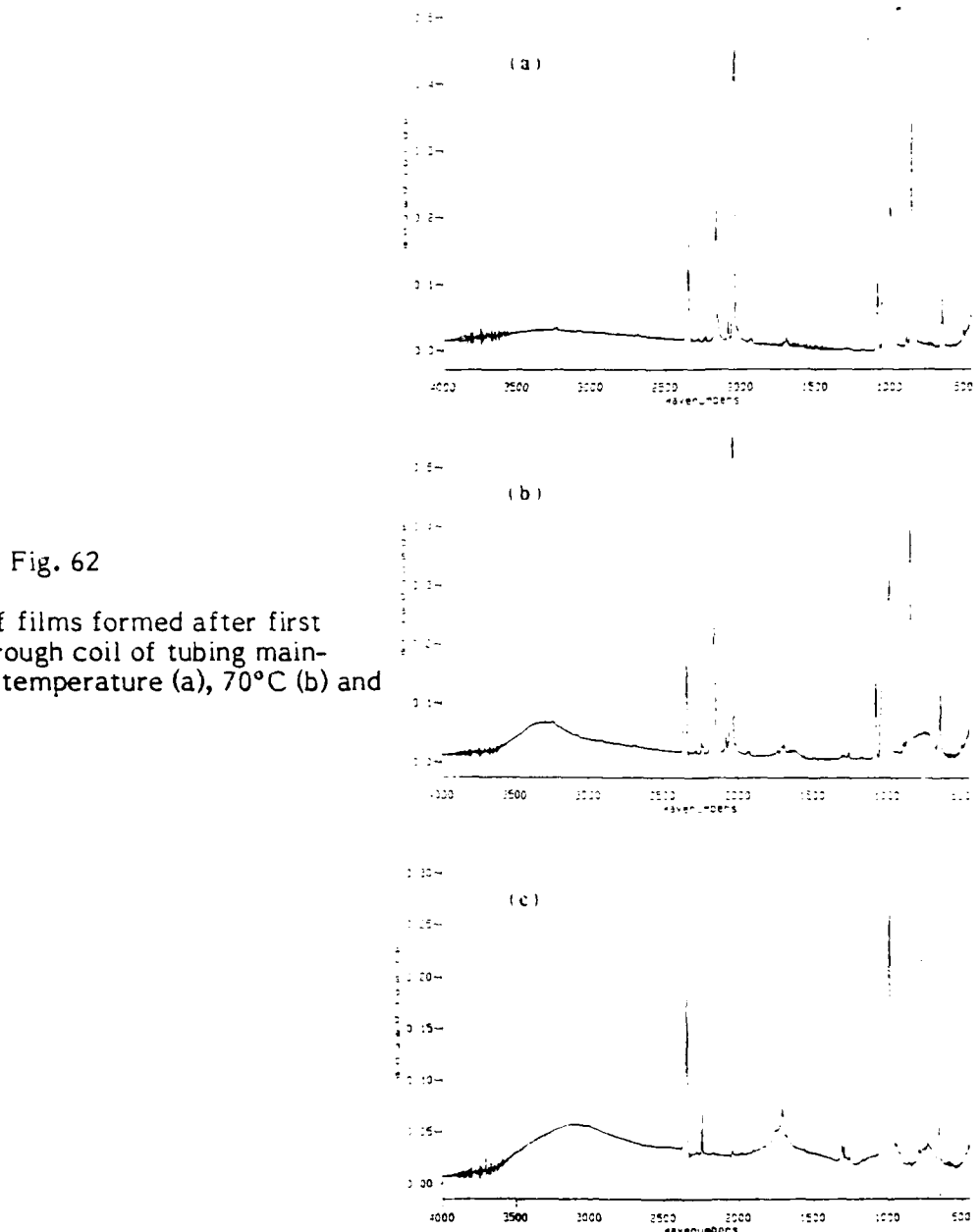


Fig. 62

FTIR spectra of films formed after first passing FN_3 through coil of tubing maintained at room temperature (a), 70°C (b) and 150°C (c).

there is another infrared absorbing species which interferes with the high frequency FN_3 absorptions. This species, though presently unidentified, is formed at low enough levels in the holding tank that its influence on the combustion of FN_3 is negligible for films formed from 'fresh' FN_3 .

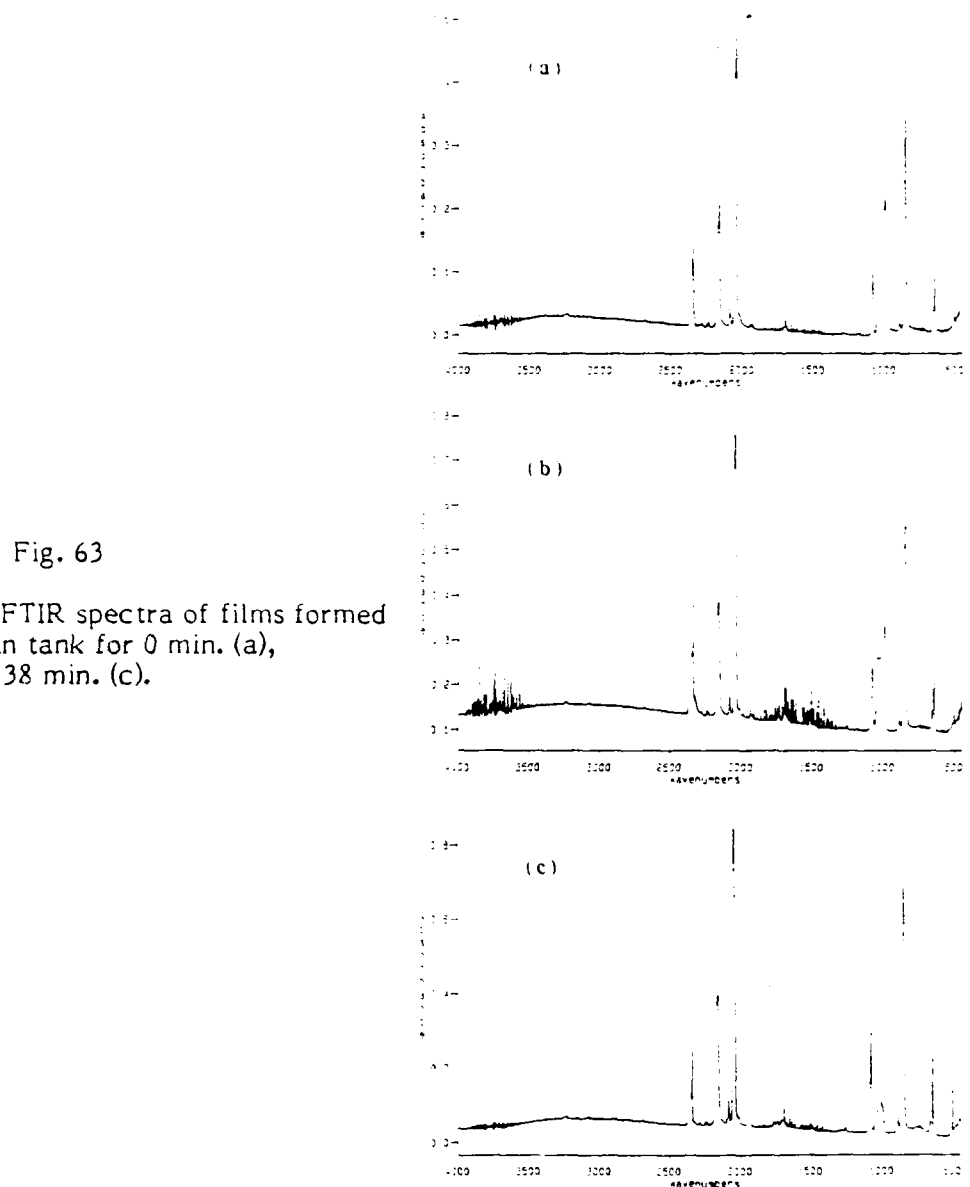


Fig. 63

Comparison of FTIR spectra of films formed with FN_3 held in tank for 0 min. (a), 23 min. (b) and 38 min. (c).

5.2 Moderation of Burn Velocity

As CO_2 and N_2F_2 were the only foreign species positively identified in the above studies, it was hypothesized that one of these two species, or perhaps both, were responsible for the variability in the burn velocity data. These two species are, thus, potentially effective moderators of the burn rate. Several experiments were performed to verify and quantify this hypothesis.

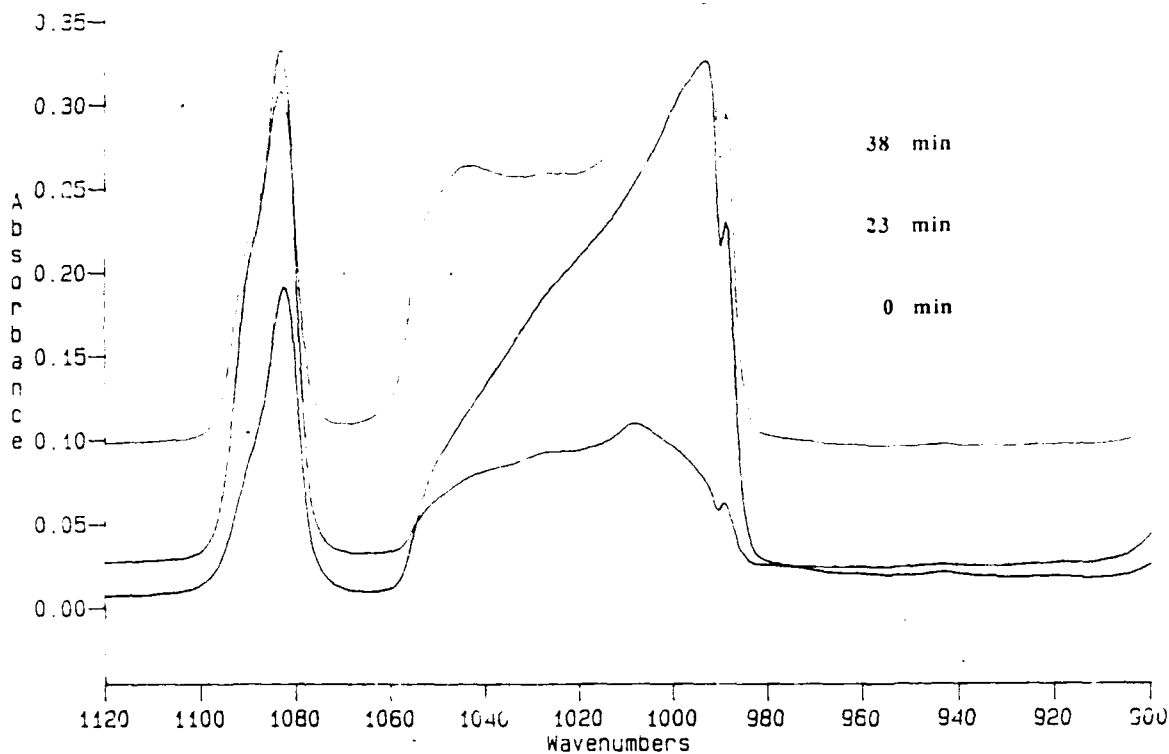


Fig. 64 Expansion of the 1000 cm^{-1} region of Fig. 63.

The effectiveness of carbon dioxide as a moderator was assessed by measuring the burn velocity of films which were intentionally doped with various amounts of CO_2 . In these experiments, the burn velocity was measured using the scattering probe apparatus (Fig. 27). The amount of CO_2 relative to FN_3 in each of the experiments was determined via FTIR of the gas phase mixture immediately prior to deposition onto the cryogenic substrate. For each sample, the CO_2 and FN_3 flows were admitted through needle valves, into a mixing manifold and, subsequently, into the holding tank. Each sample was freshly prepared immediately prior to film formation.

The delay time between irradiation of the film with the ignition pulse and arrival of the combustion front to the distant scattering probe beam is plotted against the percentage of CO_2 in the sample. The data are highly correlated and indicate that a 10% change in the level of CO_2 is required to change the delay by 1 μs . For this ignition-probe beam separation of this experiment, this corresponds to a 0.33 mm/ μs reduction in burn velocity for every 10% increase in CO_2 . Since such large amounts are required, CO_2 is not an overwhelming effective moderator.

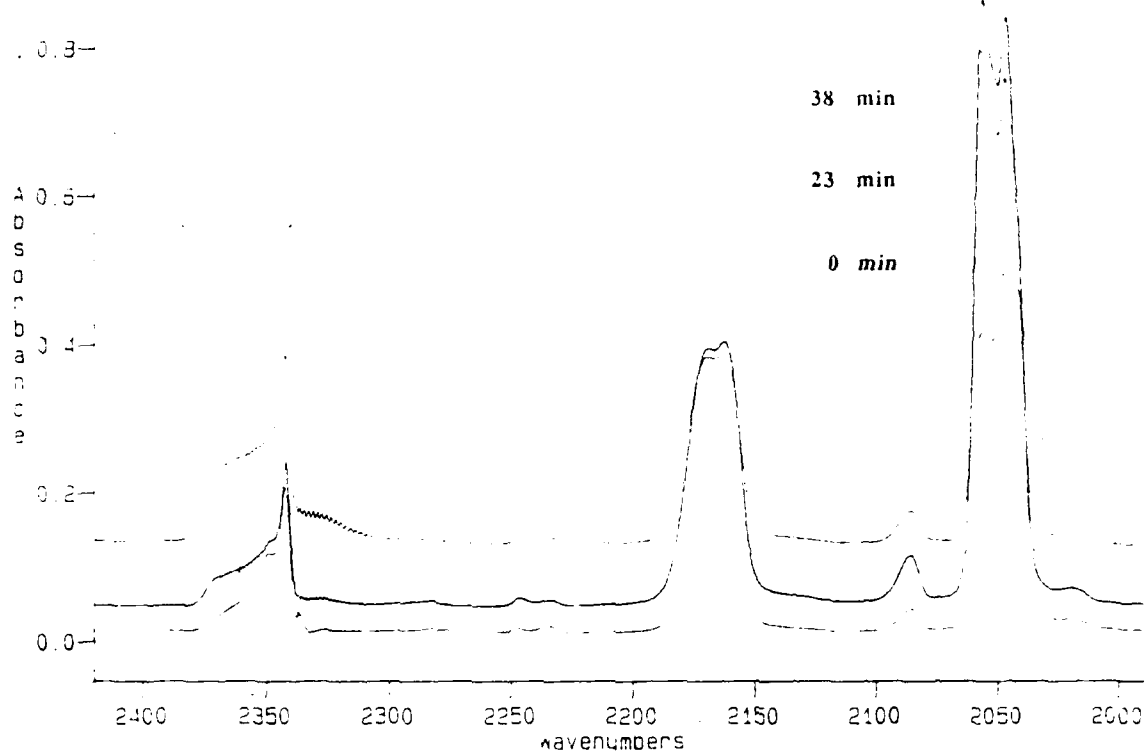


Fig. 65 Expansion of the 2200 cm^{-1} region of Fig. 63.

The rather ineffective performance of carbon dioxide may well be a function of how the molecule is incorporated into the film. To ideally moderate the burn velocity via incorporation of additives which, in the manner previously illustrated, moderate the combustion temperature, the additive should be uniformly distributed. That is, the presented model is most valid for two component amorphous films. The gas deposition rate and substrate temperature used in these experiments indicate that the films are not amorphous. Rather, it is suspected that the films are composed of islands of CO_2 and FN_3 . The FTIR diagnostic is quite insensitive to this molecular segregation. Thus, in these experiments, CO_2 may not be effectively coupled into the combustion environment. A moderating influence was, nevertheless, observed when CO_2 was incorporated into the films.

As mentioned earlier, the burn velocity was observed to vary with the time that the FN_3 sample was held in the holding tank (tank lifetime). Further, it was speculated that this effect may be due to an increase in the ratio of CO_2 to FN_3 that

was expected to result from the thermal decomposition of the FN₃. To verify this speculation, a series of experiments which were exactly analogous to the CO₂-doped film experiments were conducted. In these experiments, however, the spectroscopic and scattering probe delay time changes were measured as a function of tank lifetime, and impurities were not intentionally added to the FN₃ sample. The holding tank was operated at a somewhat higher temperature (9°C) than normal to facilitate these experiments.

The delay time (inversely proportional to burn velocity) is plotted as a function of FN₃ tank lifetime in Fig. 67. It is evident from this figure that the delay is highly sensitive to tank lifetime: A 1 μ s increase in delay requires an approximately 10 minute increase in the time of the FN₃ sample in the holding tank. Given the data of Fig. 66, if the effect observed in Fig. 67 is attributable to an increase in the relative amount of carbon dioxide in the tank, the rate of increase must be on the order of 1% CO₂/min. Examination of Fig. 68, which shows the percentage of CO₂ (relative to CO₂ + FN₃) in the samples used to form the studied films, illustrates that the observed increase in delay is not entirely attributable to an increase in the level of CO₂. Although the data are scattered, the best fit line indicates that a 1% change in CO₂ level occurs in approximately 60 minutes. If the final data point of Fig. 68 is omitted to get the most optimistic fit of the data, 10 minutes are required to obtain a 1% increase in CO₂. As this is an order of magnitude below that required to explain the observed burn velocity reduction, it is concluded that a species other than CO₂ is responsible.

FTIR spectroscopy was employed in an attempt to identify this burn moderating species. Figure 69 displays the difference spectrum obtained from IR spectra of the tank gases at holding tank times zero and thirty minutes. No IR absorptions were observed outside the range of the displayed spectrum. The two observed features are easily assignable as CO₂ and N₂F₂. Because the level of the weak 990 cm⁻¹ band of N₂F₂ is very sensitive to the factor chosen in the spectral subtraction routine, the concentration of this species as a function could not be reliably monitored. Nevertheless, because it is present, and no other species can be reasonably invoked to account for the observed moderation in burn velocity, it is speculatively concluded that N₂F₂ is the second species responsible for the moderation of the combustion of FN₃ films.

Fig. 66

Delay in arrival of combustion front to probe site plotted against percentage of CO_2 added to film.

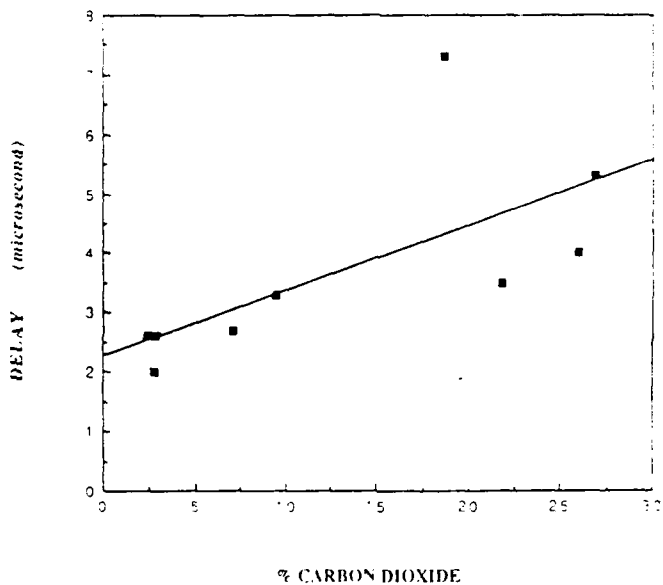
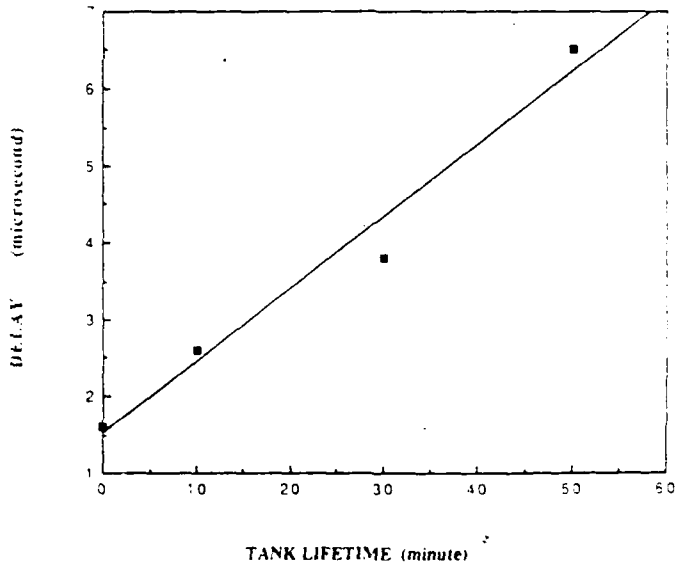


Fig. 67

Delay in arrival of combustion front to probe site plotted against time gases were held in 9°C holding tank.



Since only trace amount of the N_2F_2 species could be detected, it appears to be an exceedingly effective moderator. Thus, it must affect the combustive process in some way other than simply increasing the bulk heat capacity of the film. The N_2F_2 species may be more compatible within the FN_3 crystal lattice, hence, less likely to segregate. If, as illustrated in the following section, the combustion of condensed phase FN_3 involves 'aligned reagents', species which alter the crystal lattice may well be effective moderators.

Fig. 68

Percentage of CO_2 relative to $\text{CO}_2 + \text{FN}_3$ in 9°C holding tank plotted against holding time.

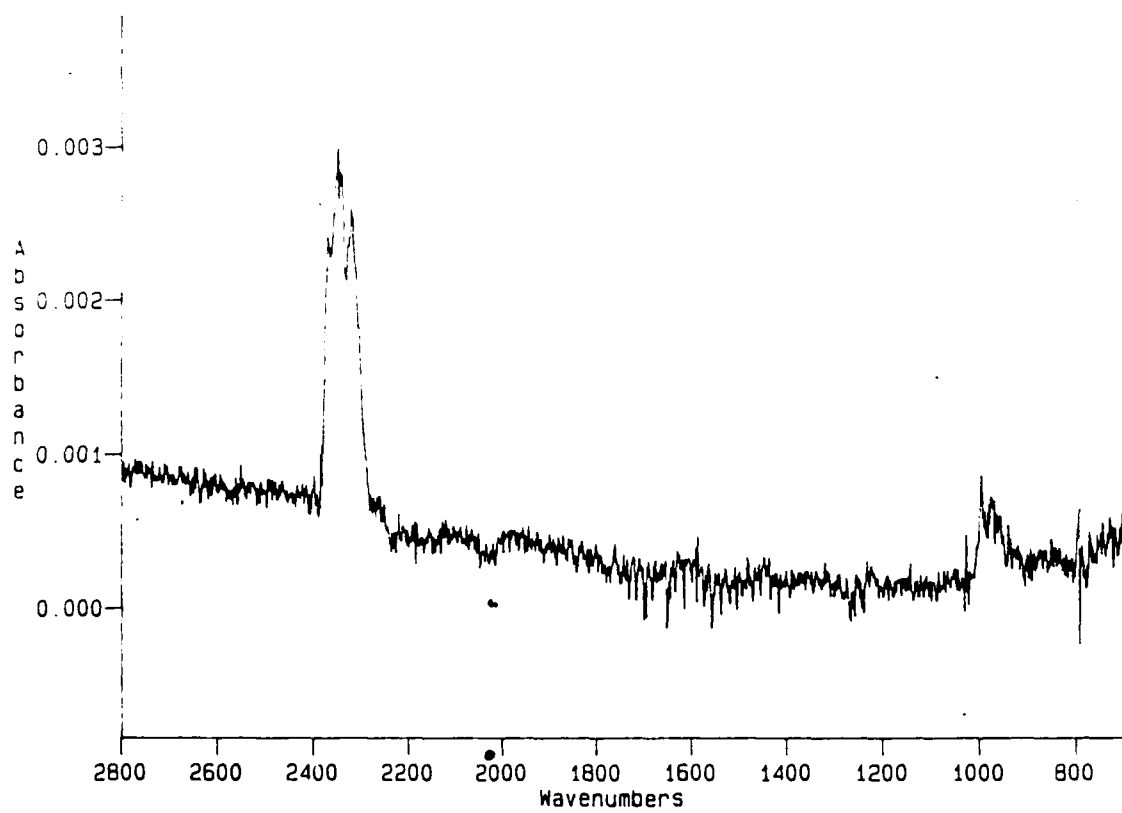
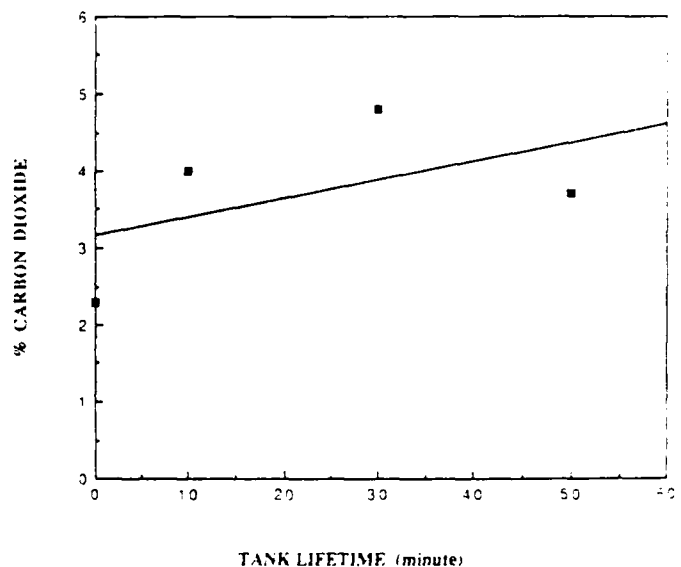
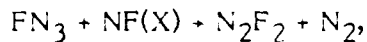


Fig. 69 Difference FTIR spectra taken from 9°C holding tank gases at 0 and 30 minutes.

5.3 Mechanism of Stability Enhancement

If, indeed, the N_2F_2 species is an exceedingly effective moderator at even very low concentration levels, the thermal FN_3 detonation mechanism needs to be modified. A variety of other, even more speculative reaction pathways involving NF fragments can be envisioned. One of the more enticing is somewhat analogous to reaction;



and involves aligned reagents. As illustrated in Fig. 70, Brener⁵ has calculated that the structure of condensed phase FN_3 is composed of regular "sheets" comprised of subunits that have two interlocking "L" shaped FN_3 molecules. As shown by the dotted lines in Fig. 70, in this geometry the NF segments of each azide molecule is aligned with that of a neighboring molecule in such a manner that solid state reactions can lead to the formation of both cis- and trans- N_2F_2 with very little structural rearrangement of the solid. Thus, low level impurities which form a solid solution with FN_3 , thereby disrupting the FN_3 crystal lattice, will prevent aligned reagent reactions and will thus inhibit decomposition.

Although the occurrence and relative importance of the above reaction is a matter to be investigated, formation of N_2F_2 is expected to be an important component of FN_3 chemistry. Indeed, N_2F_2 is known to be a product of FN_3 thermolysis.^{1,41} It is also an abundant by-product in NF matrix isolation experiments where deposition is from a rapidly heated flow of a fluorine azide- rare gas mixture.⁴² Besides its facile formation, this species is also important because a significant amount of the FN_3 combustion energy may be carried in its metastable states: Using spin selection rules, the N_2F_2 product of reaction 5 is predicted to be in a metastable triplet state, storing approximately 6 eV.⁴³ Consequently, facile formation (via aligned reagent reaction) and collisional relaxation of this species can easily support the development of a detonation wave in the FN_3 films. Again, additives which perturb the FN_3 lattice may inhibit the detonation process.

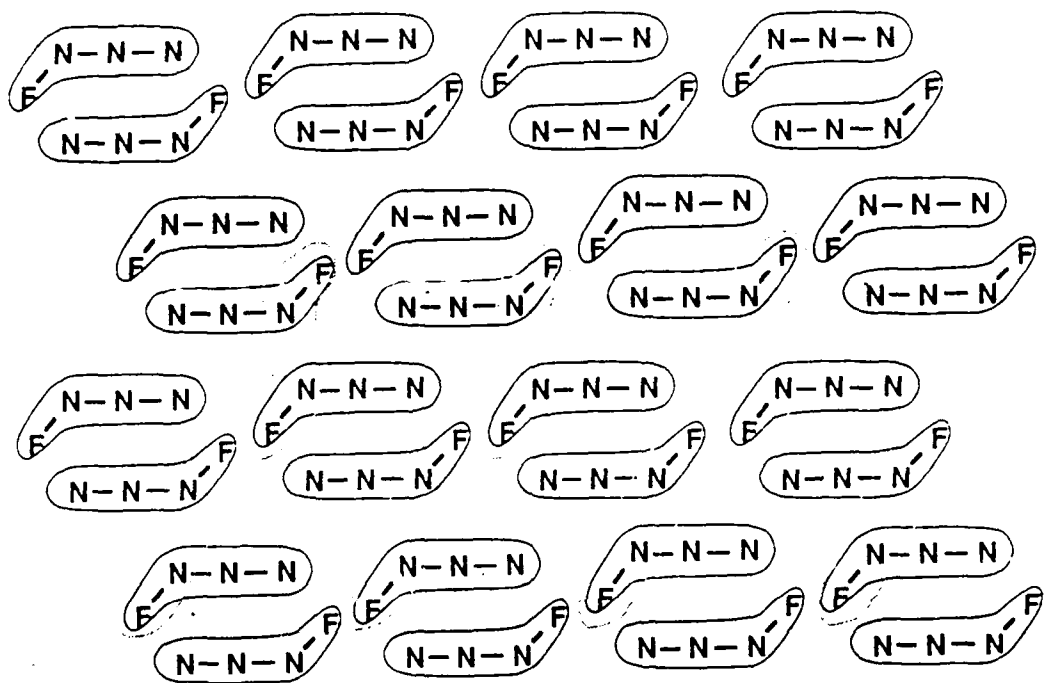


Fig. 70 Diagram of regular sheet structure of solid FN_3 calculated by Brener.

6.0 SUMMARY AND RECOMMENDATIONS

During the course of this research we have developed a state of the art fluorine azide production facility. This facility is capable of providing a relatively pure continuous flow of fluorine azide over an extended period. The 350 torr, 3 sccs flow of approximately 4% fluorine azide is stable for approximately five hours and can be produced on a daily basis. Also, an apparatus for the reproducible production and ignition of 10 μm thick cryogenic fluorine azide films has been developed.

To ultimately develop methods for burn rate moderation, or 'stabilization', the decomposition of this condensed phase material has been characterized using a variety of techniques. By emission spectroscopy, it was discovered that detectable concentrations of NF(a) and NF(b) were not present following ignition of FN_3 . If these species are produced in abundance, they are presumably readily quenched or reacted. Detection of $\text{CN}(\text{B}+\text{X})$, but no $\text{CN}(\text{A}+\text{X})$ emission implied that the B state was populated by energy transfer with some species containing at least 3.2 eV excess energy. Potential transfer partners include NF(a,b) in a state of high vibrational excitation and electronically excited metastable N_2F_2 .

Using a laser scattering probe, the velocity of the combustion front of the laser ignited material was found to be approximately 1 mm/ μs . The velocity of the plume gases was found to be comparable. Using a pulsed laser schlieren photography technique, the burn velocity was found to have the slightly larger value of 1.6 mm/ μs . The schlieren plume imaging experiments also indicated that the plume had a structure which was indicative of film decomposition via a detonation process. A single step detonation mechanism was proposed. In this scheme, the approximately 30 kcal/mol released via



is coupled into neighboring FN_3 molecules, causing these molecules to surmount the 14 kcal/mol decomposition barrier. On the basis of this model, it was concluded that the burn rate can be acceptably moderated by incorporating materials which increase the heat capacity of the azide films. Addition of CO_2 to the cryogenic films only moderately slowed the burn velocity. It was speculated that the relative ineffectiveness of CO_2 as a moderator was due to segregation of CO_2 into 'islands', as opposed to

formation of a true solid solution with the azide. (Note that the measured value of burn velocity is for microscopically thin films of the material. It is conceivable that decomposition of bulk quantities of the material may proceed through a different combustion mechanism, yielding a different value for the burn velocity.)

Conversely, N_2F_2 and N_2F_4 which are decomposition products of FN_3 were found to significantly slow the burn velocity of the fluorine azide films. The active species were present in such trace amounts that it was not detectable via FTIR. Use of mass spectroscopic analysis identified the species as the active moderator. As only trace amounts were effective, N_2F_2 and N_2F_4 are not likely to influence the burn rate by acting as heat sinks. It was postulated that these species form a solid solution with fluorine azide and act to disrupt the crystal lattice. Further, disruption of the regular alignment of the NF_3 lattice prohibits facile formation of reaction products, and subsequently slows the decomposition rate.

Methods which can potentially be employed to stabilize CBES materials, in general, and FN_3 , in particular, have been identified as a result of the described experiments. This is a significant result since fluorine azide has an I_{sp} of approximately 380 sec,⁴⁴ and is thus an attractive monopropellant. It is, therefore, recommended that the Air Force further pursue this area of research in greater detail. Specifically, experiments, such as analysis via mass filtering, which directly monitor the temporal profile of the nascent decomposition (detonation) products are suggested. This approach offers as the most cost effective method of elucidating the detonation mechanism and furthering developing CBES propellants.

7.0 REFERENCES

1. Haller, J.F., Ph.D. Dissertation, A Study of the Preparation, Structure, Properties, and Decomposition of Azine Fluoride and of Difluorodiazene, Cornell University (1942).
2. Patel, D., Pritt, A.T., and Benard, D.J., Photolysis of Fluorine Azide (FN_3) at 193 nm, *J. Phys. Chem.* 90, 1931 (1986).
3. Gholivand, K., Schatte, G. and Willner, H., Properties of Triazadienyl Fluoride FN_3 , *Inorg. Chem.* 26, 2137 (1987), and references therein.
4. Michels, H.H. and Montgomery, J.A., Theoretical Investigation of Energy Storage in Atomic and Molecular Systems, AFAL Report, Contract No. F04611-86-C-0071, Aug. (1988).
5. Brener, N., High Energy Density Materials Contractors Conference, New Orleans, March (1989).
6. Benard, D.J., Winker, B.K., Seder, T.A. and Cohn, R.H., Production of Nitrogen Monofluoride ($\text{a}^1\Delta$) by Dissociation of Fluorine Azide, *J. Phys. Chem.* 93, 4790 (1989).
7. Quinones, E., Habdas, J., and Setser, D.W., Gas-phase Chemistry of Fluoroimidogen ($\text{a}^1\Delta$): quenching rate constants, *J. Phys. Chem.* 91, 5155 (1987).
8. Herbelin, J.M., The Role of Electronic Spin in the Nitrogen Fluoride (NF) Kinetic System, *Chem. Phys. Lett.* 42, 367 (1976).
9. Krakow, B., Lord, R.C. and Neely, G.O., High Resolution Far Infrared Study of Rotation in Hydrazoic Acid, Isocyanic Acid, Isothiocyanic Acid, and their Deuterium Derivatives, *J. Mol Spect.* 27, 148 (1968).

10. Rosen, B., Spectroscopic Data Relative to Diatomic Molecules, Pergamon Press, New York (1970).
11. Dows, D.A. and Pimentel, G.C., Infrared Spectra of Gaseous and Solid Hydrazoic Acid and Deutero-hydrazoic Acid: The Thermo Dynamic Properties of HN_3 , J. Chem. Phys. 23, 1258 (1955).
12. McDonald, J.R., Rabalais, J.W. and McGlynn S.P., Electronic Spectra of the Azide Ion, Hydrazoic Acid, and Azido Molecules, J. Chem. Phys. 52, 13432 (1970).
13. King, S-T. and Overend, J., Infrared and Raman Spectra of Trans N_2F_2 , Spectrochim. Acta 22, 689 (1966).
14. King, S-T. and Overend, J., The Vibrational Spectrum of Cis N_2F_2 , Spectrochim. Acta 23A, 61 (1967).
15. Pace, E.L. and Pierce, L., Infrared and Raman Spectra of Nitrogen Trifluoride, J. Chem. Phys. 23, 1248 (1955).
16. Dows, D.A. and Pimentel, G.C., Infrared Spectra of Gaseous and Solid Hydrazoic Acid and Deutero-hydrazoic Acid: The Thermo Dynamic Properties of HN_3 , J. Chem. Phys. 23, 1258 (1955).
17. Brener, N., AFOSR Conference on Azide Chemistry, Denver (1989).
18. Childs, C.B., Low Pressure Mercury Arc Lamp for Ultraviolet Calibration, Appl. Optics 1, 711 (1962).
19. Lewis, R.W., Teets, R.E., Sell, J.A. and Seder, T.A., Temperature Measurements in a Laser-heated Gas by Quantitative Shadowgraphy, Appl. Optics 26, 3695 (1987).

20. Malins, R.J. and Setser, D.W., Rate Constants, Branching Ratios, and Energy Disposal for NF(b, a, X) and HF(v) Formation from the H + NF₂ Reaction, J. Phys. Chem. 85, 1342 (1981).
21. Coombe, R.D., Chemical Production of Excited NF, Final Report of AFWL Contract No. F29601-79-C-0016, September (1981).
22. Michels, H.H., personal communication (1988).
23. Tennyson, P.H., Fontijn, A. and Clyne, M.A.A., Radiative Lifetimes of Metastable States of Free Radicals. I. Nitrogen Fluoride (NF), Chem. Phys. 62, 171 (1981).
24. Mohamed, K.A., Khanna, B.N. and Lal, K.M., Frank-Condon Factors and R-centroids for the b¹ Σ^+ - X³ Σ^- Band System, Ind. J. Pure Appl. Phys. 25, 221 (1974).
25. Pritt, A.T. and Benard, D.J., Temperature Dependence of the Rate of the Electronic-to-electronic Energy Transfer from Fluoroimidogen (NF(b¹ $\Sigma^+})) to Iodine Fluoride (IF), J. Chem. Phys. 85, 7159 (1986).$
26. Walker, R.F. in Energetic Materials 2, Fair, H.D and Walker, R.F. (eds.), Plenum Press (1977).
27. Michels, H.H., United Technologies Research Center Report No. 77-05-236-8 (1977).
28. Rosenwaks, S., Beer-Sheva University, personal communication, (1989).
29. Benard, D.J. and Cohn, R.H., Quarterly Report No. 4, Model Studies of CBES Decomposition AFAL Contract No. FO4611-86-C-0072, December (1987).
30. Obase, H., Tsuji, M. and Mishimura, Y., First Observation of the c¹ π -b¹ Σ^+ Transition of the Fluoroimidogen Radical, Chem. Phys. Lett. 126, 134 (1986).

31. Young, R.A., Rocketdyne, personal communication (1988).
32. Arnold, J.S., Ogryzlo, E.A. and Witzke, H., Some New Emission Bands of Molecular Oxygen, *J. Chem. Phys.* 40, 1769 (1964).
33. Bader, L.W. and Ogryzlo, E.A., Reactions of $O_2(^1\Delta_g)$ and $O_2(^1\Sigma_g^+)$, *Disc. Faraday Soc.* 37, 46 (1964).
34. Thrush, B.A., The Detection of Free Radicals in the High Intensity Photolysis of Hydrogen Azide, *Proc. Roy. Soc.* 235, 143 (1956).
35. Alexander, M.H., AFOSR Conference on Azide Chemistry, Denver (1989).
36. Duff, R.E. and Houston, E., Measurement of the Chapman-Jouget Pressure and Reaction Zone Length in a Detonating High Explosive, *J. Chem. Phys.* 23, 1268 (1955).
37. Hershowitz, J., from Explosive Technology Short Course, Monterey, CA, administered by Computational Mechanics Associates, March (1989).
38. Chaudhri, M.M. and Field, J.J., in Energetic Materials 2, Fair, H. D and Walker, R. F. (eds.), Plenum Press (1977).
39. Greiner, N.R. and Blais, N., Free-expansion Experiments and Modeling in Detonation: Chemistry and Hydrodynamics on a Laboratory Scale (submitted paper #124) 9th Symposium(International) on Detonation (1989).
40. Alster, J., Downs, P.S., Gora, T., Iqbal, Z., Fox, P.G. and Mark, P., in Energetic Materials 2, Fair, H. D and Walker, R. F. (eds.), Plenum Press (1977).
41. Benard, D.J., Winker, B.K. and Seder, T.A., Model studies of CBES Decomposition Air Force Astronautics Laboratory Technical Report #8, July (1988).

SC 5467.FR

42. Wilner, H., University of Hanover, private communication (1988).
43. Brener, N., Louisiana State University, private communication (1988).
44. Thompson, S., AF Astronautic Laboratory, personal communication (1989).
45. Durig, J.R. and Clark, J.W., Raman Spectrum and Structure of N_2F_4 , J. Chem. Phys. 48, 3216 (1968).